Density and porosity of the upper lunar crust from combined analysis of gravity and topography data – Evaluation of the interior structure of impact basins

vorgelegt von
M.Sc. Daniel Wahl
ORCID: 0000-0003-4884-6630

von der Fakultät VI – Planen, Bauen, Umwelt
der Technischen Universität Berlin
zur Erlangung des akademischen Grades

Doktor der Ingenieurwissenschaften
- Dr.-Ing. -

genehmigte Dissertation

Promotionsausschuss:

Vorsitzender:	Prof. Dr. Frank Flechtner
Gutachter:	Prof. Dr. Jürgen Oberst
Gutachter:	Prof. Dr. Doris Breuer
Gutachter:	Prof. Dr. Ulrich Hansen

Tag der wissenschaftlichen Aussprache: 18. Dezember 2020

Berlin 2021

Technische Universität Berlin

PhD Thesis

Density and porosity of the upper lunar crust from combined analysis of gravity and topography data – Evaluation of the interior structure of impact basins

Supervised by
Prof. Dr. phil. nat. Jürgen Oberst

Released by
M.Sc. Daniel Wahl

Berlin 2021

Density and porosity of the upper lunar crust from combined analysis of gravity and topography data –
Evaluation of the interior structure of impact basins

Daniel Wahl

This research was funded by the Deutsche Forschungsgemeinschaft (DFG),
grant SFB TRR-170-1 TP A4 – Late Accretion onto Terrestrial Planets.
The project was realized at the Chair of Planetary Geodesy, Institute of Geodesy and Geoinformation Science,
Technische Universität Berlin, Germany.

Acknowledgement

First, I would like to express my gratitude to Jürgen Oberst, who offered me the great opportunity to do my PhD in the most exciting field of lunar research at his department of Planetary Geodesy at Technische Universität Berlin. Thank you for providing excellent support throughout the entire doctorate and spending so much time discussing my work. Thank you for sending me around the world to inspiring conferences and workshops, where I had the chance to present and discuss my findings with experts from different scientific fields. I have taken part in exciting excursions, where I discovered volcanoes and impact craters, hold meteorites of several kilograms in my hands, and browse through one of the last original copies of the book *Sidereus Nuncius* where Galileo Galilei published his famous drawings of the Moon and Jupiter's satellites.

I want to thank Mark Wieczorek who hosted me at the Observatoire de la Côte d'Azur. Even if my stay was short, the time spending with you was very inspiring and helpful to me. I have learned a lot from our discussions, and I will never forget the familiar atmosphere during lunch in the small restaurant in the center of the historical observatory, with the most wonderful view over Nice.

I gratefully acknowledge Frank Flechtner for being the head of the committee as well as my reviewers Doris Breuer and Ulrich Hansen for evaluating this dissertation.

I want to thank the entire team of planetary geodesists at the Institute of Geodesy and Geoinformation Science. I enjoy every minute with my most favorite colleagues. How lucky I am to have met all of you! I also want to express my gratefully thanks to Kai Wünnemann and Frank Sohl for their constructive and friendly advice as well as Sven Weißbrich, who always supports me in any matter of adjustment calculation tasks.

Finally, I would like to thank my family for giving me so much. My mother Annette Wahl, who always believes more in my skills than I do. Thank you for your unrestricted love and support. My partner in life Nina Fisseler, for withstanding all my tense and stress throughout the preparation of this thesis (and beyond). And my son Justus, who is giving me so much, spending the first years of his life together with him. I am sure you will find your way to explore your most favorite planet, Neptune.

Abstract

The upper crust of the Moon exhibits large variations in bulk density and porosity owing to the formation sequence and spatial distribution of large impact basins. The focus of this work is on the detailed characterization of the porosity structure of lunar basins using the most recent data from lunar missions.

Specifically, lateral variations in bulk density are calculated using a high-resolution Gravity Recovery and Interior Laboratory (GRAIL) gravity model, developed to spherical harmonic degree and order 1500, in combination with topography, derived from the Lunar Orbiter Laser Altimeter (LOLA). Two different methods for estimating the bulk density are compared: The first approach focuses on minimizing the correlation between Bouguer gravity and the topography. Bulk density maps are derived for grid points of a global raster with a spacing of 0.75° within circular analysis regions of 3° radius. Thus, the spatial resolution is improved by a factor of two compared to maps presented previously (Wieczorek et al., 2013).

The first method is tested against a modified approach, where we search for the density which minimizes the short-scale roughness of the derived Bouguer anomaly. While both approaches show similar results in almost all the lunar highlands, significant discrepancies of up to 700 kg m^{-3} are found in regions, where the terrain is flat and prominent topographic features are lacking.

Global porosity of the upper crust is calculated using bulk densities in combination with independently obtained grain densities, estimated from remotely obtained composition of surface materials.

Detailed porosity maps as well as azimuthally averaged porosity profiles of 40 impact basins ($D > 200$ km) located in the lunar highlands are derived. The basins typically show similar porosity signatures, characterized by high crustal porosities near the basin rims as opposed to low porosities in their centers within the peak ring. We find that larger basins possess a more pronounced porosity signature than smaller basins. Furthermore, we find that younger basins show a more pronounced porosity contrast, while for older basins the porosity signatures tend to vanish within the global background, presumably due to their longer exposure and modification through subsequent impacts.

The new data on the interior structure of impact basins elaborated in this work complement our knowledge about the characteristics of lunar craters. The gained results help to improve our understanding of the formation process of the lunar impact basins and give us new insights in the modification of the upper crust of the Moon during the late accretion of terrestrial planets.

Zusammenfassung

Der obere Teil der Mondkruste weist große Variationen in seiner Schüttdichte und Porosität auf, was auf die sequenzielle Bildung und die räumliche Verteilung großer Einschlagbecken zurückzuführen ist. Der Schwerpunkt dieser Arbeit liegt auf der detaillierten Beschreibung der Krustenporosität dieser Einschlagbecken unter Verwendung aktueller Daten unterschiedlicher Missionen.

Durch die kombinierte Auswertung eines hochauflösenden Schwerefeldmodells der Gravity Recovery and Interior Laboratory (GRAIL) Mission, entwickelt bis zur Kugelflächenfunktion von Grad und Ordnung 1500, und der Topographie, hergeleitet aus Messdaten des Lunar Orbiter Laser Altimeters (LOLA), werden zunächst laterale Variationen der Schüttdichte bestimmt. Zwei unterschiedliche Methoden zur Berechnung werden miteinander verglichen: Bei dem ersten Ansatz wird die Schüttdichte durch das Minimieren der Korrelation zwischen der Bouguer Schwere und der Topographie bestimmt. Durch die Berechnung einzelner Rasterpunkte (Abstand von 0.75°) innerhalb 3° großer Analyseregionen, konnte die räumliche Auflösung im Vergleich zu früheren Karten (Wieczorek et al., 2013) um einen Faktor von zwei verbessert werden.

Die erste Methode wird mit einem weiterentwickelten Ansatz verglichen, bei dem die gesuchte Schüttdichte durch das Minimieren der Oberflächenrauigkeit der Bouguer Schwere bestimmt wird. Während beide Ansätze für das Mondhochland nahezu identische Ergebnisse liefern, gibt es kleine Regionen, in denen große Abweichungen von bis zu 700 kg m^{-3} auftreten. Die Ursache für die Differenzen liegt in der Beschaffenheit des Geländes, welches in den problematischen Bereichen sehr flach ist und keine markanten topographischen Punkte aufweist.

Die Porosität des oberen Krustengesteins lässt sich bestimmen, indem man die ermittelte Schüttdichte in Relation zur Korndichte setzt. Die Korndichte ergibt sich aus der Zusammensetzung des Oberflächenmaterials und stellt somit einen von der Schüttdichte unabhängigen Datensatz dar.

Detaillierte Karten der Porosität, sowie azimutal gemittelte Profile von insgesamt 40 Einschlagbecken (D > 200 km) in den Hochländern zeigen, dass die meisten Becken ähnliche Signaturen aufweisen. Im Zentrum, innerhalb des Peak-Rings, weist das Krustenmaterial eine sehr geringe Porosität auf, während weiter außen, in der Nähe des Beckenrandes, eine sehr hohe Porosität beobachtet werden kann. Die Intensität dieser Signatur wird durch die Größe des Beckens bestimmt, wobei größere Krater einen markanteren Ausdruck in ihrer Porositätsstruktur aufweisen als kleinere. Auch das Alter der Becken hat einen Einfluss auf die vorzufindende Porosität: Jüngere Becken zeigen einen ausgeprägten Kontrast in ihrer Porosität

als ältere Becken. Der Grund ist vermutlich, dass ältere Becken den Einschlägen von Meteoriten länger ausgesetzt waren. Ihre ursprüngliche Porositätsstruktur wurde stärker verändert, so dass ihre Signatur im globalen Hintergrund teilweise nur noch schwer zu erkennen ist.

Die in dieser Arbeit neu gewonnenen Erkenntnisse über die innere Struktur von Einschlagbecken vervollständigen unser Wissen über die Eigenschaften von Mondkratern. Sie verbessern unser Verständnis über die Entstehungsprozesse von Einschlagbecken und die Modifikation der oberen Mondkruste in der späten Akkretionsphase der terrestrischen Planeten.

Content

List of Figures

List of Figures (continued)

List of Tables

Structure of the dissertation

The first chapter describes the *motivation* that leads to this work and its relevance in an overall scientific context.

The *introduction* presents findings in the fields of geology and geochemistry and focuses on the current state of geodetic and geophysical knowledge. Models of the gravitational field and the topography of the Moon are of essential significance, providing important details about its inner structure. Since the lunar crust was strongly affected by a massive bombardment in the early history, the introduction especially covers the properties of craters and basins, that have been formed by this bombardment.

The main part of this cumulative thesis consists of two peer-reviewed and published scientific papers:

Research paper I

Lateral variations in bulk density and porosity of the upper lunar crust from high-resolution gravity and topography data: comparison of different analysis techniques.
Authors: Daniel Wahl and Jürgen Oberst
Accepted manuscript, Open Access publication, Creative Common Attribution 4.0, published in ISPRS Annals of Photogrammetry, Remote Sensing and Spatial Information Science, IV-2/W5, 527-532, May 2019, doi: 10.5194/isprs-annals-IV-2-W5-527-2019

Research paper II

Crustal porosity of lunar impact basins
Authors: Daniel Wahl, Mark Wieczorek, Kai Wünnemann and Jürgen Oberst
Accepted manuscript, Open Access publication, Creative Common Attribution 4.0 published in Journal of Geophysical Research: Planets, 125(4), 1-14, April 2020, doi: 10.1029/2019JE006335

The *discussion* section covers the results of the two publications and emphasizes their contextual link. The obvious dependencies between estimated bulk densities and porosities of the upper crust are discussed as well as possible structural properties of mare basaltic regions, which were omitted from the main data analysis of this work. The chapter closes with an outlook and objectives for future investigations.

The thesis includes an *appendix*, summarizing mathematical background for working with spherical harmonic functions, a flowchart and description of the software that was developed for this work, and a critical discussion on the "effective resolution" of the bulk density and porosity maps prepared in this work.

1. Motivation

Impact craters are the most prominent landforms on the Moon. The old and large impact basins are witnesses of the Late Heavy Bombardment (LHB), which occurred in the early history of the inner Solar System. Their total number, size distribution, and formation time may constrain the mass flux and timing of this *Late Accretion*. While the existence of the Late Heavy Bombardment is undisputed (Morbidelli et al., 2018), the presence of a spike in the impactor flux ~3.9 Ga years ago (lunar cataclysm) or a steady decline (accretion tail) are currently being discussed (e.g., Bottke and Norman, 2017; Hartmann, 2019).

Also, fundamental aspects of the processes and products of basin formation remain not fully understood. Analyzing the morphological and geophysical characteristics of impact basins might help to understand the formation process of basins and their alteration with time. In order to draw conclusions about the characteristics of the impactors which created the basins during the LHB, numerical models are used for simulating impact cratering (e.g., Freed et al., 2014; Zhu et al., 2015; Miljković et al., 2016). Those numerical models need to be constraint by geophysical parameters, such as the density and the temperature of the target material. Analyzing the outcome based on observational data, the effect of individual parameters on the basin forming process can be quantified and adjusted for the next iteration (e.g., Pierazzo and Collins, 2004; Ivanov, 2005).

Impact craters of different sizes possess distinct surface morphologies and geophysical properties. Observations of the gravity field of impact craters and basins hint at complicated interior structures and mass distributions. Simple and complex craters ($D < 200$ km) possess a gravity low in their centers, probably caused by the excavation of crustal material during crater formation and fracture of the underlying rock (Pilkington and Grieve, 1992). However, lunar impact basins ($D > 200$ km) exhibit high mass concentrations, as revealed by early tracking data of the Lunar Orbiter (Muller and Sjogren, 1968). These mass concentrations could be studied in unprecedented detail with the high-resolution gravity data from the GRAIL mission (Zuber et al., 2013b). Neumann et al. (2015) showed that positive gravity anomalies are found in the center of lunar basins. The peak ring is surrounded by a negative anomaly, extending to the outer topographic rim, where the gravity field returns to normal. The mass concentration within the basin is caused by an uplift of dense mantle material, a consequence of crater excavation in a target of high temperatures, followed by an isostatic adjustment due to cooling and contraction of a melt pool in the basin center (Melosh et al., 2013). With this knowledge, new basins could be discovered even below a highly degraded surface relief utilizing GRAIL gravity data. With the

provided impact basin catalog by Neumann et al. (2015), listing morphological characteristics as well as properties of their gravity signal, a major step to a complete inventory of lunar impact basins has been taken.

Introducing GRAIL extended mission data as well as applying new processing strategies (e.g., Goossens et al., 2020), the resolution and accuracy of the gravity field models have improved over the last years. Using the most recent model at the time of preparing this work, bulk density and porosity of the upper crust were determined in higher resolution than before. This allows us not only to revise the properties of the crust in a global context. The high resolution enables a detailed investigation of the crustal porosity of individual impact basins.

Previous studies on crustal porosity associated with impact craters are either based on numerical models or depend on the interpretation of Bouguer gravity, serving as an indicator for variations in porosity (e.g., Milbury et al., 2015; Soderblom et al., 2015). Here, the main idea is that craters with reduced Bouguer anomalies in relation to their surroundings, exhibit higher crustal porosities than the neighboring crust. Since the analysis would be biased by the mass concentration caused by the mantle uplift, these studies are restricted to simple and complex craters with diameters smaller than 200 km. However, the presented results in this thesis are independent from the bending of the crust-mantle interface. We are therefore able to follow up on earlier work and investigate, for the first time, impact structures with diameters larger than 200 km. Another advantage is that we use observational data to derive absolute values, allowing a direct consideration of the bulk density of the upper crust and the porosity structure of lunar impact basins.

The following questions are of paramount interest for the present research: How do meteorite impacts modify the bulk density and porosity structure of the lunar crust? Do large impact basins possess the same porosity signature as smaller basins? Does the age of a basin have an influence on the characteristics of its crustal porosity? This work is motivated by the need to provide a complete inventory of lunar impact basins, in particular to study their interior mass distribution and crustal porosity structure. Moreover, the findings about the porosity of lunar impact basins provide details about their formation and may be used to constraint simulations of impact cratering using numerical models.

2. Introduction

Besides the Earth, our Moon is the best explored planetary body in our Solar System. Apparently, the reason for this is the small distance to the Moon compared to other celestial bodies. Apart from observations made from Earth, missions to the Moon help to better understand its present-day appearance and to learn more about its geological history. These missions range from orbiting spacecraft, observing the Moon with various instruments, to static landers or roving vehicles, performing in-situ experiments on ground, and to six manned missions, where astronauts carried out detailed surveys on the Moon and brought several kilograms of rock samples to Earth. Thanks to past, current, and future missions, we learn more about the Moon's interior. The uppermost layer of the differentiated Moon, the crust, is of particular interest. For gaining insights on the crust, Moon's geochemical characteristics are just as important as its geophysical constraints. Therefore, we will at first have a look at the Moon's mineralogy, and how the crust formed. Afterwards, findings from seismic data are presented, before we will consider the morphology of the surface, the gravitational field of the Moon, and how those fundamental geodetic observables are obtained. In the following section, different types of lunar impact structures are presented as well as their formation process. Determining the formation sequence as well as absolute ages of individual impact events help to constrain the impactor flux in the early Solar System.

2.1 Special object Moon

With a radius of 1737 km (about a quarter of Earth) and a total mass of approx. 73.46×10^{21} kg (about 1% of Earth; Michael and Blackshear, 1972) the Moon's global mean density amounts to 3340 kg m^{-3} (Solomon, 1974), which is about the same density as Earth's upper mantle (Birch, 1964) and which may also be an evidence of its genesis. Compared to other moons in our Solar System, the size ratio between the Moon and Earth is remarkable, with the Moon being comparably large. In contrast, the moons Phobos and Deimos e.g., possess a mass of only about 10^{-8} of their parent planet Mars (Christensen et al., 1977; Hildebrand et al., 1979).

Due to the rapid cooling after its formation (Wood, 1972), the lack of plate tectonics, as known from Earth, and the absence of atmospheric erosion, the Moon preserves remnants of its formation and evolution until today. While on the Earth only few highly degraded impact craters are known, the Moon is covered by vast numbers of comparably crisp impact craters of different sizes and ages. With a diameter of about 2400 km (Neumann et al., 2015), the largest impact

basin on the Moon (and at the same time the largest crater known in our Solar System) is South Pole-Aitken basin (Spudis et al., 1994). Impact melt, found in the vicinity of prominent impact basins, was dated to an age of about 3.9 - 4.5 Ga (e.g., Papanastassiou and Wasserburg, 1971; Tera et al., 1974; Stöffler and Ryder, 2001; Hartmann, 2019), which indicates that the largest basins on the Moon originate from the time, when the Moon just had formed.

2.2 The lunar crust

2.2.1 Composition of the lunar crust

Important knowledge on the Moon's inner structure is derived from the mineralogical and chemical composition of returned samples from the Apollo and the Luna program as well as from lunar meteorites collected on Earth. An important finding is the diversity and the identification of compositional types of lunar rocks (Heiken et al., 1991). The dark and smooth mare regions consist of basalts, derived from an ultramafic pyroxene and olivine source (Warren, 1985). Chemically, most mare basalts are enriched in TiO_2 and FeO (Taylor et al., 1991), why they possess much higher bulk densities (between 3010 and 3270 kg m^{-3}) compared to terrestrial basalts (Kiefer et al., 2012). Conversely, the bright and heavily cratered highland crust is composed of the mineral plagioclase, which has a low density. Most samples are enriched in Ca and Al, but poor in Fe, Mg, and Ti (Lucey et al., 2006). Besides those *Ferroan anorthosites* further types of highland rocks were identified, e.g., Mg rich feldspar, containing also grains of olivine and pyroxene (Heiken et al., 1991).

The different compositional rock types suggest that a segregation process must have occurred while the Moon has formed. A widely accepted hypothesis is the existence of an ancient global lunar magma ocean (e.g., Warren, 1985), which postulates that the Moon, at the time of its formation, was molten and exhibited material of low viscosity (Wood et al., 1970). When the lunar magma ocean began to crystalize, minerals of low density, like plagioclase, rose and formed the anorthositic crust (Warren and Wasson, 1977; Wood et al., 1970). Dense minerals like olivine and pyroxene sank down and created the mafic mantle. Numerical models indicate that the crystallization process of the lunar magma ocean took almost 200 Ma (Maurice et al., 2020), much longer than previously thought. While the uppermost layer solidified fast, forming an insulating layer on top of the magma ocean, the cooling process of the inner part was significantly slowed down. But many details of the crystallization process remain unknown and different models exist, how the magma ocean developed. One key question is the effect of dense ilmenite-bearing cumulates, which crystalized at the late stage of the solidification process of the

magma ocean (Snyder et al., 1992). Those cumulates formed near the base of the crust at a depth of around 100 km (van Orman and Grove, 2000). With a density of more than 3700 kg m^{-3} (Elkins-Tanton et al., 2002) they are denser compared to the underlying mantle. Several models suggest that the ilmenite-rich cumulates sunk through the mafic mantle down to the bottom of the magma ocean (Hess and Parmentier, 1995). Other studies propose that the structure became gravitationally unstable, leading to an overturn (Ringwood and Kesson, 1976). This would explain why Ti-rich mare basalts and minerals like olivine and pyroxene have been transported up to the lunar surface. Although not all particulars are answered, the idea of an ancient magma ocean provides not only an explanation for the segregation of the minerals, it is also consistent with the formation theory of the Moon through a giant impact (Hartmann and Davis, 1975), where the Moon was formed from very hot material. From all those different observations and reasonable assumptions, we think that the Moon is a differentiated body, composed of an inner core, a surrounding mantle, and an outer crust (Heiken et al., 1991; Wieczorek et al., 2006).

Besides anorthositic rocks, forming the lunar highlands, another main component of material found on the lunar surface are basalts. Mare basalts were most likely transported from deeper regions to the surface, as result of partial melting (Taylor, 1989). While the majority of a lunar magma ocean is assumed to have crystalized right at the beginning of the lunar evolution history, the age determination of some basaltic surfaces indicates that they were formed only 1 to 2 billion years ago (Hiesinger et al., 2000).

Our knowledge of the mineralogical and chemical composition of the lunar crust from analyzing rock samples is complemented by remote sensing data, which provide global context information on surface composition. Prominent examples of lunar missions are the Clementine mission (Nozette et al., 1994), where the surface was observed with different optical sensors, covering wide spectral ranges, revealing details about the global distribution and concentration of different minerals in the lunar soil. The Lunar Prospector mission (Binder, 1998) carried the Gamma Ray Spectrometer (Lawrence et al., 1998) from which first global counting rate maps of thorium, potassium, and iron were derived. Finally, the Moon Mineralogy Mapper instrument (Pieters et al., 2009) onboard the Chandrayaan-1 orbiter, provided a detailed assessment of abundances of minerals in the different lunar terrains.

Huang and Wieczorek (2012) and Kiefer et al. (2012) studied lunar rock samples and found a clear correlation of grain density and porosity on composition, in particular for iron and titanium abundances. Benefitting from these findings, global maps of Fe and TiO_2, from Lunar Prospector can be used to obtain information about the grain densities of the upper crust (Huang and Wieczorek, 2012).

2.2.2 Evidence from seismic data

One of the most instructive sources for details about the lunar interior are observations of seismic waves. Analyzing the attenuation, runtime, refraction, and reflection of seismic waves, insights on the interior of the planetary bodies can be gained (Aki and Richards, 2002). Active and passive seismic experiments had been carried out on the Moon. Since the seismic recordings represent the only in situ observations on the lunar interior, they are still of interest and have been analyzed with ever improving methods up to the present day.

The network of the Apollo Passive Seismic Experiment, including four stations spanning a near-equilateral triangle with a side of length of about 1100 km, operated between 1969 and 1977 (Latham et al., 1972; Nakamura et al., 1976). From early analysis of the data, the lunar crust-mantle boundary was estimated to have a depth of about 60 km (Toksöz et al., 1972; Nakamura et al., 1982). Using advanced data processing strategies, a crustal thickness of only 45 km including a discontinuity at a depth of about 20 km were found (Khan et al., 2000), dividing the lunar crust in an upper and a lower part. However, no seismic data on crustal thickness are available on the lunar farside. The discontinuity may indicate a change in composition or porosity (Wieczorek et al., 2006), as is supported by geochemical evidences and numerical modelling. The lower part of the crust is thought to be noritic (Ryder and Wood, 1965; Pieters et al., 2001), as is indicated by the mafic composition of impact melt rocks and central peaks of complex craters (both originating from deeper crustal regions) (Tompkins and Pieters, 1999). A change in porosity is just as likely. Numerical models show that the shockwaves from large impacts may fracture the target rock down to at least several kilometers (Collins, 2014), perhaps even down to the upper mantle (Wieczorek et al., 2013), matching the seismic discontinuity at 20 km depth.

A successful active seismic experiment was executed by the Lunar Seismic Profiling Experiment (Kovach et al., 1973), deployed by US astronauts of Apollo 17, providing details about the density structure of the near surface crust (~1 km depth). The experiment consisted of four identical geophones, set up in a Y-shaped array (Vostreys, 1980). Using eight explosive packages as well as the thrust of the Lunar Module's ascent stage during launch, and its later impact on the lunar surface, seismic waves could be recorded and analyzed (Cooper et al., 1974; Heffels et al., 2017). Cooper et al. (1974) presented a 4-layer model for the uppermost crust, showing a drastic increase of seismic velocity with depth (Figure 1). Using laboratory measurements of com-pressibility and elastic wave propagation within lunar basalts, the seismic velocity models may be interpreted in terms of density profiles. For example, for a P-wave velocity of 960 m/s a density of 3200 kg m^{-3} was derived (Cooper et al., 1974).

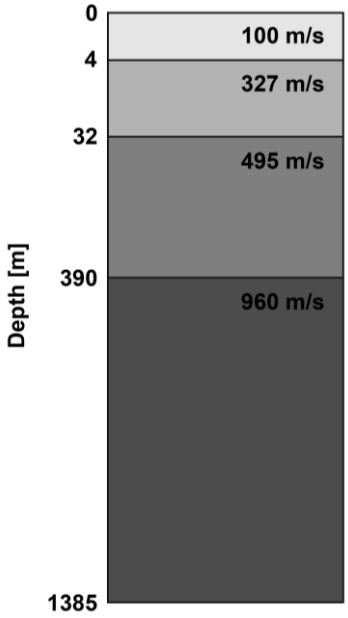

Figure 1: Modified figure of the velocity-depth profile from Cooper et al. (1974), indicating an increasing bulk density with depth at the Apollo 17 landing site in the Taurus-Littrow valley.

2.2.3 Surface morphology

The morphology of the lunar surface is characterized by two major units, the elevated (bright and heavily cratered) highlands, and the large (comparably young) mare depressions. While the lowest topographic depressions (about 8 km below the mean lunar sphere of 1737.151 km radius) are found inside the South Pole-Aitken (SPA) basin, the highest elevations (about 10 km) are found on the farside of the Moon, associated with the rims of the Korolev and Hertzsprung basins (Figure 2). Impact craters are by far the most prominent landforms, whereas rills, pits, domes, wrinkle ridges, and lobate scarps testify to the Moon's volcanic and tectonic history.

The topography also reveals insights in the internal structure, and the geological and thermal evolution of a planetary body (Zuber et al., 2012). Two independent remote sensing techniques are typically used for topographic mapping. Digital Terrain Models (DTMs) may be derived through photogrammetric analysis of stereo image data. The camera system aboard of the currently operating Lunar Reconnaissance Orbiter (LRO; Chin et al., 2007) mission consists of two identical panchromatic Narrow Angle Cameras (NACs), and a Wide Angle Camera (WAC), providing multispectral data in seven color bands. LROC (LRO Cameras) acquires global data with a resolution of 75 m/pixel (WAC), and high-resolution close-ups of 0.25 - 0.5 m/pixel (NAC) (Robinson et al., 2010). From the image data, global and local topographic data products have been derived, such as the Global Lunar DTM 100 m (GLD100; Scholten et al., 2012), or high-resolution (1 m) DTMs of the Apollo 17 landing site (Haase et al., 2019).

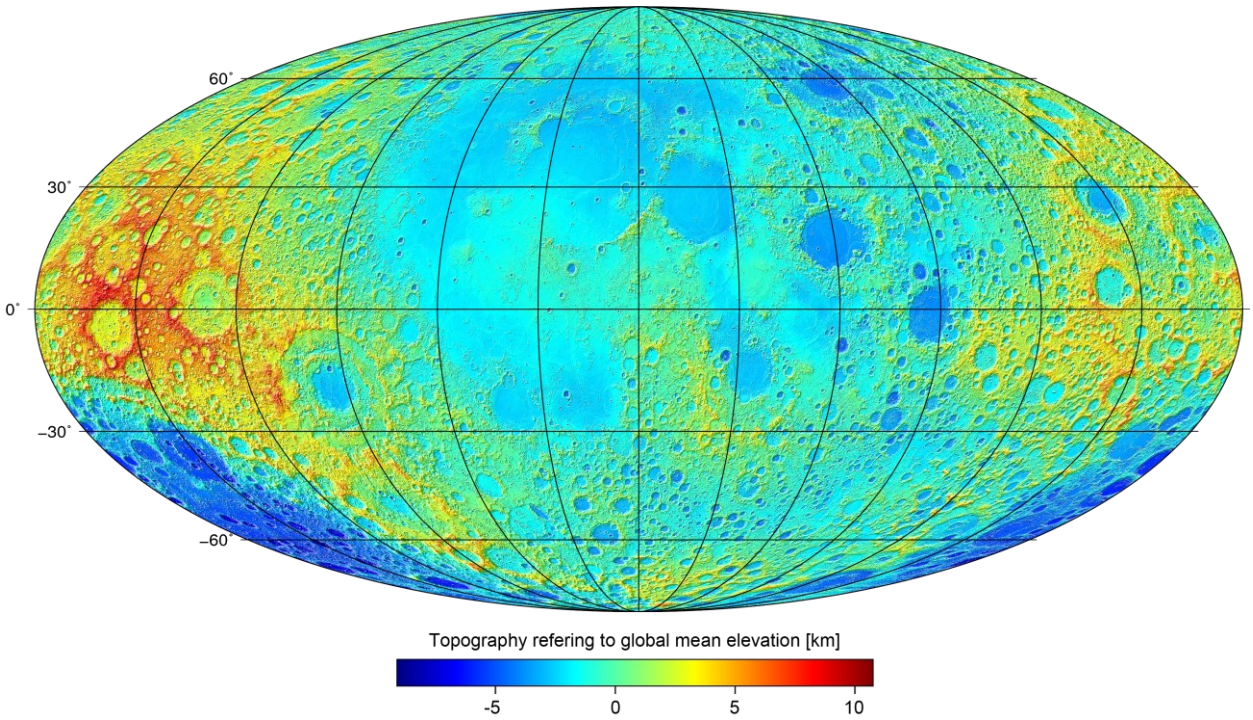

Figure 2: Global lunar topography derived from LOLA data. The heights refer to a global mean elevation of 1737.151 km. The map is given in Mollweide projection, centered at the lunar nearside at 0° East, 0° North.

Alternatively, precise topographic models may be obtained by Light Detection and Ranging (LiDAR) experiments, i.e., laser altimetry. Here, a laser emits short pulses from a spacecraft down to the planetary surface. The light is reflected, and a fraction of the backscattered radiation is detected by the instrument's receiver unit. By measuring the travel time of the laser pulse, the distance between the surface point and the instrument can be derived. In combination with the exact orbit of the spacecraft, the topography is determined, referencing surface ranges to the body's center of mass (Smith, et al., 2010). The vertical resolution is dependent on the laser pulse width and the timing precision of the altimeter electronics, while the horizontal resolution depends on the laser beam footprint size on ground, and the frequency of measurements along track (Bufton, 1989).

The first laser altimeter in space was the LiDAR instrument on the Apollo 15 mission, which used ruby flashlamp lasers, generating a few pulses per minute (in average 3.75 pulses per minute) (Kaula et al., 1973). An advanced LiDAR experiment on the polar-orbiting Clementine spacecraft (Nozette et al., 1994; Smith et al., 1997) successfully mapped the near-global lunar topography at a high vertical accuracy of a few hundred meters (Smith et al., 1997). After Clementine, several LiDAR systems were sent into lunar orbit, such as the laser altimeter (LALT) on the Selenological and Engineering Explorer (SELENE; Araki et al., 2008) mission, the laser altimeter on Chang'E-1 (Sun and Dai, 2005), the Lunar Laser Ranging Instrument (LLRI) aboard

the Chandrayaan probe (Kamalakar et al., 2005), or the Lunar Orbiter Laser Altimeter (LOLA; Smith et al., 2010) aboard the LRO mission, which is the only one still active today. Using a beam-splitter, LOLA generates five laser beams in every shot, which form a pattern on ground that allows to estimate two-dimensional slopes and roughness profiles (Kreslavsky et al., 2013). Since LRO is on a polar orbit (inclination of 89.7°) the north- and south pole are mapped with each revolution, while regions closer to the equator develop gradually as the Moon rotates below the satellite. With a resolution of about 60 m at the equator and a vertical accuracy of about 3 - 4 m root mean square (RMS) (Baker et al., 2016), LOLA currently provides the highest resolution and accuracy topography of any solid planetary body in our Solar System (Smith et al., 2017).

2.2.4 Moment of inertia

The moment of inertia I is defined as the measure of an object's resistance to rotational change, which is the ratio between the angular momentum L and its angular velocity ω around a principal axis, as

$$I = \frac{L}{\omega}. \tag{1}$$

Since this resistance depends on the radial mass distribution, the moment of inertia is an important measure for the inner structure of a planetary body. Even if the moment of inertia does not uniquely determine the vertical density structure, it provides important information about whether the density increases with depth or not. The normalized moment of inertia is defined as

$$\frac{C}{MR^2} \tag{2}$$

where C denotes the moment of inertia of the principal axis showing the highest moment of inertia (the rotational axis), R is the radius, and M the total mass of the body. The Moon has a normalized polar moment of inertia of 0.3932 (Konopliv et al., 1998), indicating a slight increase in density with depth. A value of 0.4 would indicate a homogeneous body and a moment of inertia above 0.4 refers to a decreasing density with depth.

2.2.5 Gravity field

The gravitational acceleration is defined as the free fall acceleration of an object in a medium without any (atmospheric) drag. This acceleration is caused by the force of gravitational

attraction (acting in opposite direction to the gravitational potential) of a certain mass. Newton's law of universal gravitation states that the attractive force F between two objects is directly proportional to the product of their masses m_1 and m_2, and inversely proportional to the square of their distance r, multiplied by the gravitational constant G from Einstein's field equations of general relativity, as

$$F = G\frac{m_1 m_2}{r^2} \tag{3}$$

If one mass is significantly larger than the other, the gravitational acceleration g of a spherical field source with a radius R and a total mass M may be expressed as

$$g = \frac{GM}{R^2}. \tag{4}$$

While for the gravitational acceleration the SI unit m/s^2 is used, smaller variations are often expressed in the unit Gal, defined as 0.01 m/s^2. Especially, when mapping gravity anomalies, which are variations in the gravity field deviating from the normal gravity field (approximating the true gravity), the unit Gal is a convenient alternative.

While the shape of the Earth's geoid (surface with equal potential) is best described by an ellipsoid, the most appropriate mathematical figure describing the normal gravity of the Moon is a sphere. The reason is that the effective potential (which is the sum of the centrifugal potential energy and the gravitational potential energy) for both objects is different. Compared to Earth, the Moon has a much lower angular velocity, with a full rotation around its axis in about 27.3 days. Consequently, the centrifugal forces on the Moon are much smaller compared to those on Earth, so that any equatorial bulk is formed.

With a mean surface gravity of 1.625 m/s^2 the Moon has an acceleration of about 17% compared to the mean gravity at the surface of the Earth (9.807 m/s^2). But the Moon possesses large variations in local gravity, deviating from the average gravity acceleration. Those variations provide constraints on structural parameters (e.g., crustal thickness) and the mass distribution below the surface, characterized by bulk density and porosity. Local variations in gravity may conveniently expressed in spherical harmonics, which are continuous functions for describing irregularities of the geopotential field across the surface of a sphere. Spherical harmonic functions divide the potential into different spectral frequency components, which are represented by a series of coefficients $\bar{c}_{lm}$ and $\bar{s}_{lm}$, where l and m represent the coefficients' degree and order (Appendix 6.1).

Lunar mascons

The most prominent features visible in the gravity field of the Moon are the so-called mascons, mass concentrations located in the centers of lunar impact basins, first detected by Muller and Sjogren (1968). Since the largest mascons are associated with basins having volcanic mare material in their centers (Figure 3), early studies related the mass concentrations to the high density of the mare basalts (Howard, 1970). Later, gravity and topography data obtained by Clementine (Nozette et al., 1994), rather indicated variations in the depth of the crust-mantle boundary (Neumann et al., 1996), in particular a thinning of the lunar crust, which may be explained by the excavation of the crater cavity.

The gravity field observations from the GRAIL satellite mission (Zuber et al., 2013a), which will be explained in detail below, confirmed that volcanic magma emplacement may not be the main reason for positive gravity anomaly in the centers of basins. Numerical simulations showed that mascons are most likely the consequence of a postimpact isostatic adjustment, as a result of cooling and contraction of the center melt pool, which causes an uplift of mantle material (Melosh et al., 2013).

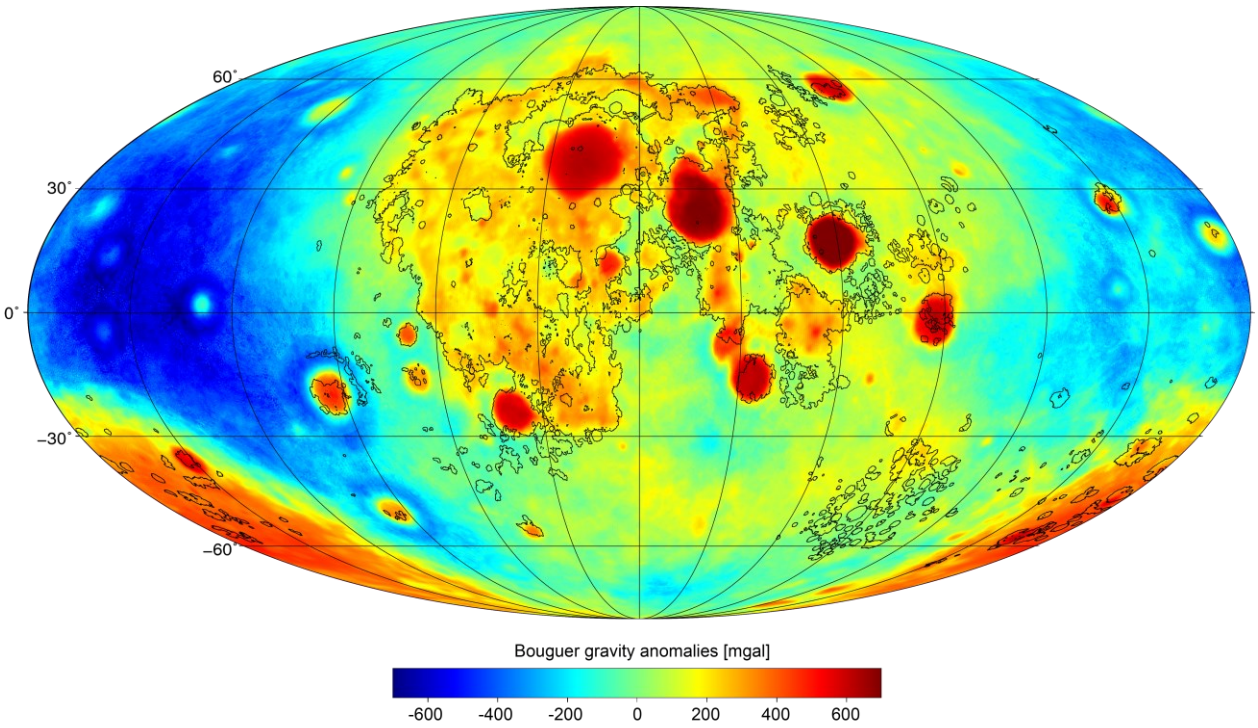

Figure 3: Global Bouguer gravity anomalies (ρ = 2550 kg m^{-3}), mapped in Mollweide projection, centered at the lunar nearside (0° East, 0° North). Regions of mare basalt are marked with black outlines (Nelson et al., 2014).

SELENE mission

The SELENE mission (Kato et al., 2008), better known by its new given name Kaguya, obtained the first gravity field model of the lunar farside from direct observations (Namiki et al., 2009). Gravity field mapping was realized by four-way Doppler measurements, where two relay subsatellites were used to track the main spacecraft at the lunar farside.

With SELENE a global gravity field model of the Moon developed up to degree and order 90 was derived, corresponding to a spatial resolution of about 60 km. Combining the low-frequency gravity field models with the gravity potential derived from topography, gravity field models of higher resolution (1.5 km) could be obtained (Hirt and Featherstone, 2012).

GRAIL mission and data

Data from the Gravity Recovery and Interior Laboratory (GRAIL) satellite mission represent an important milestone regarding our knowledge about the crustal structure of the Moon. The GRAIL gravity field models have a higher spatial resolution and accuracy compared to any other planetary body in our Solar System. The mission design is similar to the successful Earth-orbiting Gravity Recovery and Climate Experiment (GRACE; Tapley and Reigber, 1999) and the GRACE Follow-On (GRACE-FO) mission (Flechtner et al., 2014). Here, measurements of the changes in the line-of-sight distance between two co-orbiting satellites are used as observables for determining monthly gravity field solutions. GRAIL was equipped with the Lunar Gravity Ranging System (LGRS), where changes in satellite-to-satellite distance were monitored through phase measurements of a KA-band carrier signal (Klipstein et al., 2014). Even when spacecraft separation was large (between 40 km and 225 km), range rates were estimated with an accuracy of 0.03 μm s^{-1} for the primary mission (March 1, 2012 until May 29, 2012) and 0.05 - 0.07 μm s^{-1} for the extended mission (August 30, 2012 until December 14, 2012), as a function of the sampling intervals of 5 s and 2 s, respectively (Lemoine et al., 2014). The measurements were post-processed by two independent NASA analysis groups, at the Jet Propulsion Laboratory (JPL) and Goddard Space Flight Center (GSFC).

While GRACE uses the Global Positioning System (GPS) for time synchronization and absolute positioning of the two spacecraft, the GRAIL satellites were tracked from Earth by the Deep Space Network (DSN) using two-way Doppler measurements (S-band). A Time Transfer System (TTS) synchronized the clocks of the two satellites and the ground station via S-band. A one-way X-band link was used for sending data from the satellites to the ground stations of the DSN (Asmar et al., 2013). Figure 4 illustrates the radio link scheme of GRAIL.

An important parameter for the final resolution of the derived gravity field model is the altitude of the two spacecraft above the ground. Since the gravity field signal attenuates with increasing distance to the body, measurements from lower altitudes result in a higher spatial resolution, though limited in coverage. During the primary mission, the average altitude of the GRAIL orbiters was 55 km. For mapping regions of interest in higher resolution, in the extended mission phase the orbit of the spacecraft was lowered down to a mean altitude of about 23 km. In the final stage of the mission, the periapsis altitude was even lowered down to 5 km, leading to an enormous increase in resolution, such that the gravity field of Orientale basin was mapped with a resolution of about 3 - 5 km (Zuber et al., 2013a). Apart from the altitude of the spacecraft, the inclination of the orbit is of great relevance for the sensitivity to different spherical harmonic coefficients. While satellites in a polar orbit are sensitive to changes in north-south direction (zonal terms) a lower inclination results in higher accuracy for sectoral and tesseral terms of the recovered gravity field (e.g., Kaula, 1966; Emeljanov and Kanter, 1989).

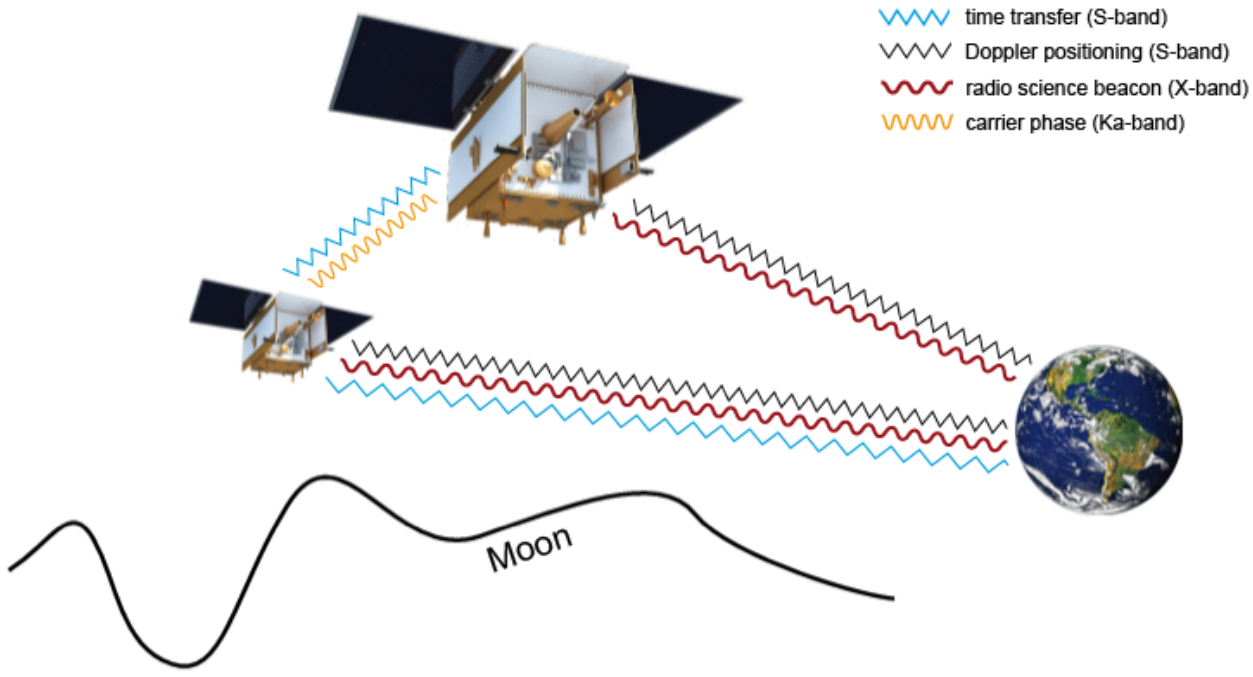

Figure 4: Scheme of the GRAIL satellite radio links. Changes in distance between both satellites are determined via KA-band carrier phase measurements. S-band is used for Satellite-to-satellite link for time synchronization between the satellites as well as time synchronization with the ground stations, and absolute positioning. Downlink is realized via X-band. The modified sketch is adopted from Asmar et al. (2013).

From extended mission data in combination with advanced processing strategies, the resolution and accuracy of the gravity field models could be greatly improved (Lemoine et al., 2014). A summary of different GRAIL gravity model releases is given in Table 1. Due to variations in spatial sensitivity of the tracking data (mainly caused by different orbit conditions) a constant constraint (Kaula power law constraint; Kaula, 1966) based on topographic information is added to the higher degree coefficients to limit spurious power (Goossens et al., 2017). The improvement in accuracy in contrast to the unconstrained model is shown in Figure 5, where the RMS power spectra of three different gravity models are given (Lemoine et al., 2014). While the accuracy for the unconstrained model attenuates at about degree 650, the RMS of the corrected model shows a constant trend with an enhanced RMS.

Table 1: Gravity field solutions derived from GRAIL tracking data, divided according to the two analyses centers.

Goddard Spaceflight Center (GSFS)					
Model name	Model resolution	Release year	Mission data	Half-wavelength resolution [km]	Reference
GRGM420A	420	2012	primary	13.0	Zuber et al. (2013b)
GRGM540A	540	2013	primary	10.1	Lemoine et al. (2013)
GRGM660PRIM	660	2013	primary + extended	8.3	Lemoine et al. (2013)
GRGM900C	900	2014	primary + extended	6.1	Lemoine et al. (2014)
GRGM1200A	1200	2016	primary + extended	4.5	Goossens et al. (2016)
Jet Propulsion Laboratory (JPL)					
Model name	Model resolution	Release year	Mission data	Half-wavelength resolution [km]	Reference
GRAIL420C1A	420	2012	primary	13.0	Konopliv et al. (2013)
GL0660B	660	2013	primary	10.1	Konopliv et al. (2013)
GL900C	900	2014	primary + extended	8.3	Konopliv et al. (2014)
GL0900D	900	2014	primary + extended	6.1	Konopliv et al. (2014)
GL1500E	1500	2016	primary + extended	3.6	Park et al. (2015)

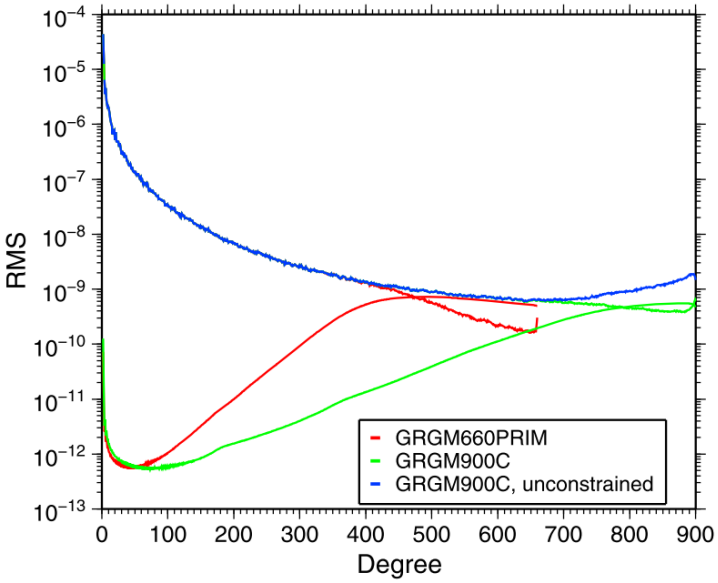

Figure 5: Power spectra of gravity model GRGM660PRIM (primary mission data), GRGM900C (primary and extended mission data) with and without applied Kaula power law constraints. In addition, the power spectra of the uncertainties for GRGM660PRIM and GRGM900C are given (Lemoine et al., 2014).

2.2.6 Joint analysis of gravity and topography

Gravity field data in combination with surface topography may constrain geophysical parameters of a planetary body.

The relation between gravity and topography may be expressed analytically by the admittance Z (Eq. 5), solving for the bulk density and the thickness of the elastic lithosphere (e.g., McKenzie and Fairhead, 1997), which again allows to derive further conclusions, e.g., about the surface heat flow (McGovern et al., 2004). If gravity and topography are expressed in spherical harmonic functions, the correlation between the gravity field coefficients C_{lm} and the topography coefficients T_{lm} is obtained as a function of the wave number l

$$Z(l) = \frac{S_{tg}(l)}{S_{tt}(l)} \tag{5}$$

with the cross- and auto power spectra S being

$$S_{tg}(l) = \sum_{m=-l}^{l} T_{lm}\, C_{lm} \tag{6}$$

$$S_{tt}(l) = \sum_{m=-l}^{l} T_{lm}\, T_{lm} \ . \tag{7}$$

McKenzie (1994) demonstrated that for long wavelengths the support is isostatic, characterized by an admittance of about zero. The short wavelength portion of the gravity field signal is independent from the bending of the crust-mantle interface (lithospheric flexure) and may therefore be used for the determination of the bulk density of crustal materials.

Analyzing the admittance between the short wavelength gravity field signal and topography, Besserer et al. (2014) found that for the anorthositic highlands on the lunar farside the bulk density increases with depth at an average gradient of about 35 kg m^{-3} km^{-1}. However, prominent mare regions located on the lunar nearside possess a distinct decrease in density with greater depth. This effect is caused by dense mare basalt overlying anorthositic rock of lower density.

A different method for estimating bulk density in the spectral domain, uses a fractal-based approach (e.g., Chapin, 1996; Satya Kumar et al., 2017). Many geophysical processes may be described in fractal terms, meaning that they are scale invariant. Topography has also been determined to behave fractally (Turcotte, 1992), unlike the gravity field, which is of mixed nature, having a scale invariant part (from topography) and a scale-dependent part (from specific geological density distributions) (Chapin, 1996). The objective is to find the density that minimizes the topographic effects on the Bouguer anomalies, consequently, the one showing less fractal components. Satya Kumar et al. (2017) applied the method to a large region in the lunar highlands on the Moon's farside. Since in the region of interest several impact basins are located, containing dense mare basalts in their centers, the estimated average bulk density of the highland crust of 2700 kg m^{-3} is significantly higher than in other studies.

Apart from the spectral analysis, lateral variations in bulk density can also be solved in the spatial domain, as described by Wieczorek et al. (2013). By minimizing the correlation between the short wavelength portion of the gravity field signal and the local topography, bulk density is estimated (see the two publications in the main part of this work for details, Section 3.3.1 and Section 4.2).

The combined analysis of topography and gravity also allows to solve for the thickness of the crust (Wieczorek, 2009). Since the observed gravity field signal is sensitive to abrupt density changes (Wieczorek and Le Feuvre, 2009), Bouguer anomalies may reflect the density contrast at the interface between the crust and the mantle. Consequently, mass changes visualized by Bouguer anomalies, are solely a result of crustal thickness variations (e.g., Phillips et al., 1973; Zuber al., 1994). Several assumptions are included in the construction of a crustal thickness model: (1) the observed gravity field signal originates from the surface relief as well as the crust-mantle boundary only. (2) The bulk density is constant for the crust and the mantle. (3) A mean crustal thickness must be pre-defined, since Bouguer gravity anomalies are sensitive to

subsurface mass changes, but insensitive to an absolute depth. Therefore, assigning an initial mean crustal thickness is necessary (Phillips et al., 1973). Minimizing the differences between the assigned and observed Bouguer gravity, the depth of the crust-mantle boundary may be computed with the following equation from Wieczorek and Phillips (1998) as

$$h_{lm} = \omega_l \left(\frac{C_{lm}^{BA}\, M\, (2l+1)}{4\,\pi \Delta\rho D^2} \left(\frac{R}{D}\right)^l - D \sum_{n=2}^{l+3} \frac{(h^n)_{lm}}{D^n\, n!} \frac{\prod_{j=1}^{n}(l+4-j)}{(l+3)} \right) \tag{8}$$

with

$$\omega_l = \left(1 + \lambda \left[\frac{M(2l+1)}{4\,\pi \Delta\rho D^2} \left(\frac{R}{D}\right)^l \right]^2 \right)^{-1} \tag{9}$$

where C_{lm}^{BA} are the Bouguer anomaly coefficients of radius R, downward continued to a reference radius D. The density contrast at the crust-mantle interface is denoted with $\Delta\rho$. The term ω_l acts as a filter, stabilizing the downward continuation process, with λ being a Lagrange multiplier.

Global maps of the crustal thickness of the Moon reveal a thinning of the crust in the central regions of large impact basins (Neumann et al., 1996; Wieczorek et al., 2013). Furthermore, there is a striking asymmetry between the crustal thickness of the nearside and the farside of the Moon. Studies by Wieczorek et al. (2013) revealed a crustal thickness with values of 30 - 40 km for the nearside and about 50 - 60 km for the lunar farside. The differences in crustal thickness between both hemispheres as well as their different surface appearance of large and smooth mare regions on the Earth-facing side and heavily cratered and bright landscapes on the side facing away from Earth, is still not fully understood. Zhu et al. (2019) suggest that the disparity of crustal thickness between both hemispheres may be the result of a giant impact on the young Moon. Their results (in terms of elevation, crustal thickness, and mineral composition) using numerical models simulating such an impact match well with today's observational data.

2.3 Impact craters and basins

While until the 1950s it was assumed that craters on the Moon were formed by volcanic activity, today we know that the vast majority of the craters originate from impact processes (Shoemaker, 1962; Melosh, 1989). Lunar rock samples, brought to Earth by the Apollo astronauts, show traces of shock-metamorphism, indicating a formation through meteorite impacts (Engelhardt et al., 1970).

The Earth-Moon-System is assumed to be exposed to the same impactor populations. However, the lunar surface is covered by thousands of impact craters with diameters of up to 2400 km, while only 190 confirmed impact structures are currently listed in the Earth Impact Database (Earth Impact Database, 2011), with the largest crater being Vredefort, having a diameter of only ~250 km (Henkel and Reimold, 1996). While craters on Earth are routinely erased by effects of atmospheric erosion, sedimentation, and tectonism, the Moon is an undynamic body, where these effects are lacking. Impact structures with ages of about 3.9 - 4.5 Ga, when the Moon just had formed, are still preserved.

Impact craters possess a distinct morphology, characterized by a circular depression and an elevated outer rim. In addition, they exhibit unique geophysical anomalies, which can be identified by remote sensing techniques. Mapping the magnetic and the gravitational field are most suitable for finding and identifying impact craters and basins, possibly supplemented by seismic experiments and the measurement of electric resistivity (Pilkington and Grieve, 1992). To distinguish impact craters from circular depressions of other origin (e.g., volcanic calderas or sinkholes) it is instructive to study the geology of the crater. Since hypervelocity impacts cause peak shock pressures of more than 100 GPa (French, 1998) the shock wave modifies rock and minerals in a distinctive way. Figure 6 depicts zones of initial shock wave pressures in dependency to the point of impact (Meyer, 2012). While pressures above 50 GPa cause vaporization and melting of rock, shock metamorphism effects are expected to occur at pressures starting from 5 GPa. Those shock metamorphic effects vary with the pressure magnitude (French, 1998), which is dependent on the distance from the point of impact. Most reliable shock metamorphism effects, which can be found at impact craters are (1) microscopic planar deformation features (PDF), located in quartz, feldspar, and other minerals (French, 1998) and (2) megascopic shatter cones (Figure 7). Those cone-like, striated fractures in rock can be found in the center peak region or at the rim of impact craters (Wieland et al., 2006). Even beyond the shock metamorphism zone the target rocks may show fracturing and brecciation, increasing the porosity of the affected material. Another indicator may be the geochemical evidence for remnants of the extraterrestrial meteorite projectile, even not many impactor fragments have been found in craters yet (Tagle and Hecht, 2006).

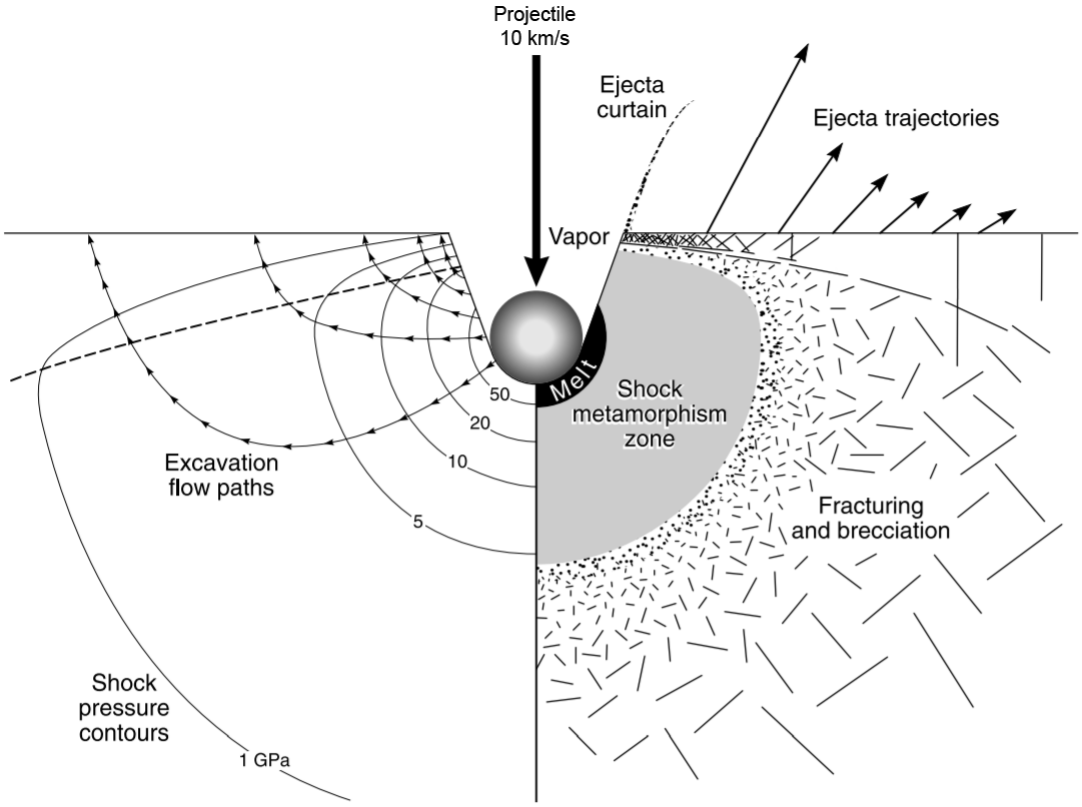

Figure 6: Schematic cross-section of the contact and compression stage of a meteorite impact. On the left contour lines of initial shock pressures and flow lines of excavation are shown. On the right, effects are depicted, which occur at certain pressures, like melting of rock, effects of shock metamorphism, and brecciation of rock (Melosh, 1989; modified by Meyer, 2012).

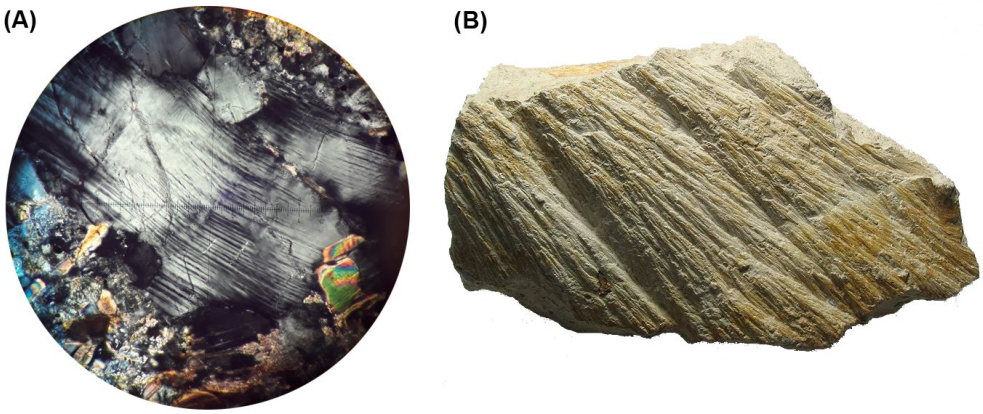

Figure 7: (A) Microscopic image of planar deformation features (PDS) in quartz grains and (B) shatter cone with a size of about 13 cm, found at Steinheimer Becken, Germany (Raab, 2009).

2.3.1 Classification of lunar impact craters

The Moon hosts a large inventory of impact craters of various sizes, ranging from a few meters up to hundreds of kilometers in diameter. The morphologies of these impact structures depend on the properties of the projectile (size, velocity, impact angle, and material) and the characteristics of the target (composition, porosity, and temperature). Depending on their different characteristics, impact structures can be subdivided into different classes:

(1) *Simple craters* (Figure 8A) have the shape of a truncated cone (Garvin et al., 2011). The floor of the crater is filled with breccia, consisting of a mixture of melt-bearing allochthonous rock (formed elsewhere and moved to the current location) and slump material of the steep crater walls (Osinski and Pierazzo, 2013). Simple craters represent the group of the smallest candidates with diameters up to 17 km for craters located in the highlands, and up to 14 km for craters in the lunar maria (Krüger et al., 2018). Their depth to diameter ratio is about 1/5 (Kenkmann et al., 2013).

(2) *Transitional craters* (not to be confused with the term transient crater; see Section 2.3.2) are building a link between simple and complex impact structures (Figure 8B). The morphology of a transitional crater shares characteristics of both crater classes, having steep crater walls similar to simple craters, but on the other hand a large and flat floor, similar to complex craters (Cintala and Grieve, 1998).

(3) *Complex craters* (Figure 8C) owe their name to their structurally complicated morphology. Large, circular zones of stepped terraces form the crater wall (French, 1998). In the center a distinctive central peak can be found, surrounded by a flat crater floor. The observed features of complex craters are caused by the gravitational adjustment of the initial crater during the modification stage of crater formation (see Section 2.3.2). Due to an inward movement of material, the central uplift is formed (Hartmann and Wood, 1971). The depth to diameter ratio for complex craters varies between 1/10 and 1/20 (Kenkmann et al., 2013).

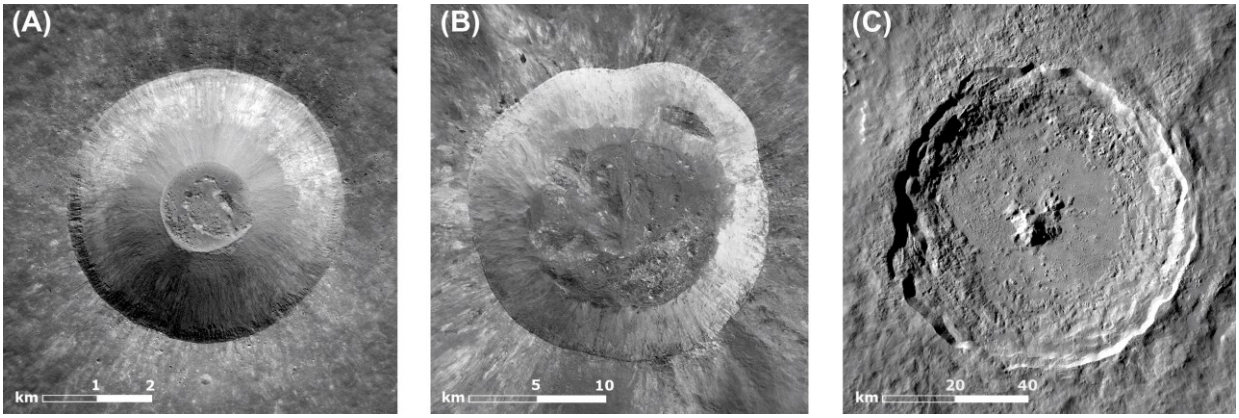

Figure 8: LROC NAC north-facing image mosaics (LROC NAC NASA/GSFC/Arizona State University) of impact craters on the Moon. (A) Simple crater Lichtenberg B, (B) transitional crater Giordano Bruno, and (C) complex crater Tycho.

(4) The largest structures formed by meteorite impacts are *basins*. The projectiles must have been large, with about 10 to 20 km in diameter (Reimold and Gibson, 2009), impacting at high velocities (20 km/s) (Stuart and Binzel, 2004). Basins can be subdivided in further classes. There are (a) basins without any interior ring, due to their small dimension or removed by postimpact modifications, (b) peak-ring basins, characterized by two circular rings, one forming the outer rim crest, the other is located inside the basin, with a radius which is about half of the dimension of the main rim (Neumann et al., 2015), and (c) multi-ring basins, with more than two concentric topographic rings (Hartmann and Wood, 1971). Examples of the different types of impact basins are given in Figure 9.

The crater floor of a basin appears to be flat and shallower (relative to its size) compared to complex craters (Baker et al., 2011). Many impact basins are either partially or fully filled with mare basalt, triggered by magmatic intrusion after crater formation (Hartmann and Wood, 1971). Since basins belong to the oldest impact structures on the Moon, the surface morphology of many basins is highly degraded due to subsequent impact events. For some basins, topographic features, like an inner depression or an elevated crater rim, are difficult to detect or destroyed, so that only their geophysical properties can be used as a reference (Neumann et al., 2015).

The geophysical properties of impact basins differ significantly from those of simple or complex craters. Data from the GRAIL mission reveal that impact basins exhibit a distinct gravity bullseye pattern (Figure 10), characterized by a large positive anomaly in the center surrounded by a gravity low (see Section 2.2.5).

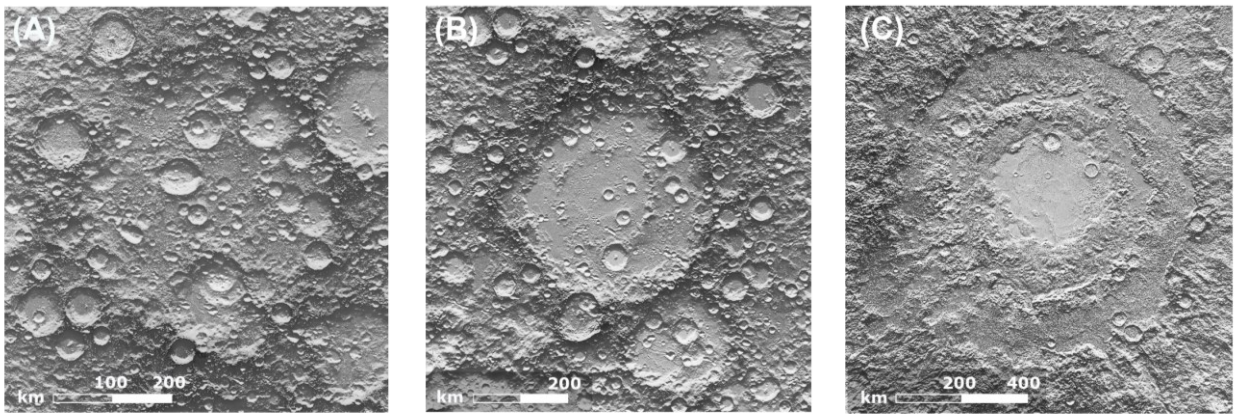

Figure 9: Shaded topographic relief of the (A) Dirichlet-Jackson basin having only an outer rim, (B) peak-ring basin Korolev, and (C) the multi-ring basin Orientale. The Mercator projected, north-facing maps are derived from LOLA data.

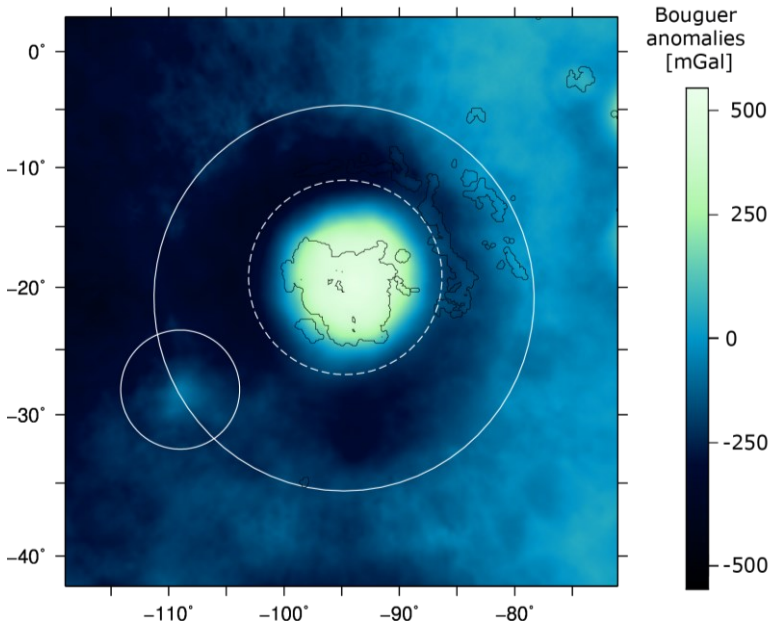

Figure 10: Mercator projected map of Bouguer gravity anomalies (ρ = 2550 kg m^{-3}) of Orientale basin (center) and Orientale South-West. The solid line marks the outer rims and the dashed line the peak ring (Neumann et al., 2015).

Different transition diameters from (lunar) complex craters to impact basins can be found in the literature. While some studies define the transition at a radius of 300 km, depending on morphological features, solely, Soderblom et al. (2015) found that the mantle uplift occurs for highland craters with diameters larger than 218 km. Since for impact basin recognition the geophysical characteristics play a role as important as the morphological features, it stands to reason to define the transition diameter at about 200 km, where the geophysical characteristics of the impact craters change. In Figure 11 schematic profiles of the topography and the Bouguer gravity anomalies of a complex crater (left) and a peak-ring basin (right) are shown.

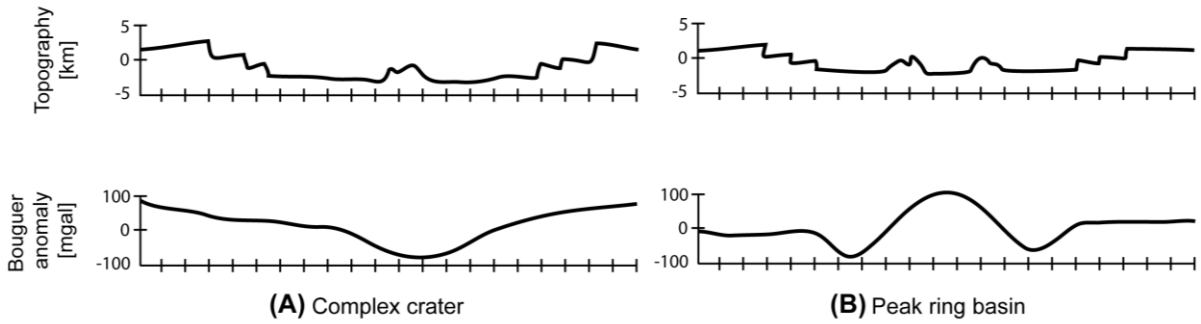

Figure 11: Schematic representation of topography (top) and Bouguer anomalies (bottom) for (A) complex craters and (B) peak-ring basins, showing different morphologic and gravitational characteristics.

2.3.2 Impact crater formation process

Crater formation can be best described by three distinct stages, which are dominated by different physical forces and mechanics (Gault et al., 1968; Melosh, 1989; French, 1998):

(1) *Contact and compression stage*: This stage of crater formation begins, when the projectile, travelling with hypervelocity of 15 - 30 km s^{-1}, contacts the target surface. The projectiles kinetic energy is transferred into the target rock and converted into high-pressure shock waves, radiating radially from the point of impact. While the peak pressure close to the point of contact can reach values larger than 100 GPa, the shock wave energy declines rapidly with distance. Besides from the effect of geometric spreading, energy is lost to the target rock by heating, compression, and fracturing. The target properties, such as porosity or strength, affect the shock wave propagation. In target material of high porosity, the shock pressure attenuates faster, and also the melt production close to the point of impact is increased compared to targets of lower porosity (Wünnemann et al., 2008). When the pressure is reduced to values of about 2 GPa, the shock waves turn into elastic or seismic waves, still causing fracturing and brecciation of rock as well as faulting, and landslides. All of this happens very fast: Even for large basins, the contact and compression stage lasts a maximum of only a few seconds.

(2) *Excavation stage*: In this stage the actual impact crater is formed. Since the projectile already penetrated the target and travelled inside, some of the shock waves are emitted upwards and are reflected at the surface as so-called release waves. Due to this process, a part of the shock wave energy is converted back into kinetic energy, accelerating the involved rock. A symmetric excavation flow is produced, in which the material close to the surface is moved upwards and sideways (forming an ejecta curtain), and lower material downwards and

sideways. The material in the upper part is accelerated to very high velocities, moving the material kilometers away from the center of impact. A bowl-shaped transient crater is formed, which is more of theoretical nature than a real crater, since for different regions within the crater this stage is reached at different times. Therefore, a clear determination of the transient cavity becomes difficult. Approximations for the transient crater are useful, e.g., when the volume of the crater is largest. The excavation phase is completed after less than 2 minutes. A terrestrial crater with a dimension of 200 km occurs in about 90 seconds (Melosh, 1989).

(3) *Modification stage*: After the transient crater has been completely formed, the modification stage begins, with its dominating physics being gravity and rock mechanics. The modifications depend on the size of the transient crater as well as its structure and the target rock properties, forming different types of craters (see Section 2.3.1). While some modifications happen immediately after the end of the excavations stage, other processes require longer time scales. The excavated ejecta forms a blanket on the surface around the crater, and loose material from the crater walls slides down the cavity and deposits breccia inside the crater. Since other effects such as isostatic adjustment (mantle uplift) or viscoelastic relaxation last longer, a clear marked end of the stage is not easy to define.

Our current knowledge about the formation of impact craters and how the target material is modified is based on four pillars: (1) experiments performed in the laboratory, simulating hypervelocity impacts, (2) observations of physical effects on rock and soil at nuclear test sites, (3) numerical models that simulate the impact cratering process, and (4) observations of geological and geophysical characteristics of impact craters on Earth and other planetary bodies. Numerical simulations are used to complement small scale laboratory experiments, especially when it comes to the effect of individual physical parameters involved in the formation process of large structures (Collins et al., 2012). The outcome of the modelling process is best constrained by observational data. However, when considering the impact basins, it should be noted that the characteristics changed in the long time period between the end of their formation process and the measurements which are performed today.

2.3.3 Age determination of impact basins

The timing of basin forming events is a significant key for understanding the evolution of the early Solar System (Shoemaker and Hackmann, 1962; Tera et al., 1974). Variations in the impactor flux as well as changes of the impactor population have been suggested by analyzing the lunar basin record (Head et al., 2010). Different methods are used to estimate the time when the impact basins have been formed.

Late Heavy Bombardment

After the differentiation of the terrestrial planets, a high flux of various types of interplanetary matter (rocky fragments as well as gas-rich comets) persisted for several hundred million years following planetary accretion (Taylor, 1989). The lithospheres of the inner planets just stabilized, such that craters formed by impacts could be preserved. The observed frequency and ages of these craters have been used to obtain models of the flux. Melt intrusions in highland rock samples, likely to have emerged through impact shocks, were found to have formed approximately 3.9 - 4.5 Ga ago, assigning absolute ages to the impact events.

While the existence of the Late Heavy Bombardment is undisputed (Morbidelli et al., 2018), different hypotheses exist, how the impactor flux of objects, including planetesimals, asteroids, and comets, developed with time. Today's debate generally focuses on two possible interpretations (Figure 12) of the record:

(1) The *cataclysm* scenario suggests a spike in the declining impactor rate (Tera et al., 1974; Marchi et al., 2012), explaining the concentration of samples dated with an age of 3.9 Ga, either formed by a population of planetesimals left over from accretion (Morbidelli et al., 2001) or from asteroid belt objects (Walsh et al., 2011). There are different theories explaining the spike in the impactor rate. The most prominent is the Nice model (Gomes et al., 2005; Morbidelli et al., 2005; Tsiganis et al., 2005), which explains the spike in the impactor flux by a migration of the giant planets in the early Solar System. The migration causes strong resonance effects, bringing a vast amount of material into the inner Solar System. (Gomes et al., 2005). Various geologic, chemical, and dynamical arguments have been discussed supporting alternative cataclysm models (Ryder et al., 2000; Kring and Cohen, 2002; Norman and Taylor, 2005; Bottke et al., 2007; Trail et al., 2007).

(2) The *accretion tail* scenario suggests a monotonically decay with time, caused by a steady decline of leftover objects, due to collisions and dynamical effects. While in this theory the highest flux rates exist at the time of terrestrial planet formation, the dominance of impact ages around 3.9 Ga is explained by sampling biases, due to a reset of K-Ar ages caused by lunar magmatism and overprinting from subsequent impact events (e.g., Boehnke and Harrison, 2016; Michael et al., 2018).

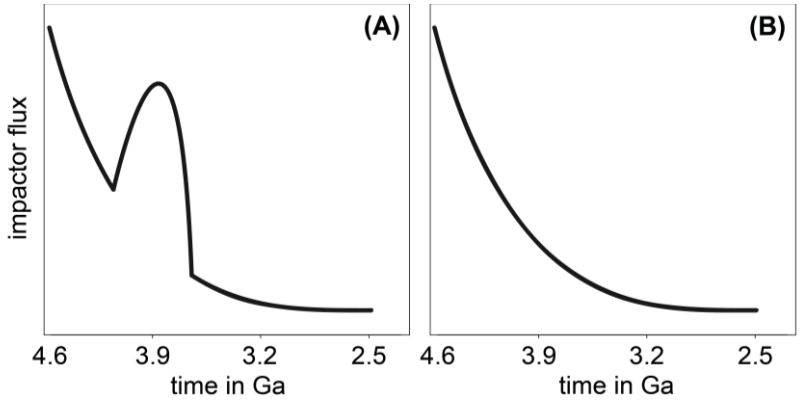

Figure 12: Two possible models of the Late Heavy Bombardment: (A) Lunar cataclysm and (B) accretion tail.

Formation sequence using stratigraphy

The most obvious approach for determining formation sequences of adjacent craters is their stratigraphy (Wilhelms, 1987), i.e., the observed superposition of craters and ejecta (see example in Figure 13). While this method provides indisputable references to the sequence of impact events, a disadvantage is that the craters must be in close proximity with direct contact to each other. Neither relative nor absolute ages can be determined based on the stratigraphy of impact craters and basins.

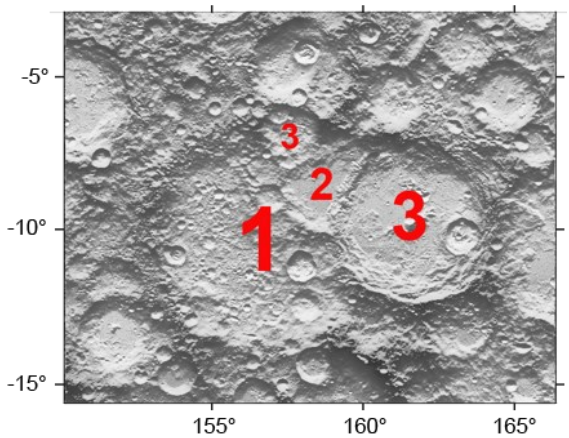

Figure 13: Shaded topographic map of Keeler West basin, derived from LOLA data. The stratigraphy reveals the sequence of crater formation (labeled with red numbers).

Crater statistics for relative age determination

A common technique for assigning relative ages to planetary surfaces is based on the statistics of impact craters. The method is based on two assumptions: First, crater formation is a geographically random process, and second, processes destroying the craters proceed much slower than craters are formed (McGill, 1977). The basic idea is that a surface with a larger number of impact craters of different sizes is older than a geological defined unit with fewer craters and smaller crater sizes. Counting and measuring each crater diameter within a certain region, the crater size-frequency can be set up, which is given as the crater diameter against the cumulative number of craters per square kilometer (Shoemaker et al., 1963; Baldwin, 1964). Neukum et al. (1975) showed that the lunar crater size-frequency distribution for areas of different ages can be modeled by the same function, the so-called production function (PF). Applying a least-squares fit, the production function can be adapted to the crater size-frequency distribution of individual geological units (Figure 14), so that relative ages can be found by considering the vertical offset.

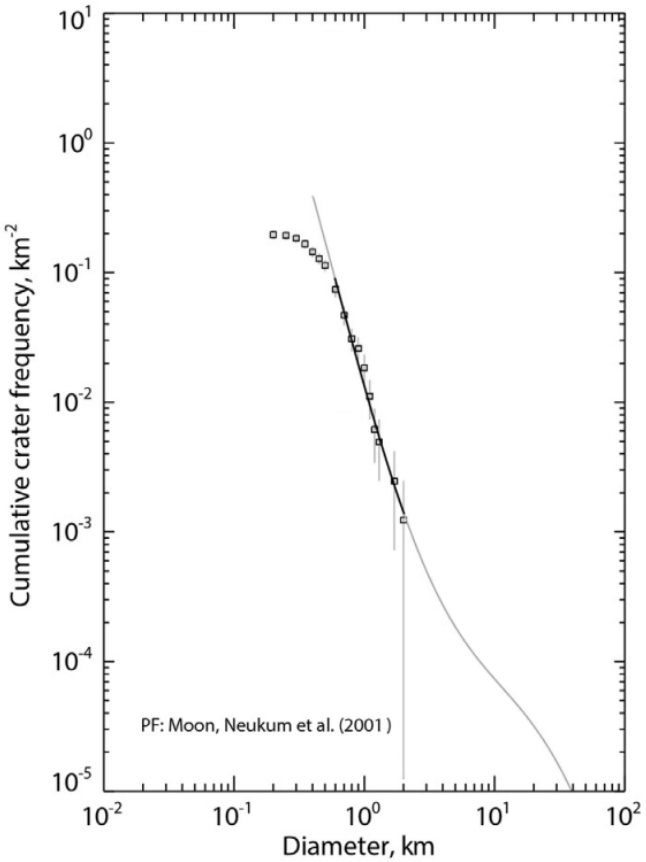

Figure 14: Crater size-frequency distribution with the least-squares fitted production function.

Radiometric dating of lunar rocks

By measuring the abundances of naturally occurring radiogenic isotopes in rocks and minerals and comparing them with their decay products, absolute ages can be determined. For the timing of an impact event, most important are the melt inclusions (minerals and glasses) in lunar rock samples. The induced temperatures during an impact are sufficient high to produce a large amount of melt, for which the isotopic clock has been reset. Therefore, it is theoretically possible to date a particular impact event using radiometric methods, which yield the last crystallization age (Stöffler and Ryder, 2001). Different decay systems may be used for this purpose, such as the rubidium-strontium (Rb-Sr), the samarium–neodymium (Sm-Nd), and the uranium-led (U-Pb) method. The potassium-argon (K-Ar) as well as the associated argon-argon (^{40}Ar-^{39}Ar) method are the most common techniques for dating impact melt. While the K-Ar dating method may be used for the timing of very early events in the lunar history (potassium decays with a half-life of 1.248 x 10^9 years), but is technically difficult, the ^{40}Ar-^{39}Ar method has the advantage of being applicable to fine-grained crystalline rocks and glasses (e.g., Hartung et al., 1971; Bottomley et al., 1990).

Absolute model ages

Combining the ages of radiometric dated rock samples with the geological unit, where the rocks have been found, the measured crater population can be linked and calibrated to an absolute age. The relationship of the crater size-frequency distribution as a function of radiometric age, is referred to as lunar cratering chronology (Figure 15). It can be approximated by a polynomial function, the so-called chronology function (CF), describing a constant cratering rate going back about 4 Ga (Hartmann et al., 1981; Neukum, 1983). Using the production function to extrapolate the measured crater size-frequency distribution of a geological unit to a reference diameter (1 km), the frequency leads to an absolute model age from the chronology function.

In a range between 1 and 3 Ga the chronology function is not supported by any data points. Age dating of rock samples, recently brought to Earth by the Chang'e 5 mission (Pei et al., 2015), which landed in the Mons Rümker area, a volcanic complex which include a suite of the youngest mare basalts (~2.0-1.0 Ga) on the lunar surface (Hiesinger et al., 2011), may constraint the chronology function in this area.

The statistical approach in combination with the stratigraphy is a powerful tool for determining relative and absolute ages of impact basins, although there are some challenges. One problem are secondary craters, which may bias the crater count (Bierhaus et al., 2005). Secondary

craters are formed by the ballistically ejected material of primary craters, leading to a higher count. Usually, the upper part of the crater size-frequency distribution, where the smallest diameters are depicted, shows a fall-off, which is a consequence of the limited resolution of the image data (Michael and Neukum, 2010). A steep slope of the crater size-frequency distribution in this area is an indication for contamination through secondaries (Hartmann and Wood, 1971).

Another problem which might question the entire approach of absolute age dating is the connection between the dated rock sample and the surface unit, where the sample has been found. The determined absolute age of the sample together with the crater size-frequency distribution of the geological unit serves as an anchor point for the chronology function. The determination of absolute ages of certain areas therefore only works under the assumption that the rock certainly originates from the location where it was collected. But there are two major problems: First, since rocks are accelerated to very high velocities in the course of impact crater formation, it is expected that ejecta covers large distances between the target area and the fall point (Michikami et al., 2007). Thus, it is very likely that a collected rock originates from a place other than where it was found. Second, impact melt is exposed to a complicated diffusion process through subsequent impacts of different sizes (Liu et al., 2019). Impact melt originating from a particular event may get re-melted, excavated, buried, and re-excavated (impact gardening), shaping a complex structure of impact melt from different events.

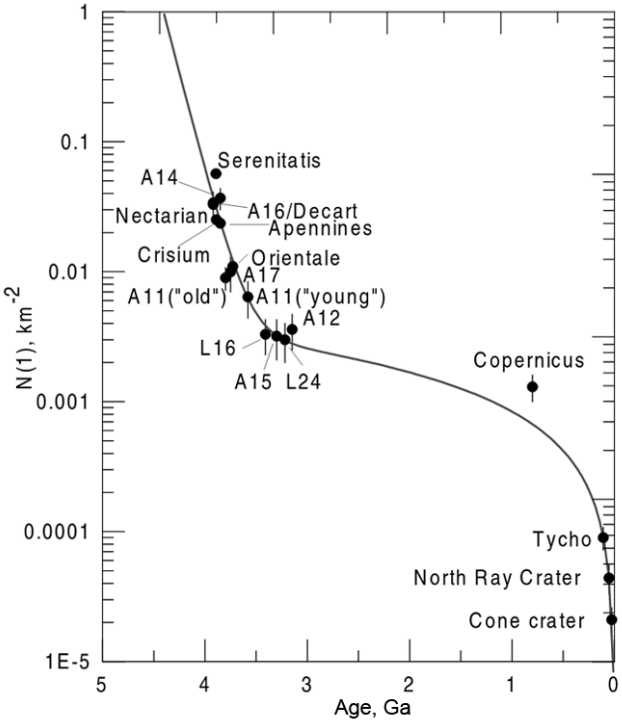

Figure 15: Lunar cratering chronology data points from Apollo and Luna landing sites (Stöffler and Ryder, 2001) together with the polynomial chronology function (Neukum, 1983).

Correlation of lunar basin ages and gravity signature

Based on the lunar impact basin inventory presented by Neumann et al. (2015), we tested for a correlation between the formation time of lunar basins and their gravity signal, aiming on a further method for determining the formation sequence of lunar basins (Wahl and Oberst, 2017).

Bouguer gravity anomalies of lunar impact basins reveal a distinct bullseye pattern, involving a positive Bouguer anomaly in the center surrounded by a gravity low. Neumann et al. (2015) found that larger basins show a more pronounced *Bouguer anomaly contrast* than smaller basins. Even if there is a clear linear trend (Figure 16), the scattering of the points indicates further influences.

Since the lithosphere of the Moon was much warmer and less viscous in the past, when the Moon just had formed, structures that were created by meteorite impacts probably relaxed fast. For later events, when the interior was colder and thus more viscous, basin relaxation probably was slow. Consequently, older basins would reveal a small Bouguer anomaly contrast, compared to young basins. However, no correlation between the gravity signature and the formation sequence of lunar basins could be found. We suggest that in addition to age, other factors like different thermal conditions or variations in thickness of mare infill in the center of lunar basins have a major impact on the gravity signal of lunar basins.

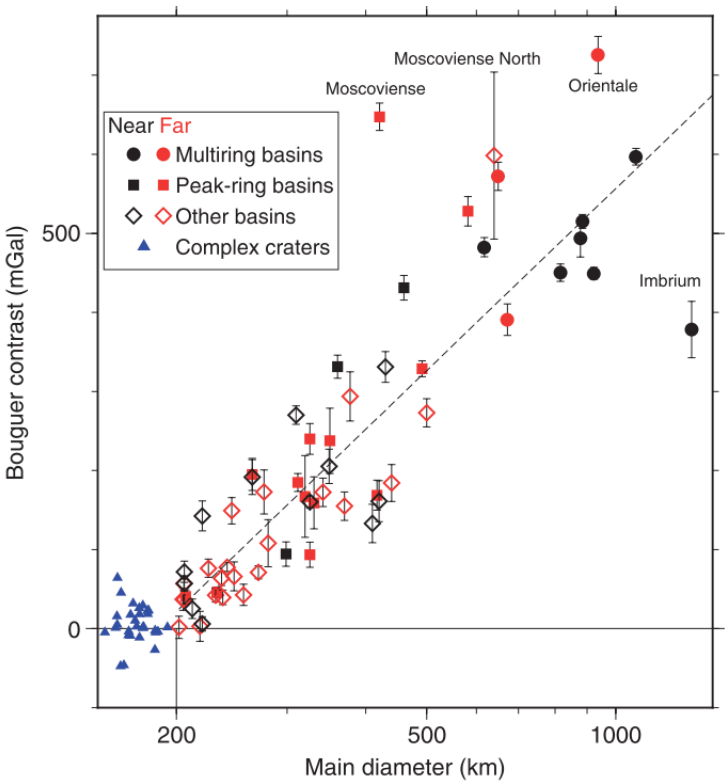

Figure 16: Bouguer anomaly contrast as a function of the diameter of lunar complex craters and impact basins (Neumann et al., 2015).

References

Aki, K. and Richards, P.G. (2002) Quantitative Seismology, 2nd edition. University Science Books, pp. 2002.

Araki, H., Tazawa, S., Noda, H., Tsubokawa, T., Kawano, N. and Sasaki, S. (2008) Observation of the lunar topography by the laser altimeter LALT on board Japanese lunar explorer SELENE. Advances in Space Research, 42, 317–322.

Asmar, S.W., Konopliv, A.S., Watkins, M.M., Williams, J.G., Park, R.S., Kruizinga, G., Paik, M., Yuan, D.N., Fahnestock, E., Strekalov, D., Harvey, N., Lu, W., Kahan, D., Oudrhiri, K., Smith, D.E. and Zuber, M.T. (2013) The Scientific Measurement System of the Gravity Recovery and Interior Laboratory (GRAIL) Mission. In: GRAIL: Mapping the Moon's Interior, Zuber, M.T. and Russell, C.T. (eds) Springer, New York, pp. 25–55.

Baker, D.M.H., Head, J.W., Collins, G.S. and Potter, R.W.K. (2016) The formation of peak-ring basins: Working hypotheses and path forward in using observations to constrain models of impact-basin formation. Icarus, 273, 146–163.

Baker, D.M.H., Head, J.W., Fassett, C.I., Kadish, S.J., Smith, D.E., Zuber, M.T. and Neumann, G.A. (2011) The transition from complex crater to peak-ring basin on the Moon: New observations from the Lunar Orbiter Laser Altimeter (LOLA) instrument. Icarus, 214, 377–393.

Baldwin, R.B. (1964) Lunar crater counts. The Astronomical Journal, 69, 377-392.

Barton, P.J. (1986) The relationship between seismic velocity and density in the continental crust - a useful constraint? Geophysical Journal of the Royal Astronomical Society, 87, 195-208.

Besserer, J., Nimmo, F., Wieczorek, M.A., Weber, R.C., Kiefer, W.S., McGovern, P.J., Andrews-Hanna, J.C., Smith, D.E. and Zuber, M.T. (2014) GRAIL gravity constraints on the vertical and lateral den-sity structure of the lunar crust. Geophy-sical Research Letters, 41, 5771-5777.

Bierhaus, E.B., Chapman, C.R. and Merline, W.J. (2005) Secondary craters on Europa and implications for cratered surfaces. Nature, 437, 1125–1127.

Binder, A.B. (1998) Lunar Prospector: Overview. Science, 281, 1475–1476.

Birch, F. (1964) Density and composition of mantle and core. Journal of Geophysical Research, 69, 4377–4388.

Boehnke, P. and Harrison, T. M. (2016) Illusory Late Heavy Bombardments, Proceedings of the National Academy of Sciences of the United States of America, 113 (39), 10802-10806.

Bottke, W.F. and Norman, M.D. (2017) The Late Heavy Bombardment. Annu. Rev. Earth Planet Sci., 45, 619-647.

Bottke, W.F., Levison, H.F., Nesvorný, D., Dones, L. (2007) Can planetesimals left over from terrestrial planet formation produce the lunar Late Heavy Bombardment? Icarus, 190(1), 203-223.

Bottomley R.J., York D., Grieve R.A.F. (1990) ^{40}Argon-^{39}Argon dating of impact craters. Proc Lunar Planet Sci Conf 20, 421-431.

Bufton, J.L. (1989) Laser Altimetry Measurements from Aircraft and Spacecraft. Proceedings of the IEEE, 77, 463-477.

Chapin, D.A. (1996) A deterministic approach toward isostatic gravity residuals – A case study from South America, Geophysics, 61 (4), 1022-1033.

Chin, G., Brylow, S., Foote, M., Garvin, J., Kasper, J., Keller, J., Litvak, M., Mitro-fanov, I., Paige, D., Raney, K., Robinson, M., Sanin, A., Smith, D., Spence, H., Spudis, P., Stern, S.A., Zuber, M.T. (2007) Lunar reconnaissance orbiter overview: The instrument suite and mission. Space Science Reviews, 129, 391–419.

Christensen, E.J., Born, G.H., Hildebrand, C.E. and Williams, B.G. (1977) The Mass of Phobos from Viking Flybys, Geophysical Research aLetters, 4 (12), 555-557.

Cintala, M.J. and Grieve, R.A.F. (1998) Scaling impact melting and crater dimensions: Impli-cations for the lunar cratering record. Meteoritics and Planetary Science, 33, 889–912.

Collins, G.S. (2014) Numerical simulations of impact crater formation with dilatancy. Journal of Geophysical Research: Planets, 119, 2600–2619.

Collins, G.S., Wünnemann, K., Artemieva, N. and Pierazzo, E. (2012) Numerical Modelling of Impact Processes. Impact Cratering: Processes and Products, 254-270.

Earth Impact Database (2011) URL: www.unb.ca/passc/ImpactDatabase accessed: May 15, 2019.

Elkins Tanton, L.T., Van Orman, J.A., Hager, B.H. and Grove, T.L. (2002) Re-examination of the lunar magma ocean cumulate overturn hypo-thesis: Melting or mixing is required. Earth and Planetary Science Letters, 196, 239–249.

Emeljanov, N.V. and Kanter, A.A. (1989) A method to compute inclination functions and their derivatives. Manuscripta Geodaetica, 14, 77-83.

von Engelhardt, W., Arndt, J., Mueller, W.F. and Stöffler, D. (1970) Shock metamorphism of lunar rocks and origin of the regolith at the Apollo 11 landing site. Apollo 11 Lunar Science Conference, Proc., Vol. 1., 363–384.

Fassett, C.I., Head, J.W., Kadish, S.J., Mazarico, E., Neumann, G.A., Smith, D.E. and Zuber, M.T. (2012) Lunar impact basins: Stratigraphy, sequence and ages from superposed impact crater populations measured from Lunar Orbiter Laser Altimeter (LOLA) data. Journal of Geophysical Research: Planets, 117, 1–13.

Freed, A.M., Johnson, B.C., Blair, D.M., Melosh, H.J., Neumann, G.A., Phillips, R.J., Solomon, S.C., Wieczorek, M.A. and Zuber, M.T. (2014) The formation of lunar mascon basins from impact to contemporary form. Journal of Geophysical Research: Planets, 119, 1-20.

French, B.M. (1998) Traces of Catastrophe: A Handbook of Shock-Metamorphic Features in Terrestrial Meteorite Impact Structures. Lunar and Planetary Institute, Houston, pp. 120.

Garvin, J.B., Robinson, M.S., Frawley, J. Tran, T., Mazarico, E., Neumann, G.A. (2011) Linne: Simple Lunar Mare Crater Geometry from LRO Observations. 42nd Lunar Planet Sci Conf, Abstract #2063.

Gault, D.E., Oberbeck, V.R. and Quaide, W.L. (1968) Impact cratering mechanics and structures. In: Shock metamorphism of natural materials, French M., Short, N.M. (eds), Mono Book Corp., Baltimore, 87-99.

Gomes, R., Levison, H.F., Tsiganis, K., Morbidelli, A. (2005) Origin of the cataclysmic Late Heavy Bombardment period of the terrestrial planets, Nature, 435, 466-469.

Goossens, S., Lemoine, F.G., Sabaka T.J., Nicholas, J.B., Mazarico, E., Rowlands, Loomis, B.D., Chinn, D.S., Neumann, G.A., Smith, D.E. and Zuber, M.T. (2016) 27th Lunar Planet Sci. Conference, Abstract #1484.

Goossens, S.J., Sabaka, T.J., Wieczorek, M.A., Neumann, G.A., Mazarico, E., Lemoine, F.G., Nicholas, J.B., Smith, D.E. and Zuber, M.T. (2020). High-resolution gravity field models from GRAIL data and implications for models of the density structure of the Moon's crust. Journal of Geophysical Research: Planets, 125, 1-31.

Haase, I., Wählisch, M., Gläser, P., Oberst, J. and Robinson, M.S. (2019) Coordinates and Maps of the Apollo 17 Landing Site. Earth and Space Science, 6, 59–95.

Hartmann, W.K. (2019) History of the terminal cataclysm paradigm: Epistemology of a planetary bombardment that never (?) happened, Geosciences (Switzerland), 9 (7), 1-77.

Hartmann, W.K. and Davis, D.R. (1975) Satellite-Sized Planetesimals and Lunar Origin. Icarus, 24, 504-515.

Hartmann, W.K., Strom, R.G., Weidenschilling, S.J., Blasius, K.R., Woronow, A., Dence, M.R., Grieve, R.A.F., Diaz, J., Chapman, C.H., Shoemaker, E.M. and Jones, K.W. (1981) Chronology of Planetary Volcanism by Comparative Studies of Planetary Craters, Basaltic Volcanism on the Terrestrial Planets, Pergamon Press, Elmsford, NY, 1050-1127.

Hartmann, W.K. and Wood, C.A. (1971) Moon: Origin and evolution of multi-ring basins. The Moon, 3, 3-78.

Hartung, J.B., Dence, M.R., Adams, J.A.S. (1971) Potassium-argon dating of shock-metamorphosed rocks from the Brent Impact Crater, Ontario, Canada, Journal of Geophysical Research, 76, 5437-5448.

Head, J.W., Fassett, C.I., Kadish, S.J., Smith, D.E., Zuber, M.T., Neumann, G.A. and Mazarico, E. (2010) Global distribution of large lunar craters: Implications for resurfacing and impactor populations. Science, 329, 1504-1507.

Heffels, A., Knapmeyer, M., Oberst, J. and Haase, I. (2017) Re-evaluation of Apollo 17 Lunar Seismic Profiling Experiment data. Planetary and Space Science, 135, 43–54.

Heiken, G.H., Vaniman, D.T. and French, B.M. (1991) Lunar Sourcebook - A User's Guide to the Moon. Cambridge University Press, pp. 736.

Henkel, H. and Reimold, W.U. (1996) Integrated gravity and magnetic modelling of the Vredefort impact structure - Reinterpretation of the Wit-watersrand Basin as the erosional remnant of an impact basin. Econ. Geol. Res. Unit., 1–89.

Hess, P.C. and Parmentier, E.M. (1995) A model for the thermal and chemical evolution of the Moon's interior: implications for the onset of mare volcanism. Earth and Planetary Science Letters, 134, 501-514.

Hiesinger, H., Head, J.W., Wolf, U., Jaumann, R. and Neukum, G. (2011) Ages and stratigraphy of lunar mare basalts: a synthesis. Spec. Pap., Geol. Soc. Am. 477, 1–51.

Hiesinger, H., Jaumann, R., Neukum, G. and Head, J.W. (2000) Ages of mare basalts on the lunar nearside. Journal of Geophysical Research: Planets, 105, 29239–29275.

Hildebrand, C.E., Born, G.H. and Duxbury, T.C. (1979) The Deimos Mass Experiment: Planning and Preliminary Results, In: Natural and Artifical Satellite Motions, Nacozy and Ferraz-Mello (eds.), University of Texas Press, Austin, pp 353-368.

Hirt, C. and Featherstone, W.E. (2012) A 1.5km-resolution gravity field model of the Moon. Earth and Planetary Science Letters, 329–330, 22–30.

Howard. (1970) Mascons, mare rock and isostasy. Nature, 226, 924-925.

Huang, Q. and Wieczorek, M.A. (2012) Density and porosity of the lunar crust from gravity and topography. Journal of Geophysical Research: Planets, 117, 1–9.

Ivanov, B.A. (2005) Numerical Modeling of the Largest Terrestrial Meteorite Craters, Solar System Research, 39, 381-409.

Kamalakar, J.A., Bhaskar, K.V.S., Laxmi Prasad, A.S., Ranjith, R., Lohar, K.A., Venketeswaran, R. and Alex, T.K. (2005) Lunar ranging instrument for Chandrayaan-1. Journal of Earth System Science, 114, 725-731.

Kamata, S., Sugita, S., Abe, Y., Ishihara, Y., Harada, Y., Morota, T., Namiki, N., Iwata, T., Hanada, H., Araki, H., Matsumoto, K., Tajika, E., Kuramoto, K. and Nimmo, F. (2015) The relative timing of Lunar Magma Ocean solidification and the Late Heavy Bombardment inferred ferred from highly degraded impact basin structures. Icarus, 250, 492-503.

Kaula, W.M. (1966) Tests and combination of satellite determinations of the gravity field with gravimetry. Journal of Geophysical Research, 71, 5303–5314.

Kaula, W.M., Schubert, G., Lingenfelter, R.E., Sjorgen, W.L. and Wollenhaupt, W.R. (1973) Lunar topography from Apollo 15 and 16 laser altimetry. Proceedings of the 4th Lunar Science Conference, 3, 2811-2819.

Kenkmann, T., Collins, G.S. and Wünnemann, K. (2013) The modification stage of crater formation. Impact cratering: processes and products, G.R. Osinski, E. Pierazzo (eds), Blackwell Publishing Ltd, 60-75.

Khan, A., Mosegaard, K. and Rasmussen, K.L. (2000) A new seismic velocity model for the moon from a Monte Carlo inversion of the Apollo lunar seismic data. Geophysical Research Letters, 27, 1591-1594.

Kiefer, W.S., MacKe, R.J., Britt, D.T., Irving, A.J. and Consolmagno, G.J. (2012) The density and porosity of lunar rocks. Geophysical Research Letters, 39, 1-5.

Klipstein, W.M., Arnold, B.W., Enzer, D.G., Ruiz, A.A., Tien, J.Y., Wang, R.T. and Dunn, C.E. (2014) The lunar gravity ranging system for the gravity recovery and interior laboratory (GRAIL) mission. GRAIL: Mapping the Moon's Interior (eds M.T. Zuber, C.T. Russell), Springer, New York, 57–76.

Kneissl, T., Michael, G.G., Platz, T. and Walter, S.H.G. (2015) Age determination of linear surface features using the Buffered Crater Counting approach - Case studies of the Sirenum and Fortuna Fossae graben systems on Mars. Icarus, 250, 384–394.

Koeberl, C. (1994) African meteorite impact craters: Characteristics and geological importance. Journal of African Earth Sciences, 18, 263–295.

Konopliv, A.S., Binder, A.B., Hood, L.L., Kucinskas, A.B., Sjogren, W.L. and Williams, J.G. (1998) Improved gravity field of the moon from lunar prospector, Science, 281, 1476–1480.

Konopliv, A.S., Park, R.S., Yuan, D.N., Asmar, S.W., Watkins, M.M., Williams, J.G., Fahnestock, E., Kruizinga, G., Paik, M., Strekalov, D., Harvey, N., Smith, D.E. and Zuber, M.T. (2013) The JPL lunar gravity field to spherical harmonic degree 660 from the GRAIL Primary Mission, Journal of Geophysical Research: Planets, 118 (7), 1415-1534.

Konopliv, A.S., Park, R.S., Yuan, D.-N., Asmar, S.W., Watkins, M.M., Williams, J.G., Fahnestock, E., Kruizinga, G., Paik, M., Strekalov, D., Harvey, N., Smith, D.E. and Zuber, M.T. (2014) High-resolution lunar gravity fields from the GRAIL Primary and Extended Missions. Geophysical Research Letters, 41, 1452-1458.

Kovach, R.L., Watkins, J.S. and Talwani, P. (1973) Lunar Seismic Profiling Experiment, In: Apollo 17: Preliminary Science Report NASA SP-330, Section 10, U.S. Govt. Print. Off., pp. 1-12.

Kreslavsky, M.A., Head, J.W., Neumann, G.A., Rosenburg, M.A., Aharonson, O., Smith, D.E. and Zuber, M.T. (2013) Lunar topographic roughness maps from Lunar Orbiter Laser Altimeter (LOLA) data: Scale dependence and correlation with geologic features and units. Icarus, 226, 52-66.

Kring, D.A., Cohen, B.A. (2002) Cataclysmic bombardment throughout the inner Solar System 3.9–4.0 Ga. Journal of Geophysical Research, 107, 1-6.

Krüger, T., Hergarten, S. and Kenkmann, T. (2018) Deriving Morphometric Parameters and the Simple-to-Complex Transition Diameter From a High-Resolution, Global Database of Fresh Lunar Impact Craters (D ≥ ~3 km). Journal of Geophysical Research: Planets, 123, 2667–2690.

Latham, G., Ewing, M., Dorman, J., Lammlein, D., Press, F., Toksőz, N., Sutton, G., Duennebier, F. and Nakamura, Y. (1972) Moonquakes and lunar tectonism. The Moon, 4, 373–382.

Lawrence, D.J., Feldman, W.C., Barraclough, B.L., Binder, A.B., Elphic, R.C., Maurice, S. and Thomsen, T.R. (1998) Global elemental maps of the moon: The Lunar Prospector gamma-ray spectrometer. Science, 281, 1484–1489.

Lemoine, F.G., Goossens, S., Sabaka, T.J., Nicholas, J.B., Mazarico, E., Rowlands, D.D., Loomis, B.D., Chinn, D.S., Neumann, G.A., Smith, D.E. and Zuber, M.T. (2014) GRGM900C: A degree 900 lunar gravity model from GRAIL primary and extended mission data. Geophysical Research Letters, 41, 3382-3389.

Lemoine, F.G., Goossens, S., Sabaka, T.J., Nicholas, J.B., Mazarico, E., Rowlands, D.D., Loomis, B.D., Chinn, D.S., Caprette, D.S., Neumann, G.A., Smith, D.E., Zuber, M.T. (2013) High-degree gravity models from GRAIL primary mission data. Journal of Geophysical Research: Planets, 118, 1676–1698.

Lemoine, F.G., Smith, D.E., Zuber, M.T., Neumann, G.A. and Rowlands, D.D. (1997) A 70th degree lunar gravity model (GLGM-2) from Clementine and other tracking data. Journal of Geophysical Research: Planets, 102, 16339–16359.

Liu, T., Michael, G., Engelmann, J., Wünnemann, K. and Oberst, J. (2019) Regolith mixing by impacts: Lateral diffusion of basin melt. Icarus, 321, 691-704.

Lucey, P., Korotev, R.L., Gillis, J.J., Taylor, L.A., Lawrence, D., Campbell, B.A., Elphic, R., Feldman, B., Hood, L.L., Hunten, D., Mendillo, M., Noble, S., Papike, J.J., Reedy, R.C., Lawson, S., Prettyman, T., Gasnault, O. and Maurice, S. (2006) Understanding the lunar surface and space-Moon interactions. Reviews in Mineralogy and Geochemistry, 166, 83-219.

Marchi, S., Bottke, W.F., Kring, D.A. and Morbidelli, A. (2012) The onset of the lunar cataclysm as recorded in its ancient crater populations. Earth and Planetary Science Letters, 325, 27-38.

Marchi, S., Bottke, W.F., Cohen, B.A., Wünnemann, K., Kring, D.A., McSween, H.Y., De Sanctis, M.C., O'Brien, D.P., Schenk, P., Raymond, C.A. and Russell, C.T. (2013) High-velocity collisions from the luar cataclysm recorded in asteroidal meteorites, Nature Geosciences, 6, 303-307.

Maurice, M., Tosi, N., Schwinger, S., Breuer, D. and Kleine, T. (2020) A long-lived magma ocean on a young Moon. Science Advances, 6(28), 1-10.

Mazarico, E., Lemoine, F.G., Han, S.C. and Smith, D.E. (2010) GLGM-3: A degree-150 lunar gravity model from the historical tracking data of NASA Moon orbiters. Journal of Geophysical Research: Planets, 115, 1–14.

McGill, G.E. (1977) Crater as "fossils": The remote dating of planetary surface materials, Geol. Soc. Am. Bull. 88, 1102-1110.

McGovern, P.J., Solomon, S.C., Smith, D.E., Zuber, M.T., Simons, M., Wieczorek, M.A., Phillips, R.J., Neumann, G.A., Aharonson, O. and Head, J.W. (2004) Correction to "Localized gravity/topography admittance and correlation spectra on Mars: Implications for regional and global evolution." Journal of Geophysical Research, 109, 1-5.

McKenzie, D. (1994) The relationship between gravity and topography on Earth and Venus, Icarus, 112, 55–88.

McKenzie, D. and Fairhead, D. (1997) Estimates of the effective elastic thickness of the continental lithosphere from Bouguer and free air gravity anomalies. Journal of Geophysical Research: Solid Earth, 102, 27523–27552.

Melosh, H.J. (1989) Impact cratering: A geologic process. Research supported by NASA. New York, Oxford University Press, pp. 253.

Melosh, H.J., Freed, A.M., Johnson, B.C., Blair, D.M., Solomon, S.C., Wieczorek, M.A. and Zuber, M.T. (2013) The Origin of Lunar Mascon Basins. Science, 340, 1552–1556.

Meyer, C. (2012) Sedimentological, Structural and Geochemical Investigations of the Suevite of the Impact Crater Nördlinger Ries, Germany. Doctoral Dissertation. pp. 384.

Michael, W.H. and Blackshear, W.T. (1972) Recent results on the mass, gravitational field and moments of inertia of the moon. The Moon, 3, 388–402.

Michael, G.G, Basilevsky, A. and Neukum, G. (2018) On the history of the early meteoritic bombardment of the Moon: Was there a terminal lunar cataclysm? Icarus, 302, 80-103.

Michael, G.G. and Neukum, G. (2010) Planetary surface dating from crater size-frequency distribution measurements: Partial resurfacing events and statistical age uncertainty. Earth and Planetary Science Letters, 294, 223–229.

Michikami, T., Moriguchi, K., Hasegawa, S. and Fujiwara, A. (2007) Ejecta velocity distribution for impact cratering experiments on porous and low strength targets. Planetary and Space Science, 55, 70–88.

Miljković, K., Collins, G.S., Wieczorek, M.A., Johnson, B.C., Soderblom, J.M., Neumann, G.A. and Zuber, M.T. (2016) Subsurface morphology and scaling of lunar impact basins. Journal of Geophysical Research: Planets, 121, 1695–1712.

Morbidelli, A., Petit, J.M., Gladman, B., Chambers, J. (2001) A plausible cause of the late heavy bombardment, Meteoritics and Planetary Science, 36 (3), 371-380.

Morbidelli, A., Nesvorny, D., Laurenz, V., Marchi, S., Rubie, D.C., Elkins-Tanton, L., Wieczorek, M.A. and Jacobson, S. (2018) The Timeline of the Lunar Bombardment - Revisited. Icarus, 305, 262-276.

Muller, P.M. and Sjogren, W.L. (1968) Mascons: Lunar mass concentrations. Science, 161, 680–684.

Nakamura, Y., Latham, G.V. and Dorman, H.J. (1982) Apollo lunar seismic experiment - final summary. Journal of Geophysical Research, 87, 117-123.

Nakamura, Y., Latham, G. V., Dorman, H.J. and Duennebier, F.K. (1976) Seismic structure of the moon - A summary of current status. 7th Lunar Science Conference, Houston, Texas, 3, 3113-3121.

Namiki, N., Iwata, T., Matsumoto, K., Hanada, H., Noda, H., Goossens, S., Ogawa, M., Kawano, N., Asari, K., Tsuruta, S., Ishihara, Y., Liu, Q., Kikuchi, F. and Ishikawa, T. (2009) Farside Gravity Field of the Moon. Space Technology, 323, 900–905.

Nelson, D.M., Koeber, S.D., Daud, K., Robinson, M.S., Watters, T., Banks, M. and Williams, N.R., 2014. Mapping Lunar Maria Extents and Lobate Scarps Using LROC Image Products. Lunar and Planetary Science Conference, Abstract #2861.

Neukum, G. (1983) Meteoriten-bombardement und Datierung Planetarer Oberflächen. University of Munich, Germany. Habilitation Dissertation. pp. 186.

Neukum, G., Ivanov, B.A. and Hartmann, K.W. (2001) Cratering records in the inner solar system in relation to the lunar reference system. Chronology and Evolution of Mars, 96, 55–86.

Neukum, G., Koenig, B. and Arkani-Hamed, J. (1975) A study of lunar impact crater size-distributions, Moon, 12, 201-229.

Neumann, G.A., Zuber, M.T., Smith, E. and Lemoine, F.G. (1996) The lunar crust : Global structure and signature of major basins. Journal of Geophysical Research, 101, 16841-16843.

Neumann, G.A., Zuber, M.T., Wieczorek, M.A., Head, J.W., Baker, D.M.H., Solo-mon, S.C., Smith, D.E., Lemoine, F.G., Mazarico, E., Sabaka, T.J., Goossens, S.J., Melosh, H.J., Phillips, R.J., Asmar, S.W., Konopliv, A.S., Williams, J. G., Sori, M.M., Soderblom, J.M., Miljković, K., Andrews-Hanna, J.C., Nimmo, F. and Kiefer, W.S. (2015) Lunar impact basins revealed by Gravity Recovery and Interior Laboratory measurements. Science Advances, 1(9), e1500852–e1500852.

Neumann, G.A., Zuber, M.T., Wieczorek, M.A., McGovern, P.J., Lemoine, F.G. and Smith, D.E. (2004) Crustal structure of Mars from gravity and topography. Journal of Geophysical Research: Planets, 109, 1–18.

Nimmo, F. (2002) Admittance estimates of mean crustal thickness and density at the Martian hemispheric dichotomy. Journal of Geophysical Research: Planets, 107, 1-6.

Norman, M.D. and Nemchin, A.A. (2014) A 4.2 billion year old impact basin on the Moon: U-Pb dating of zirconolite and apatite in lunar melt rock 67955. Earth and Planetary Science Letters, 388, 387-398.

Norman, M.D., Taylor, L.A. (2005) Testing the lunar cataclysm: Identification of lunar impact melts possibly older than Nectaris. Lunar Planetary Science Conference 36, Abstract #1570.

Nozette, S., Rustan, P., Pleasance, L.P., Horan, D.M., Regeon, P., Shoemaker, E.M., Spudis, P.D., Acton, C.H., Baker, D.N., Blamont, J.E., Buratti, B.J., Corson, M.P., Davies, M.E., Duxbury, T.C., Eliason, E.M., Jakosky, B.M., Kordas, J.F., Lewis, I.T., Lichtenberg, C.L., Lucey, P.G., Malaret, E., Massie, M.A., Resnick, J.H., Rollins, C.J., Park, H.S., McEwen, A.S., Priest, R.E., Pieters, C.M., Reisse, R.A., Robinson, M.S., Simpson, R.A., Smith, D.E., Sorenson, T.C., Vorder Breugge, R.W. and Zuber, M.T. (1994) The Clementine mission to the Moon: Scientific overview. Science, 266, 1835-1839.

Orgel, C., Michael, G., Fassett, C.I., van der Bogert, C.H., Riedel, C., Kneissl, T. and Hiesinger, H. (2018) Ancient Bombardment of the Inner Solar System: Reinvestigation of the "Fingerprints" of Different Impactor Populations on the Lunar Surface. Journal of Geophysical Research: Planets, 123, 748–762.

Van Orman, J.A. and Grove, T.L. (2000) Origin of lunar high-titanium ultramafic glasses: Constraints from phase relations and dissolution kinetics of clinopyroxene-ilmenite cumulates. Meteoritics and Planetary Science, 35, 783–794.

Osinski, G.R. and Pierazzo, E. (2013) Impact cratering: processes and products. In: Osinski, G.R. , Pierazzo, E. (eds) Impact cratering: processes and products, Blackwell Publishing Ltd, 1-20.

Papanastassiou, D.A. and Wasserburg, G.J. (1971) Lunar chronology and evolution from RbSr studies of Apollo 11 and 12 samples. Earth and Planetary Science Letters, 11, 37–62.

Park, R.S., Konopliv, A.S., Yuan, D.-N., Asmar, S., Watkins, M.M., Williams, J., Smith, D.E. and Zuber, M.T. (2015) A high resolution spherical harmonic degree 1500 lunar gravity field from th GRAIL mission. AGU Fall Meeting, Abstract #G41B01.

Pei, Z., Wang, Q. and Tian, Y. (2015) Technology roadmap for Chang'e program. J. Deep. Space Explor. 2, 99-110.

Phillips, R.J., Saunders, R.S. and Conel, J.E. (1973) Mars: Crustal structure inferred from Bouguer gravity anomalies. Journal of Geophysical Research, 78, 4815–4820.

Pierazzo, E. and Collins, G. (2004) A Brief Introduction to Hydrocode Modeling of Impact Cratering, In: Dypvik H., Burchell M.J., Claeys P. (eds) Cratering in Marine Environments and on Ice. Impact Studies. Springer, Berlin, Heidelberg, 323-340.

Pieters, C.M., Head, J.W., Gaddis, L., Jolliff, B. and Duke, M. (2001) Rock types of South Pole-Aitken basin and extent of basaltic volcanism. Journal of Geophysical Research: Planets, 106, 28001–28022.

Pieters, C.M., Boardman, J., Buratti, B., Chatterjee, A., Clark, R., Glavich, T., Green, R., Head, J., Isaacson, P., Malaret, E., McCord, T., Mustard, J., Petro, N., Runyon, C., Staid, M., Sunshine, J., Taylor, L., Tompkins, S., Varanasi, P. and White, M. (2009) The Moon mineralogy mapper (M3) on Chandrayaan-1. Current Science, 96, 500–505.

Pilkington, M. and Grieve, R.A.F. (1992) The Geophysical Siganture of Terrestrial Impact Craters (1992). Reviews of Geophysics, 30, 161–181.

Raab, H. (2009) Shatter cone. URL: www.landesstelle.de/shatter-cone, accessed Septembre 27, 2019.

Raymond, S.N. and Morbidelli, A. (2014) The Grand Tack model: a critical review. Proceedings of the International Astro-nomical Union, 9(S310), 194A203.

Reimold, W.U. and Gibson, R.L. (2009) Meteorite Impact, 3rd edition. Springer, Berlin Heidelberg, pp. 337.

Riedel, C., Michael, G., Kneissl, T., Orgel, C., Hiesinger, H. and van der Bogert, C.H. (2018) A New Tool to Account for Crater Obliteration Effects in Crater Size-Frequency Distribution Measurements. Earth and Space Science, 5, 258–267.

Ringwood, A.E. and Kesson, S.E. (1976) A dynamic model for mare basalt petrogenesis. 7th Lunar Science Conference, Houston, Texas, 2, 1697-1722.

Robinson, M.S., Brylow, S.M., Tschimmel, M., Humm, D., Lawrence, S.J., Thomas, P.C., Denevi, B.W., Bowman-Cisneros, E., Zerr, J., Ravine, M.A., Caplinger, M.A., Ghaemi, F.T., Schaffner, J.A., Malin, M.C., Mahanti, P., Bartels, A., Anderson, J., Tran, T.N., Eliason, E.M., McEwen, A.S., Turtle, E., Jolliff, B.L. and Hiesinger, H. (2010) Lunar reconnaissance orbiter camera (LROC) instrument overview. Space Science Reviews, 150, 81-124.

Roth, C.H. (1997) Bulk density of surface crusts: Depth functions and relationships to texture. Catena, 29, 223–237.

Ryder, G., Koeberl, C. and Mojzsis, S.J. (2000) Heavy bombardment on the Earth at 3.85 Ga: The search for petrographic and geochemical evidence. In: Canup, R.M., Righter, K. (eds), Origin of the Earth and Moon. Univ. of Arizona Press, Tucson, pp. 475-492.

Ryder, G. and Wood, J.A. (1965) Serenitatis and Imbrium impact melts - Implications for large-scale layering in the lunar crust. 8th Lunar Science Conference, Houston, Texas, 1, 655–668.

Satya Kumar, A.V., Rajasekhar, R. P. and Tiwari, V. M. (2017) Gravity anomalies and crustal structure of the Lunar far side highlands, Planetary and Space Science, 163, 106-113.

Scholten, F., Oberst, J., Matz, K.D., Roatsch, T., Wählisch, M., Speyerer, E.J. and Robinson, M.S. (2012) GLD100: The near-global lunar 100 m raster DTM from LROC WAC stereo image data. Journal of Geophysical Research: Planets, 117, 1–12.

Schumacher, S. and Breuer, D. (2006) Influence of a variable thermal conductivity on the thermochemical evolution of Mars. Journal of Geophysical Research: Planets, 111, 1–19.

Shearer, C.K., Hess, P.C., Wieczorek, M.A., Pritchard, M.E., Parmentier, E.M., Borg, L.E., Longhi, J., Elkins-Tanton, L.T., Neal, C.R., Antonenko, I., Canup, R.M., Halliday, A.N., Grove, T.L., Hager, B.H., Lee, D.C. and Wiechert, U. (2006) Thermal and magmatic evolution of the Moon. Reviews in Mineralogy and Geochemistry, 60, 365-518.

Shirley, K.A., Zanetti, M., Jolliff, B., van der Bogert, C.H. and Hiesinger, H. (2016) Crater size-frequency distribution measurements and age of the Compton-Belkovich Volcanic Complex. Icarus, 273, 214-223.

Shoemaker, E., Hackman, R. Eggleton, R. (1963) Interplanetary Corre-lation of Geologic Time. Advances in the Astronautical Sciences, 8, 70-89.

Shoemaker, E.M. (1962) Interpretation of lunar craters. In: Koual Z. (ed), Physics and Astronomv of the Moon. Academic Press, New York, pp. 283-359.

Shoemaker, E.M. and Hackmann, R.J. (1962) Stratigraphic basis for a lunar time scale. The Moon, 14, 289–300.

Smith, D.E., Zuber, M.T., Jackson, G.B., Cavanaugh, J.F., Neumann, G.A., Riris, H., Sun, X., Zellar, R.S., Coltharp, C., Connelly, J., Katz, R.B., Kleyner, I., Liiva, P., Matuszeski, A., Mazarico, E.M., McGarry, J.F., Novo-Gradac, A.M., Ott, Melanie N., Peters, C., Ramos-Izquierdo, L.A., Ramsey, L., Rowlands, D.D., Schmidt, S., Scott, V.S., Shaw, G.B., Smith, J.C., Swinski, J.P., Torrence, M.H., Unger, G., Yu, A.W. and Zagwodzki, T.W. (2010) The lunar orbiter laser altimeter investigation on the lunar reconnaissance orbiter mission. Space Science Reviews, 150, 209–241.

Smith, D.E., Zuber, M.T., Neumann, G.A. and Lemoine, F.G. (1997) Topography of the Moon from the Clementine lidar. Journal of Geophysical Research: Planets, 102, 1591–1611.

Smith, D.E., Zuber, M.T., Neumann, G.A., Mazarico, E., Lemoine, F.G., Head, J.W., Lucey, P.G., Aharonson, O., Robinson, M.S., Sun, X., Torrence, M.H., Barker, M.K., Oberst, J., Duxbury, T.C., Mao, D., Barnouin, O.S., Jha, K., Rowlands, D.D., Goossens, S., Baker, D., Bauer, S., Gläser, P., Lemelin, M., Rosenburg, M., Sori, M.M., Whitten, J. and Mcclanahan, T. (2017) Summary of the results from the lunar orbiter laser altimeter after seven years in lunar orbit. Icarus, 283, 70–91.

Snyder, G.A., Taylor, L.A. and Neal, C.R. (1992) A chemical model for generating the sources of mare basalts: Combined equilibrium and fractional crystallization of the lunar magmasphere. Geochimica et Cosmochimica Acta, 56, 3809–3823.

Soderblom, J.M., Evans, A.J., Johnson, B.C., Melosh, H.J., Miljkovi, K., Phillips, R.J., Andrews-Hanna, J.C., Bierson, C.J., Head, J.W., Milbury, C., Neumann, G.A., Nimmo, F., Smith, D.E., Solomon, S.C. and Sori, M.M. (2015) The fractured Moon: Production and saturation of porosity in the lunar highlands from impact cratering, 6939-6944.

Solomon, S.C. (1974) Density within the Moon and implications for lunar composition. The Moon, 9, 147–166.

Spudis, P.D., Reisse, R.A. and Gillis, J.J. (1994) Ancient multiring basins on the moon revealed by Clementine laser altimetry. Science, 266, 1848–1851.

Stöffler, D. and Ryder, G. (2001) Stratigraphy and isotope ages of lunar geologic units: Chronological standard for the inner solar system. Space Science Reviews, 96, 9–54.

Stuart, J.S. and Binzel, R.P. (2004) Bias-corrected population, size distribution, and impact hazard for the near-Earth objects. Icarus, 170, 295–311.

Sun, H.X. and Dai, S.W. (2005) Mission objectives and payloads for the first lunar exploration of China. International Astronautical Federation, 55th International Astronautical Congress 2004, 9, 6085–6090.

Tagle, R. and Hecht, L. (2006) Geochemical identification of projectiles in impact rocks. Meteoritics and Planetary Science, 41, 1721–1735.

Tapley, B.D. and Reigber, C. (1999) GRACE: A satellite-to-satellite tracking geopotential mapping mission. Bollettino di Geofisica Teorica ed Applicata, 40 (3-4), 291.

Taylor, S.R. (1989) Growth of planetary crusts. Tectonophysics, 161, 147–156.

Taylor, J.G., Warren, P., Ryder, G., Delano, J., Pieters, C. and Lofgren, G. (1991) Lunar rocks. In: Lunar Sourcebook G.H. Heiken, D.T. Vaniman, B.M. French (eds), Cambridge University Press, Cambridge, 183–284.

Tera, F., Papanastassiou, D.A. and Wasserburg, G.J. (1974) Isotopic evidence for a terminal lunar cataclysm. Earth and Planetary Science Letters, 22, 1–21.

Toksöz, M.N., Press, F., Dainty, A, Anderson, K., Latham, G., Ewing, M., Dorman, J., Lammlein, D., Sutton, G. and Duenne-bier, F. (1972) Structure, compo-sition, and properties of lunar crust. Proceedings of the Lunar Science Conf., 3, 2527-2544.

Tompkins, S. and Pieters, C.M. (1999) Mineralogy of the lunar crust: Results from Clementine. Meteoritics and Planetary Science, 34, 25–41.

Trail D., Mojzsis S.J., Harrison T.M. (2007) Thermal events documented in Hadean zircons by ion microprobe depth profiles, Geochim. Cosmochim. Acta, 71(16), 4044-4065.

Turcotte, D.L. and Schubert, G. (2014) Geodynamics, 3rd edition. Cambridge University Press, New York, pp. 626.

Turcotte, D.L. (1997) Fractals and Chaos ind Geology and Geophysics, 2nd edition. Cambridge University Press, New York, pp. 398.

Vostreys, R., 1980. Data User's Note: Apollo seismological investigations. NASA STI/ Recon (Technical Report N, 81, 17970).

Wahl, D. and Oberst, J. (2017) Does the gravity signature of lunar basins correlate with their ages? EPSC Abstracts Vol. 11, Abstract #EPSC2017-323-1.

Walsh, K.J., Morbidelli, A., Raymond, S.N., O'Brien, D.P. and Mandell, A.M. (2011) A low mass for Mars from Jupiter's early gas-driven migration, Nature, 475, 206-209.

Warren, P.H. (1985) The Magma Ocean concept and lunar evolution. Annual Reviews of Earth and Planetary Sciences, 13, 201–240.

Warren, P.H. and Wasson, J.T. (1977) Pristine nonmare rocks and the nature of the lunar crust. 8th Lunar Science Conference, Houston, Texas, 2, 2215–2235.

Wieczorek, M.A. and Le Feuvre, M. (2009) Did a large impact reorient the Moon? Icarus, 200, 358–366.

Wieczorek, M.A., Jolliff, B.L., Khan, A., Pritchard, M.E., Weiss, B.P., Williams, J.G., Hood, L.L., Righter, K., Neal, C.R., Shearer, C.K., McCallum, I.S., Tompkins, S., Hawke, B.R., Peterson, C., Gillis, J.J. and Bussey, B. (2006) The constitution and structure of the Lunar interior. Reviews in Mineralogy and Geochemistry, 60, 221-364.

Wieczorek, M.A., Neumann, G.A., Nimmo, F., Kiefer, W.S., Taylor, J.G., Melosh, H.J., Phillips, R.J., Solomon, S.C., Andrews-Hanna, J.C., Asmar, S.W., Konopliv, A.S., Lemoine, F.G., Smith, D.E., Watkins, M.M., Williams, J.G. and Zuber, M.T. (2013) The Crust of the Moon as Seen by GRAIL. Science, 339, 671–675.

Wieczorek, M.A. and Phillips, R.J. (1998) Potential anomalies on a sphere' Applications to the thickness of the lunar crust. Journal of Geophysical Research, 103, 1715–1724.

Wieland, F., Reimold, W.U. and Gibson, R.L. (2006) New observations on shatter cones in the Vredefort impact structure, South Africa, and evaluation of current hypotheses for shatter cone formation. Meteoritics and Planetary Science, 41, 1737–1759.

Wilhelms, D.E. (1987) The Geologic History of the Moon. Professional Paper. USGS Numbered Series 1348, pp. 302.

Wood, J.A. (1972) Thermal history and early magmatism in the Moon. Icarus, 16, 229-240.

Wood, J.A., Dickey, J.S., Marvin, U.B. and Powell, B.N. (1970) Lunar anorthosites and a geophysical model of the moon. Proceedings of the Apollo 11 Lunar Science Conference, 1, 965-988.

Wünnemann, K., Collins, G.S. and Osinski, G.R. (2008) Numerical modelling of impact melt production in porous rocks. Earth and Planetary Science Letters, 269, 530-539.

Zhu, M., Wünnemann, K. and Potter, R. W. K., (2015) Numerical modeling of the ejecta distribution and formation of the Orientale basin on the Moon. Journal of Geophysical Research: Planets, 120, 2118-2134.

Zhu, M., Wünnemann, K., Potter, R.W.K., Kleine, T. and Morbidelli, A. (2019) Are the Moon's nearside-farside asymmetries the result of a giant impact? Journal of Geophysical Research: Planets, 124, 1-24.

Zuber, M.T., Smith, D.E., Lehman, D.H., Hoffman, T.L., Asmar, S.W. and Watkins, M.M. (2013a) Gravity recovery and interior laboratory (GRAIL): Mapping the lunar interior from crust to core. Space Science Reviews, 178, 3–24.

Zuber, M.T., Smith, D.E., Watkins, M.M., Asmar, S.W., Konopliv, A.S., Lemoine, F.G., Melosh, H.J., Neumann, G.A., Phillips, R.J., Solomon, S.C., Wieczorek, M.A., Williams, J.G., Goossens, S.J., Kruizinga, G., Mazarico, E., Park, R.S. and Yuan, D.-N. (2013b) Gravity Field of the Moon from the Gravity Recovery and Interior Laboratory (GRAIL) Mission. Science, 339, 2011–2014.

Zuber, M.T., Smith, D.E., Lemoine, F.G. and Neumann, G.A. (1994) The shape and internal structure of the Moon from the Clementine mission. Science, 266, 1839-1843.

Zuber, M.T., Smith, D.E., Phillips, R.J., Solomon, S.C., Neumann, G.A., II Hauk, S.A., Peale, S.J., Barnouin, O.S., Head, J.W., Johnson, C.L., Lemoine, F.G., Mazarico, E., Sun, X., Torrence, M.H., Freed, A.M., Klimczak, C., Margot, J., Oberst, J., Perry, M.E., McNutt, R.L., Balcerskt, J.A., Michel, N., Talpe, M.J. and Yang, D. (2012) Topography of the Northern Hemisphere of Mercury from MESSENGER Laser Altimetry Maria. Science, 336, 217-221.

3. Research paper I

Published in ISPRS Annals of Photogrammetry, Remote Sensing and Spatial Information Science
doi: 10.5194/isprs-annals-IV-2-W5-527-2019
Open Access publication, Creative Common Attribution 4.0
- postprint version -

Lateral variations in bulk density and porosity of the upper lunar crust from high-resolution gravity and topography data: comparison of different analysis techniques

Daniel Wahl [1], Jürgen Oberst [1,2]

[1] Technische Universität Berlin, Chair of Planetary Geodesy, 10623 Berlin, Germany

[2] German Aerospace Center (DLR), Institute of Planetary Research, 12489 Berlin, Germany

Abstract

We map lateral variations in bulk density of the upper lunar highland crust using the most recent GRAIL gravity field solution of degree and order 1500 in combination with LOLA topography data, both truncated to an upper limit of degree and order 700. Our maps have a spatial resolution of 0.75°, where each grid point was calculated using circular analysis regions of 3° radius. We apply two methods, which yield similar results for most parts of the study area. The first method minimizes the correlation between topography and Bouguer anomalies, the second maximizes the smoothness of the Bouguer anomalies. Both approaches suffer in the case that terrain is flat and lacks topographic features; consequently, this is where results from the two methods differ. We also mapped porosity of the crust using grain densities derived from Lunar Prospector spectrometry and sample analysis. It appears that variations in bulk density are mostly related to differences in crustal porosity. We find that high porosity is often associated with areas of impact basins. This confirms earlier studies that impacts changed the geophysical characteristics of the lithosphere sustainably and that the high porosity of the upper lunar crust is most likely impact induced.

3.1 Introduction

While the interior of the Moon is comparably homogeneous on global scale, the near-surface crustal structure is complex. In-situ seismic data as well as gravity measurements reveal that compaction of the crustal rocks increases quickly with depth. Also, there is evidence for significant regional variety in upper crust composition and physical properties.

The lunar near-surface structure is of great interest, as it reveals details of early crustal formation from the lunar magma ocean as well as subsequent evolution during the late heavy bombardment. The density may constrain the composition of the upper crust and availability of lunar resources. Besides, bulk density of the upper crust is needed to model mass distribution of the lower crust, independently from topographic features (calculation of Bouguer gravity).

In the past years, techniques have been demonstrated to obtain the density of the lunar crust using gravity data from Gravity Recovery and Interior Laboratory (GRAIL) mission (Zuber et al., 2013a) in combination with topography data. Besserer et al. (2014) performed a localized, multitaper spectral analysis on gravity and topography data, to study variations in the vertical density structure. While for the lunar highlands an average increase of density with depth of around 35 kg m^{-3} km^{-1} was found, mare regions reveal dense basaltic material to overly low-density anorthositic rock. Wieczorek et al. (2013) mapped the lateral variations in crustal density by analyzing the correlation between the gravity field and topography. A gravity field model of degree and order 420 was used to produce a crustal density map with a grid of 60 km spacing. Bulk density was found to vary between 2300 and 2900 kg m^{-3} globally. An average bulk density of the Moon's highland crust of 2550 kg m^{-3} was determined, substantially lower than estimated in earlier studies. From bulk density and grain density, the porosity can be determined. Studies by Wieczorek et al. (2013) reveal that the lunar upper crust is highly fractured. An average porosity of 12% was determined, varying between 4 and 21%. A correlation was found between high crustal porosity and the location of large impact basins, which confirms the idea that crustal fracturing is most likely impact induced.

The derived gravity field models from GRAIL are available in an unrivaled resolution and accuracy compared to other planetary bodies. With data from GRAIL's extended mission (Lemoine et al., 2014) and improved processing strategies, gravity field models of the Moon are now available in higher accuracy and resolution. In this study we map bulk density and the porosity of the lunar crust in high spatial resolution, using most recent gravity and topography data. We assume a homogeneous density of the crust in the vertical, as Wieczorek et al. (2013), and seek for lateral variations. In our approach, we benefit from the fact that the measured gravity signal at short wavelengths strongly correlates with the topography (Turcotte and

Schubert, 2014). In this paper, we applied two separate methods, not contemplating alone on the correlation between gravity anomalies and the overlying topography, but also on the roughness of the anomalies.

3.2 Data

We use the gravity field solution GL1500E from data obtained during the primary and the extended GRAIL mission (Park et al., 2015), which is typically given in a series of spherical harmonic coefficients. The relation between the coefficients (frequency domain) and gridded surface data (spatial domain) may be expressed as

$$f(\theta,\phi) = \sum_{l=0}^{\infty}\sum_{m=0}^{l} \bar{P}_{lm}(\cos\theta)(\bar{c}_{lm}\cos m\phi + \bar{s}_{lm}\sin m\phi) \tag{10}$$

where $\bar{c}_{lm}$ and $\bar{s}_{lm}$ are the given 4π normalized spherical harmonic coefficients of degree l and order m are the fully normalized associated Legendre functions, and θ and ϕ colatitude and longitude, respectively (Hofmann-Wellenhof and Moritz, 2006).

GL1500E has a resolution of spherical harmonic degree and order 1500, corresponding to a spatial grid size of around 7 arcminutes or 3.6 km at the equator. To assess the noise level of the dataset, we compute the root mean square (RMS) power spectra of the gravity signal following Kaula (1966) and compare these with the uncertainties, provided for each gravity coefficient (Figure 17). For degree higher than 910, errors become larger than the power of the signal.

Likewise, we computed the power spectrum of Bouguer anomalies (see explanation later in the text) using a global crustal density of 2550 kg m^{-3} (Wieczorek et al., 2013). The RMS power approaches the GL1500E error near degree 700. Consequently, we decided to truncate the coefficient series at degree and order 700. Also, we removed coefficients smaller than degree 150, to avoid contributions of the crust mantle interface gravity signal (Wieczorek et al., 2013). The remaining set of coefficients is assumed to represent attraction from topography only.

In addition to GRAIL gravity we use the topography from Lunar Orbiter Laser Altimeter (LOLA) (Smith et al., 2017). To match the resolution of the gravity field, we reduced the topography to the same spherical harmonic extension of degree and order 700. Both, topography and gravity field, are given in the principal axis (PA) reference system (NASA, 2008).

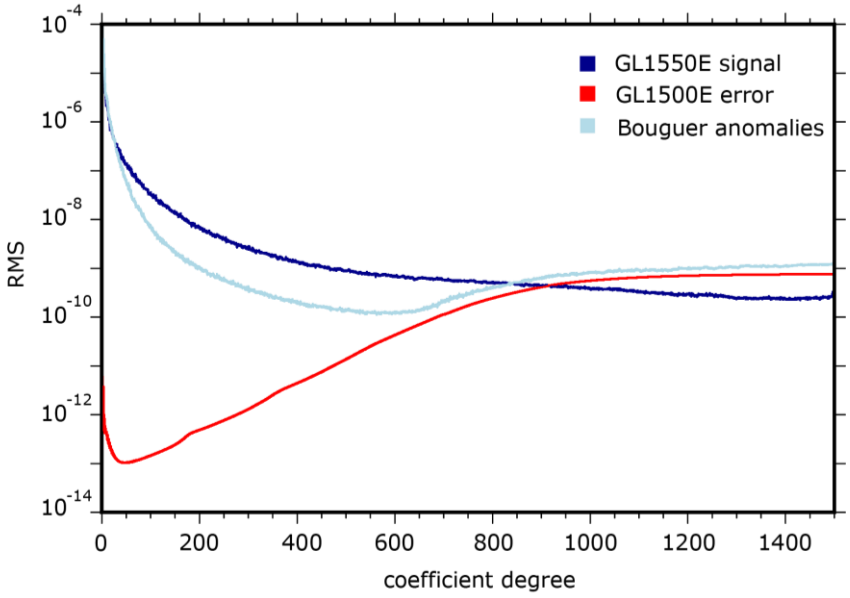

Figure 17: Power spectra of the GRAIL gravity field model GL1500E, the associated uncertainties of the coefficients, and the Bouguer anomalies, calculated with a crustal density of 2550 kg m^{-3}.

3.3 Method

To determine crustal density we benefit from the fact that the short wavelength gravity field (corresponding to high degree coefficients) strongly correlates with the topography (Turcotte and Schubert, 2014). From the given topography and some adopted bulk density ρ, we compute the Bouguer correction, i.e., the gravity attraction of the terrain related to a certain reference radius. The Bouguer correction was then subtracted from the observed gravity field (truncated to degree and order 150 - 700) to determine the best-fit density ρ. For a given surface point a simple model of the Bouguer correction is the infinite plate of thickness h with constant density ρ, where G is the gravitational constant (Hofmann-Wellenhof and Moritz, 2006)

$$g = 2\pi G\rho h\,. \tag{11}$$

However, the method is not applicable if the topography of the surrounding terrain is rough. Instead, the Bouguer correction was calculated applying the finite amplitude method of (Wieczorek and Phillips, 1998), which – like the observed gravity and topography – may be given in terms of spherical harmonic coefficients, and which may be computed from the expression

$$C_{lm} = \frac{4\pi D^3}{M(2l+1)} \sum_{n=1}^{l+3} \frac{(\rho h^n)_{lm}}{D^n n!} \frac{\prod_{j=1}^{n}(l+4-j)}{(l+3)} \tag{12}$$

where h is the terrain above a reference surface of radius D with a constant density ρ (Wieczorek et al., 2006). M denotes the mass of the planetary body. To account for the high resolution of our dataset, we estimated coefficients using power series of topography up to $n = 9$.

Bouguer correction was computed for 20 distinct values of densities varying between 2000 and 3000 kg m^{-3}. Next, Bouguer correction was applied to the observed gravity field, which was downward continued (free-air correction) to the mean elevation of each analysis region. Subtracting normal gravity, we obtain 20 sets of Bouguer anomalies. Assuming a constant density in the vertical direction the resulting signal would be zero if the correct crustal density was applied. If a wrong density was used, gravity attraction from topography is mapped in the Bouguer anomalies (see sketch in Figure 18).

The computation of the bulk density was realized in the spatial domain. Hence, topography and the 20 Bouguer anomaly models were converted to spatial grid space. Due to the high degree and order of the data, classical models for the synthesis as e.g., presented by Hofmann-Wellenhof and Moritz (2006) take a large computational effort and may suffer from numerical instabilities (Gruber et al., 2011). The transformation from the spectral domain to a spatial grid was performed using the shtools archive for Python (Wieczorek and Meschede, 2018). The routine is fast and accurate up to degree 2800 (Wieczorek and Meschede, 2018). We chose a regular sampled grid with equally spaced points in latitude and longitude that conforms the sampling theorem by Driscoll and Healy (1994). The grid, chosen to match the resolution of the given gravity field, has 2 l_{max} + 2 points in latitude and twice the number in longitude direction, i.e., 3002 x 6004 grid points.

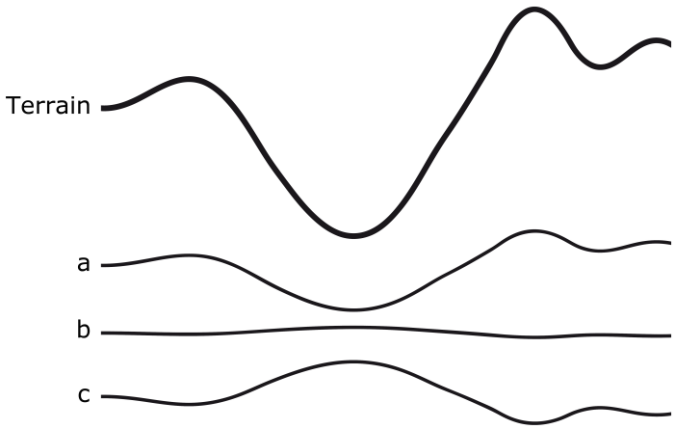

Figure 18: Profiles selected from global data sets, showing topography ("Terrain") and 3 out of 20 Bouguer anomalies, computed using different bulk densities. (a) Applied bulk density too high (b) Applied bulk density just about right. (c) Applied bulk density too low. The best-fit density is found by two different techniques, minimizing the correlation between topography and Bouguer anomalies (Section 3.3.1) or by maximizing smoothness of the Bouguer anomalies (Section 3.3.2).

The analysis was carried out over small circular analysis regions with radii of 3.0°. We used the weighted Pearson correlation scheme (Pozzi et al., 2012) to account for distortion of the circular regions with proximity to the poles. Points within the analysis region were weighted regarding their latitudinal position, to compensate for their different contributions.

A significant fraction of around 17% (Head, 1976) of the surface of the Moon is characterized by basaltic mare regions. Since mare basalt deposits were most likely formed by partial melting of lunar upper mantle cumulates (Smith et al., 1970) and therefore do not represent crustal material, we omitted those regions from our analysis. We used maps of lunar maria by Nelson et al. (2014) to identify and exclude locations, having a contribution of more than 2.5% basalts in the analysis circles.

The uncertainties were estimated by considering the average variation around each individual density value. Since the variation mostly depends on different geological characteristics within the considered region (Besserer et al., 2014), the uncertainties are therefore probably on the pessimistic side.

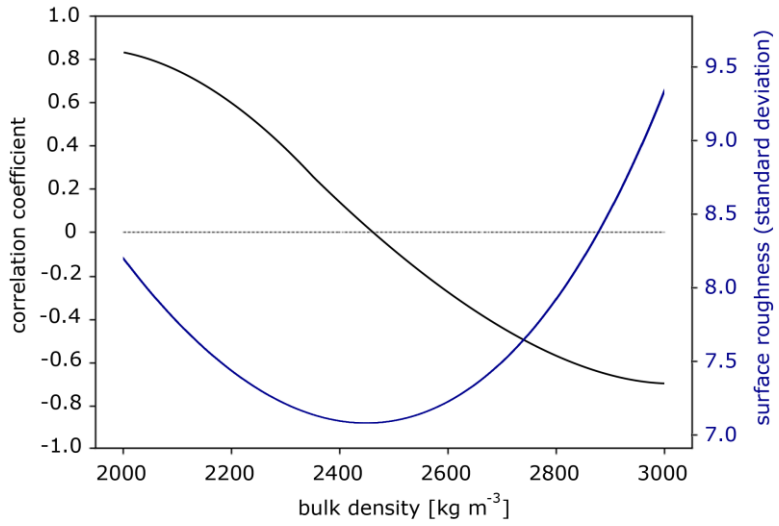

Figure 19: Search for best-fit density for an arbitrary analysis region in the lunar highlands. The black curve shows the determined coefficients of correlation between topography and Bouguer anomalies; best-fit density is found where the curve crosses zero (near 2480 kg m^{-3}). The blue curve shows the estimated standard deviations of the Bouguer anomalies; best-fit density is found where standard deviation is smallest (and thus anomaly is smoothest) (near 2460 kg m^{-3}).

3.3.1 Correlation analysis between Bouguer anomalies and topography

The 20 sets of Bouguer anomalies were analyzed to find the best-fit bulk density in each analysis circle using two distinct techniques. Using the technique of Wieczorek et al. (2013) we computed correlation coefficients between Bouguer anomalies and the terrain. Correct crustal density was found where correlation was at a minimum (see Figure 18 and Figure 19 for sketches).

3.3.2 Roughness of Bouguer anomalies

In the second approach, we computed the standard deviation of the 20 Bouguer anomalies for each analysis circle. Correct density was adopted where standard deviation, i.e., anomaly roughness, was at a minimum (Figure 18 and Figure 19).

3.4 Results

3.4.1 Bulk density map from correlation analysis

The global bulk density map of the upper lunar crust (Figure 20) has 480 x 240 grid elements, corresponding to a grid size of 0.75° (approx. 22.5 km at the equator). The map was derived from gravity and topography data as described above, having a spatial resolution of 0.06°.

Based on degree and order of the truncated spherical harmonic series and the vertical extent of each analysis circle, we estimate bulk density to a depth of several kilometers. We found an average bulk density of 2536 kg m^{-3} with an uncertainty of ±21 kg m^{-3}. A histogram of globally estimated densities is given in Figure 21A. The majority (99.6%) of determined densities are within a range from 2300 to 2900 kg m^{-3}, with only a small number of points beyond.

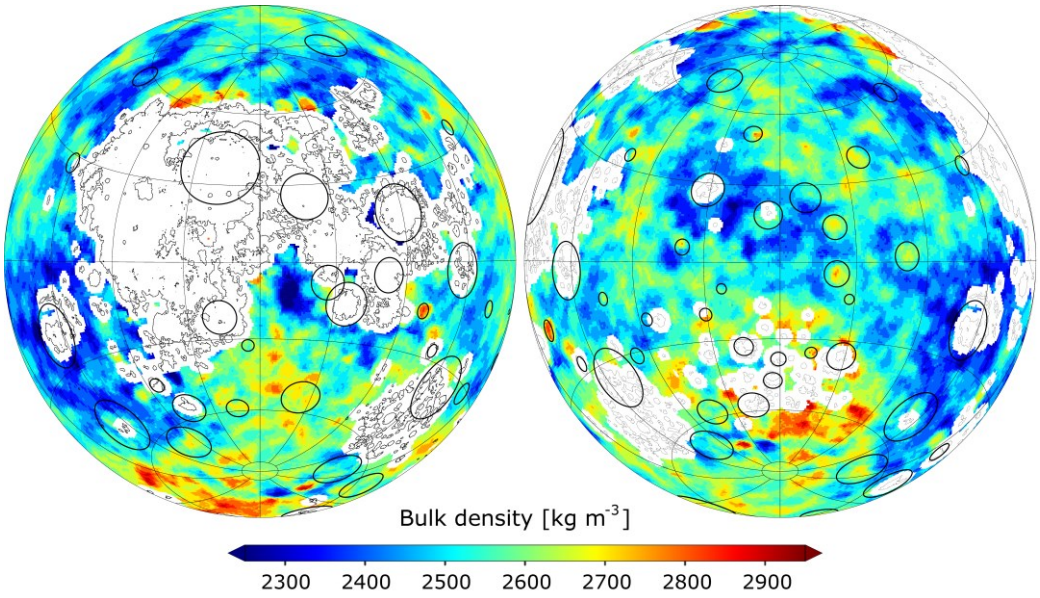

Figure 20: Bulk density of the lunar crust from correlation analysis. The data is mapped in lambert azimuthal equal-area projection, covering a 240° latitude and longitude range (nearside: left; farside: right). Prominent impact basins are marked with black circles. White areas represent lunar maria and are not mapped in our investigation.

For estimating the correlation between topography and Bouguer anomalies, we used a circular analysis region of 3° radius for each grid point. For finding the minimum dimension for the analysis circle, we tested different radii. Since our estimated errors are influenced by geological characteristics of the investigated region, the uncertainties do not give an indication for the right dimension. Huang and Wieczorek (2012) demonstrated that grain densities of the lunar highlands do not exceed 3000 kg m^{-3}. We applied a minimum radius of the analysis circle, where the resulting densities in the highlands remain below the value of 3000 kg m^{-3}.

3.4.2 Bulk density from Bouguer anomaly analysis

We tested a modified method, where, instead of examining the correlation between topography and truncated Bouguer anomalies, the roughness of the truncated Bouguer anomalies were considered. We applied the same conditions as in the correlation approach, using circular analysis region of 3.0° radius on a regular grid of 0.75°. An average bulk density of 2503 kg m^{-3} with an uncertainty of ±22 kg m^{-3} was estimated.

Results for most areas agree with those of the correlation approach, which supports the validity of the two methods. Overall, the Bouguer roughness approach exhibits slightly lower densities, compared to the correlation approach (Figure 21). For 3% of the areas on the global map larger differences occur, which will be examined in the discussion section.

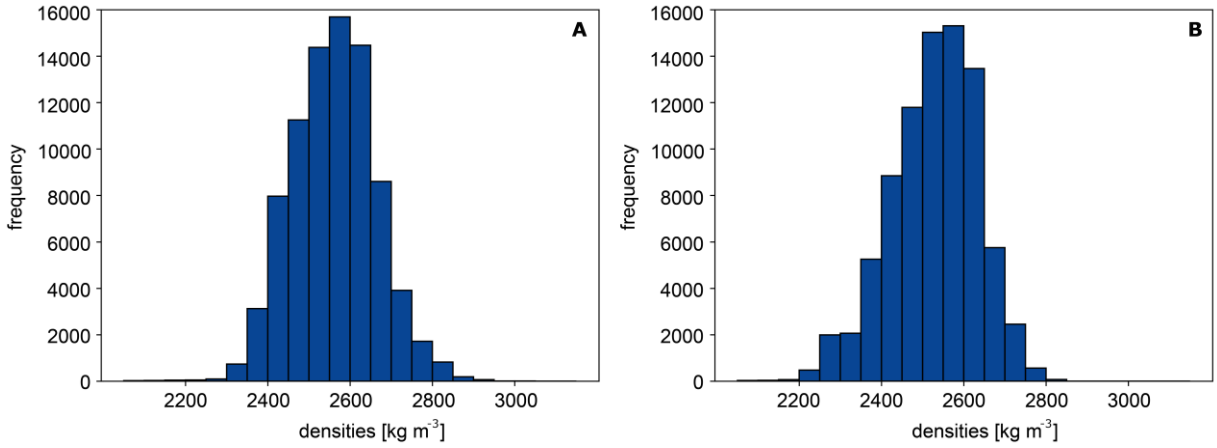

Figure 21: Frequency of the globally determined bulk densities. (A) Histogram of global crustal density estimates from correlation analysis. (B) Histogram of global crustal density estimates from Bouguer anomaly roughness.

3.4.3 Porosity

Porosity is the fraction of the volume made up of pore space (Turcotte and Schubert, 2014). For calculating the porosity, bulk densities as well as the grain densities need to be known. We benefit from the fact that average grain densities of lunar rocks are proportional to abundances of their main chemical constituents. Following Huang and Wieczorek (2012) we used titanium abundances from gamma ray spectrometer data (Prettyman et al., 2006) obtained by the Lunar Prospector mission to map the grain density of the upper crust. The porosity ϕ was then determined from the relation

$$\phi = 1 - \frac{\rho_{bulk}}{\rho_{grain}} \ . \tag{13}$$

Maps (Figure 22) were prepared in matching formats as those in Figure 20. For the highland upper crust of the Moon an average of 13% porosity for the correlation approach and 14% porosity for the Bouguer roughness approach was determined. As it can be seen in Huang and Wieczorek (2012), grain densities are quite similar over the globe, with the only exception of Procellarum KREEP Terrane (PKT). Apart from PKT densities may vary locally only by up to 2%. Therefore, we may conclude that our observed lateral variations in bulk density are mainly induced by the variations in porosity of lunar rock.

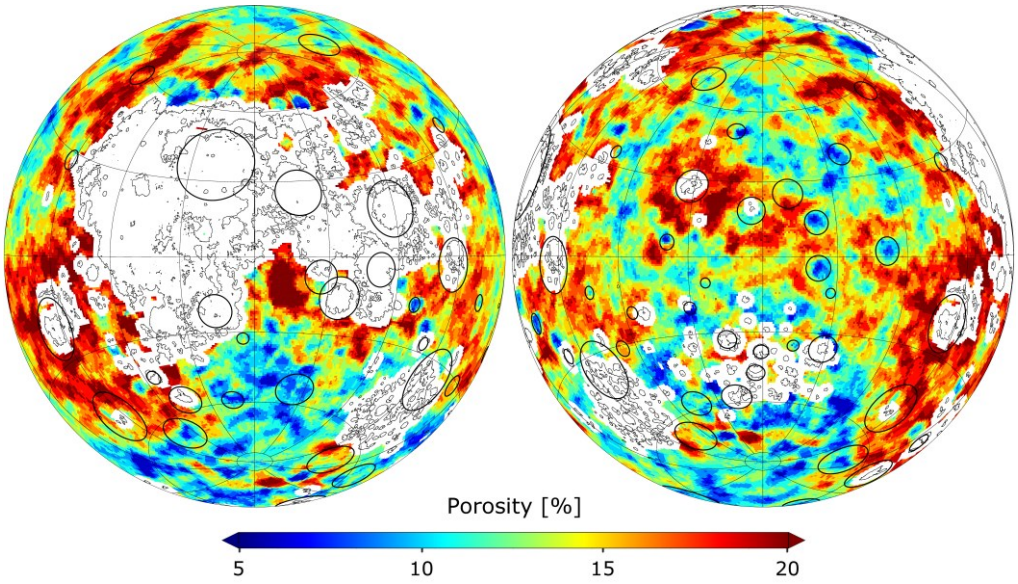

Figure 22: Porosity of the lunar crust (bulk densities were estimated applying the correlation approach). Projection and labels as in Figure 20.

3.5 Discussion

Our results agree with those from earlier studies by Wieczorek et al. (2013) and Goossens et al. (2018), who determined an average bulk density of the upper crust of 2550 ± 18 kg m^{-3} (GL0420A gravity model) and 2587 ± 54 kg m^{-3} (GRGM900C gravity model), respectively. The porosity of 12% in the study by Wieczorek et al. (2013) is slightly smaller than our estimated average of 13%, using the correlation approach, and 14%, considering the Bouguer anomaly roughness.

The derived maps, showing lateral variations in bulk density and porosity of the upper lunar highland crust, have a resolution two times higher compared to the maps of (Wieczorek et al., 2013). Due to the high level of detail we found evidence for significant regional variety in near-surface composition and physical properties. The high-resolution maps reveal a coherence between impact basins and the porosity of the lunar crust. An example is given in Figure 23, showing the Korolev farside basin, with a diameter of 417 km (Neumann et al., 2015). Within the inner ring of the basin, the upper crust possesses low porosity of 5%, likely caused by compaction of the target rock and the formation of dense impact melt (Melosh, 1989). In contrast, the region towards the outer rim holds high porosities of around 15%. These areas were probably affected by the shock wave during the contact and compression stage (Melosh, 1989), which caused fracturing and brecciation of the rock (Collins, 2014). These findings confirm earlier investigations suggesting that impact induced fracturing is the primary mechanism forming the porous upper crust of the Moon and other terrestrial planets (Collins, 2014; Soderblom et al., 2015). The high spatial resolution of the maps will enable further studies focusing on the geophysical characteristics of single impact basins.

To obtain the best-fit density, we used two distinct methods. For most areas (97%) results are similar, not different by more than 100 kg m^{-3}. However, in particular regions (e.g., at the edge to the Procellarum KREEP Terrane, especially at the northern rim) large differences of up to 700 kg m^{-3} are seen. To find out the reason for the differences, we mapped topographic roughness, using the standard deviation of topographic data points within the same circular analysis regions, which were used for determining the bulk density. We found that different bulk density solutions are typically found in areas of low surface roughness. An example is demonstrated in Figure 24, for a region at the northern boundary of the PKT.

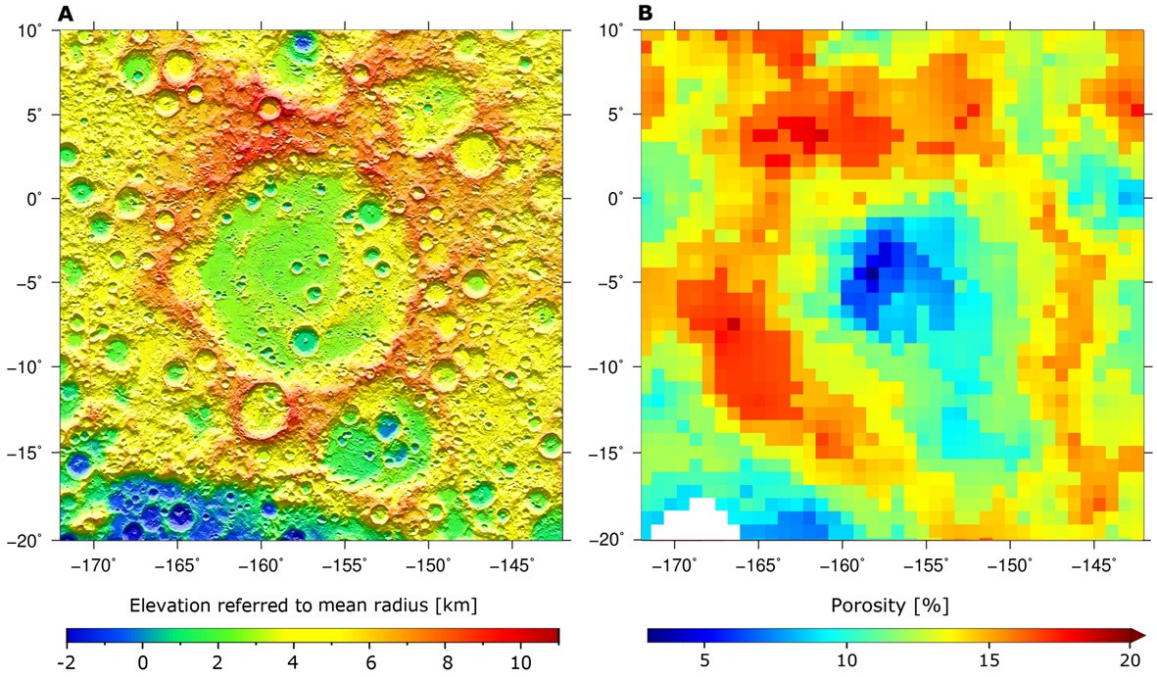

Figure 23: Korolev impact basin. The maps are presented in Mercator projection, with its meridian placed in the center of the basin. (A) Digital terrain model derived from LOLA data (Smith et al., 2017), elevations refer to mean topography radius of 1737.151 km, (B) Porosity of the upper lunar crust.

A smooth surface, lacking topographic features, is a challenge for both methods. Usually, if a wrong density was applied, surface attributes are mapped in the Bouguer anomalies. The anomalies become rough and a correlation with the topography is found. If topographic features lack, any difference can be made between a wrong and the correct density which was used. The situation is similar for regions of lunar maria: Also here topography exhibits only few landforms and craters, so that most of the areas are flat. In the present work, mare regions were omitted from the analysis in particular due to their different composition and origin compared to lunar highland crust (see earlier explanations). But the surface characteristics also make it difficult to achieve meaningful results in those areas.

The highest bulk densities can be found in the region of South Pole-Aitken basin (SPA), the oldest impact basin on the Moon (Wilhelms, 1987). With a diameter of about 2400 km (Neumann et al., 2015) it represents the largest impact basin in the Solar System. Unfortunately, SPA shows a number of distinct patches of mare basalts, which were excluded from our mapping, why a statement regarding its properties is only possible to a limited extent. As remote sensing data reveals, SPA exhibits a high abundance in pyroxenes, even though the proportions vary within the basin (Moriarty and Pieters, 2018). This mineral most likely originates from the lower crust and/or upper mantle and has a higher density than the anorthosite highland crust (Kiefer et al., 2012), which may explain the high bulk density found in SPA.

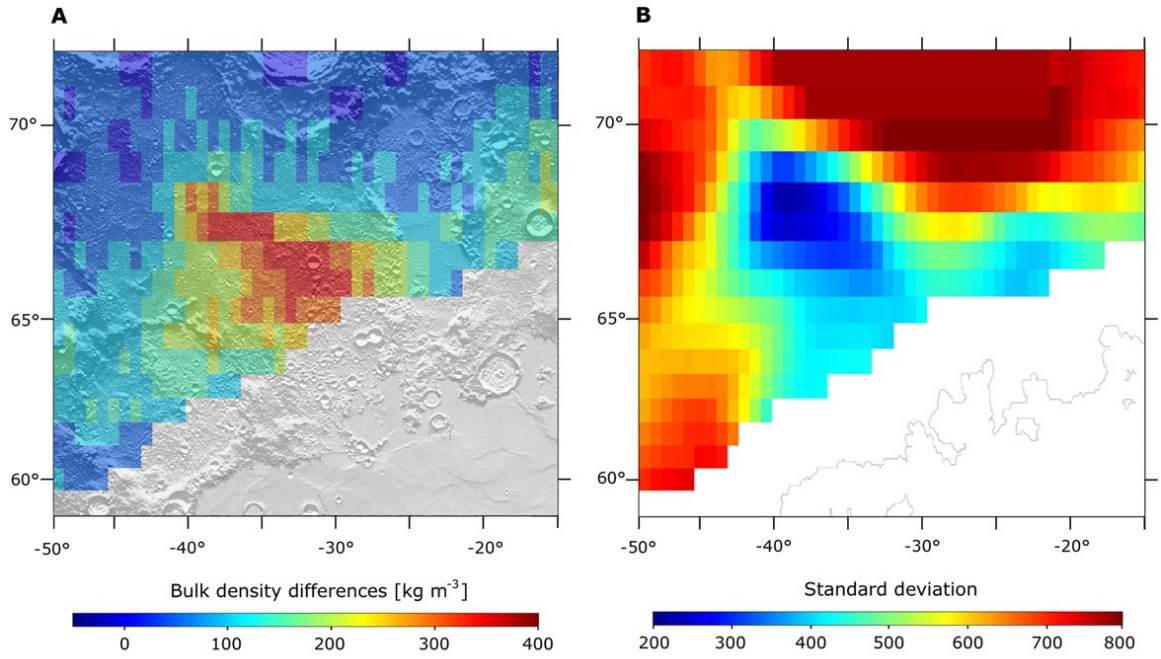

Figure 24: Region of large inconsistence of the two tested methods at the northern rim of PKT. (A) Bulk density difference (bulk density from correlation between topography and Bouguer anomalies minus bulk density from Bouguer roughness) with shaded topography in the background. (B) Surface roughness, given as the standard deviation of the topography.

3.6 Conclusion and Outlook

We mapped lateral variations of bulk density and porosity of the lunar highland crust using most recent high-resolution GRAIL gravity and LOLA topography data. For calculating the density, two methods were demonstrated, both of which yield similar results for most of the studied areas. Both methods suffer in the case of a smooth topography. Consequently, the two methods show significantly different results of up to 700 kg m^{-3} in such areas.

Using global grain densities derived from remote sensing data, we also estimated the porosity of the upper lunar crust. From inspection of the data, we conclude that differences in the bulk density are mostly determined by differences in crustal porosity, not by differences in the statistics of chemical compounds. We demonstrate that high porosity correlates with areas around impact basins, which suggests that the fracturing is most likely impact-induced.

With the present high-resolution datasets, it is possible to study impact structures in more detail. We will take a closer look at single basins regarding their variations in porosity and investigate their characteristics in terms of dimension and age.

Accurate bulk densities near the surface are important for studies of deeper crustal structures. Rather than using one average value, the high-resolution bulk density maps can be used to calculate mass variations at the crust-mantle boundary with individual values for different areas.

Acknowledgements

We gratefully acknowledge Mark Wieczorek for helpful discussions and advice. We also would like to thank two anonymous reviewers for critical comments and suggestions, which helped improving the manuscript. This work was funded by the Deutsche Forschungsgemeinschaft (SFB-TRR 170, subproject A04-60).

References

Besserer, J., Nimmo, F., Wieczorek, M.A., Weber, R.C., Kiefer, W S., McGovern, P.J., Andrews-Hanna, J.C., Smith, D.E. and Zuber, M.T., 2014. GRAIL gravity constraints on the vertical and lateral density structure of the lunar crust. Geophysical Research Letters 41(16), 5771–5777.

Collins, G.S., 2014. Numerical simulations of impact crater formation with dilatancy. Journal of Geophysical Research 119(12), 2600–2619.

Driscoll, J.R. and Healy, D.M., 1994. Computing fourier transforms and convolutions on the 2-sphere, 202-250.

Goossens, S., Sabaka, T.J., Genova, A., Mazarico, E., Nicholas, J.B. and Neumann, G.A., 2017. Evidence for a low bulk crustal density for Mars from gravity and topography. Geophysical Research Letters 44(15), 7686–7694.

Gruber, C., Novak, P. and Sebera, J., 2011. FFT-based high-performance spherical harmonic transformation. Studia Geophysica et Geodaetica 55(3), 489-500.

Head, J.W., 1976. Lunar volcanism in space and time. Reviews of Geophysics and Space Physics 14(2), 265–300.

Hofmann-Wellenhof, B. and Moritz, H. (2006) Physical Geodesy, 2nd edition Springer, Wien, pp. 403.

Huang, Q. and Wieczorek, M.A., 2012. Density and porosity of the lunar crust from gravity and topography. Journal of Geophysical Research: Planets, 117(5), 1-9.

Kaula, W., 1966. Theory of Satellite Geodesy. Blaisdell Puplishing Company, Waltham, Mass. (republished by Dover, New York, 2000), 5303-5314.

Kiefer, W.S., Macke, R.J., Britt, D.T. and Irving, A.J., 2012. The density and porosity of lunar rocks. Geophysical Research Letters 39, 1–5.

Lemoine, F.G., Goossens, S., Sabaka, T.J., Nicholas, J.B., Mazarico, E., Rowlands, D.D., Loomis, B.D., Chinn, D.S., Neumann, G.A., Smith, D.E. and Zuber, M.T., 2014. GRGM900C: A degree 900 lunar gravity model from GRAIL primary and extended mission data. Geophysical Research Letters 41(10), 3382–3389.

Melosh, H.J. (1989) Impact cratering: A geologic process. Research supported by NASA. New York, Oxford University Press, pp. 253.

Moriarty, D.P. and Pieters, C.M., 2018. The Character of South Pole-Aitken Basin: Patterns of Surface and Subsurface Composition. Journal of Geophysical Research: Planets 123, 729–747.

NASA, 2008. A Standardized Lunar Coordinate System for the Lunar Reconnaissance Orbiter and Lunar Datasets. Vol. 5, NASA Goddard Space Flight Center, Greenbelt, Md., pp. 13.

Nelson, D.M., Koeber, S.D., Daud, K., Robinson, M.S., Watters, T., Banks, M. and Williams, N.R., 2014. Mapping Lunar Maria Extents and Lobate Scarps Using LROC Image Products. Lunar and Planetary Science Conference. Abstract #2861.

Neumann, G.A., Zuber, M.T., Wieczorek, M.A., Head, J.W., Baker, D.M.H., Solomon, S.C., Smith, D.E., Lemoine, F.G., Mazarico, E., Sabaka, T.J., Goossens, S.J., Melosh, H.J., Phillips, R.J., Asmar, S.W., Konopliv, A.S., Williams, J.G., Sori, M.M., Soderblom, J.M., Miljkovic, K., Andrews-Hanna, J.C., Nimmo, F. and Kiefer, W.S., 2015. Lunar impact basins revealed by Gravity Recovery and Interior Laboratory measurements. Science Advances 1(9), 1-10.

Park, R.S., Konopliv, A.S., Yuan, D., Asmar, S., Watkins, M., Williams, J., Smith, D.E. and Zuber, M.T., 2015. A high-resolution spherical harmonic degree 1500 lunar field from the grail mission. AGU Fall Meeting, Abstract #G41B-01.

Pozzi, F., Di Matteo, T., and Aste, T., 2012. Exponential smoothing weighted correlations. European Physical Journal B 85(6), 1–21.

Prettyman, T.H., Hagerty, J.J., Elphic, R.C., Feldman, W.C., Lawrence, D.J., McKinney, G.W. and Vaniman, D.T., 2006. Elemental composition of the lunar surface: Analysis of gamma ray spectroscopy data from Lunar Prospector. Journal of Geophysical Research: Planets 111(12), 1–41.

Smith, D.E., Zuber, M.T., Neumann, G.A., Mazarico, E., Lemoine, F.G., Head, J.W., Lucey, P.G., Aharonson, O., Robinson, M.S., Sun, X., Torrence, M.H., Barker, M.K., Oberst, J., Duxbury, T.C., Mao, D., Barnouin, O.S., Jha, K., Rowlands, D.D., Goossens, S., Baker, D., Bauer, S., Gläser, P., Lemelin, M., Rosenburg, M., Sori, M.M., Whitten, J. and Mcclanahan, T., 2017. Summary of the results from the lunar orbiter laser altimeter after seven years in lunar orbit. Icarus 283, 70–91.

Smith, J.V., Anderson, A.T., Newton, R.C., Olsen, E.J., Crewe, A.V., Isaacson, M.S., Johnson, D. and Wyllie, P.J., 1970. Petrologic history of the moon inferred from petrography, mineralogy and petrogenesis of apollo 11 rocks. Geochimica et Cosmochimica Acta Supplement, Volume 1. Proceedings of the Apollo 11 Lunar Science Conference held 5-8 January, 1970 in Houston, TX.: Mineraolgy and Petrology. Edited by A. A. Levinson. New York: Pergammon Press, 1970. 1, 897–925.

Soderblom, J.M., Evans, A.J., Johnson, B.C., Melosh, H.J., Miljkovi, K., Phillips, R.J., Andrews-Hanna, J.C., Bierson, C.J., Head, J.W., Milbury, C., Neumann, G. A., Nimmo, F., Smith, D.E., Solomon, S.C. and Sori, M.M., 2015. The fractured Moon: Production and saturation of porosity in the lunar highlands from impact cratering. 6939-6944.

Turcotte, D. and Schubert, G., 2014. Geodynamics, 3rd edition. Cambridge University Press, Cambridge, pp. 636.

Wieczorek, M.A., 2009. Gravity and topography of the terrestrial planets. In: G. Schubert and T. Spohn (eds), Treatise on Geophysics, Vol. 10, Elsevier, Amsterdam, 165–206.

Wieczorek, M.A. and Meschede, M., 2018. SHTools: Tools for Working with Spherical Harmonics. Geochemistry, Geophysics, Geosystems 19(8), 2574-2592.

Wieczorek, M.A. and Phillips, R.J., 1998. Potential anomalies on a sphere: Applications to the thickness of the lunar crust. Journal of Geophysical Research 103(97), 1715–1724.

Wieczorek, M.A., Neumann, G.A., Nimmo, F., Kiefer, W.S., Taylor, J.G., Melosh, H.J., Phillips, R.J., Solomon, S.C., Andrews-Hanna, J.C., Asmar, S.W., Konopliv, A.S., Lemoine, F.G., Smith, D.E., Watkins, M.M., Williams, J.G. and Zuber, M.T., 2013. The Crust of the Moon as Seen by GRAIL. Science 339, 671–675.

Wilhelms, D.E., 1987. The geological history of the Moon. United States Geological Survey Professional Paper 1348, Washington, pp. 302.

Zuber, M.T., Smith, D.E., Watkins, M.M., Asmar, S.W., Konopliv, A.S., Lemoine, F.G., Melosh, H.J., Neumann, G.A., Phillips, R.J., Solomon, S.C.,Wieczorek, M.A., Williams, J.G., Goossens, S.J., Kruizinga, G., Mazarico, E., Park, R.S. and Yuan, D.-N., 2013. Gravity Field of the Moon from the Gravity Recovery and Interior Laboratory (GRAIL) Mission. Science 339, 2011–2014.

4. Research paper II

Published in Journal of Geophysical Research: Planets
doi: 10.1029/2019JE006335
Open Access publication, Creative Common Attribution 4.0
- postprint version -

Crustal porosity of lunar impact basins

Daniel Wahl [1], Mark A. Wieczorek [2], Kai Wünnemann [3,4], Jürgen Oberst [1,5]

[1] Technische Universität Berlin, Chair of Planetary Geodesy, Berlin, Germany

[2] Université Cote d'Azur, Observatoire de la Cote d'Azur, CNRS, Laboratoire Lagrange, Nice, France

[3] Museum für Naturkunde, Leibniz Institute for Evolution and Biodiversity Science, Berlin, Germany

[4] Freie Universität Berlin, Institut für Geologische Wissenschaften, Berlin, Germany

[5] German Aerospace Center (DLR), Institute of Planetary Research, Berlin, Germany

Key Points

- The bulk density and porosity of the upper highland crust are revisited using a high-resolution GRAIL gravity field model in combination with LOLA topography and independently estimated grain densities
- For many impact basins, porosity is reduced within their peak ring and increased near and just exterior to the main rim
- Large impact basins show a stronger pronounced porosity signature than smaller basins, and old impact basins reveal a muted porosity signature compared to younger basins

Abstract

Lateral variations in bulk density and porosity of the upper lunar highland crust are mapped using a high-resolution Gravity Recovery and Interior Laboratory (GRAIL) gravity field model and Lunar Reconnaissance Orbiter (LRO) derived topography. With a higher spatial resolution gravity model than previous studies, we focus on individual impact basins with diameters greater than 200 km. The bulk density of the upper few kilometers of the lunar crust is estimated by minimizing the correlation between the topography and Bouguer gravity at short wavelengths that are unaffected by lithospheric flexure. Porosity is then derived using estimates of the grain density obtained from remote sensing data of the surface composition. The near surface crust in proximity to many large basins is found to exhibit distinct radial porosity signatures. Low porosities are found in the basin centers within the peak ring whereas high porosities are identified near and just exterior to the main rim. The larger basins exhibit a more pronounced porosity signature than the smaller basins. Though the number of basins investigated in this study is limited, younger basins appear to be associated with the largest amplitude variations in porosity. For basins with increasing age the magnitude of the porosity variations decreases.

Plain Language Summary

The gravity field surrounding an impact basin allows us to investigate the properties of the underlying crust and to better understand how craters form and evolve. In the center of the largest lunar craters, the impact basins, positive mass anomalies can be found that are caused by the excavation of crustal materials and the uplift of the mantle during formation. When using only the short wavelength portion of the gravity field, signals from these deeper regions are masked, and this allows us to estimate both the density and porosity of the upper crust. We investigated the crustal porosity of impact basins located in the lunar highlands, with diameters larger than 200 km. Many of these basins reveal similar porosity signatures, having low porosities in their center and high porosities near the crater rim. For the most pristine basins, the magnitude of the porosity variations increases with increasing basin size. Furthermore, the crustal porosity is influenced by the formation age of a basin, where the older basins have more muted signatures than younger basins.

4.1 Introduction

High resolution data from the GRAIL mission (Zuber et al., 2013) allowed to investigate physical characteristics of the lunar interior. In combination with topography data, variations in bulk density of the lunar crust can be investigated (e.g., Wieczorek et al., 2013; Besserer et al., 2014) and when compared with independent knowledge of mineral grain densities based on remote sensing data, the porosity of crustal materials can be estimated. The main result of these studies is that the crust of the Moon exhibits high porosities, between about 4 and 21%, with an average of about 12%. While the interiors of many impact basins were found to have lower porosities, the two youngest and largest basins on the Moon, Moscoviense and Orientale, show particular high porosities in their surroundings (Wieczorek et al., 2013). Later work by Besserer et al. (2014) confirmed the high crustal porosities and placed constraints on how porosity decreases with depth below the surface.

The porosity of lunar impact craters was investigated by Soderblom et al. (2015) by analyzing their Bouguer gravity signatures. In order to avoid the contribution of the gravity signal caused by the uplift of mantle material (e.g., Wieczorek and Phillips, 1998; Melosh et al., 2013), their study was restricted to complex craters with diameters smaller than 200 km. It was determined that preimpact porosity of the target material (estimated from the regional value far from the crater) controls the magnitude of the Bouguer gravity anomaly. Impacts in targets with initially low porosity were found to result in a negative Bouguer anomaly, which they interpreted as being caused by the fragmentation of the underlying target rock. In contrast, impacts in target materials with high preimpact porosity result in positive Bouguer anomalies, which they attributed to compaction of the target rock leading to a reduced porosity.

Similar effects were found based on numerical simulations of impact crater formation, suggesting a major influence of the preimpact porosity on the final outcome. Milbury et al. (2015) simulated the formation of complex craters using the iSALE shock physics code (Collins et al., 2004; Wünnemann et al., 2006) and investigated the resulting crater porosity by analyzing the computed Bouguer gravity. While preimpact target porosities up to a maximum of 7% result in negative Bouguer anomalies (indicating higher postimpact porosities), initial porosities greater than 7% result in positive Bouguer anomalies (indicating lower postimpact porosities). In target materials with high preimpact porosity, the impact induced shock wave crushes out pre-existing fractures and compresses the material (Wünnemann et al., 2006), causing a reduction of porosity (Milbury et al., 2015). At further distances, the pre-existing porosity remains intact (Milbury et al., 2015), caused by a more efficient decay of the pressure wave in porous targets (Love et al.,

1993). In contrast, for target material with a low preimpact porosity, the energy is transported more efficiently, causing fracturing of rocks also in larger distance to the point of impact.

Examples from Earth show that regions of high porosity are to be expected within and surrounding impact basins. Rocks obtained from the central peak region of the Chicxulub impact structure in Mexico show strong fracturing. Analysis of the drill core samples revealed an average porosity of 11.5% for depths between 850 and 1250 m below the surface, whereas porosities as high as 20% were found in the uppermost portion of the drill core between 750 and 850 m depth (Rae et al., 2019). The high porosity is primarily caused by intragranular microfracturing, induced by the impact generated shock wave. The occurrence of cataclasites in the samples, having a high porosity but being small in volume, has only a minor contribution on the overall porosity of the rocks. Another well studied impact structure on Earth is the Ries crater in Germany. From the bulk densities of rock samples obtained from two drill cores, Förstner (1967) estimated the related porosity. The drill core in Wörnitzostheim, located between the inner ring and the outer crater rim, revealed a mean porosity of about 28% (at depths between 37 and 74 m), while the drill core taken in Deiningen, located close to the inner ring, shows porosities of up to 34% at depths between 311 and 350 m. Many terrestrial impact craters (including Chicxulub and Ries) show prominent negative Bouguer gravity signatures that are result of impact induced porosity (e.g., Rae et al., 2019; Pilkington and Grieve, 1992; Pohl et al., 1977).

Samples from the Apollo program as well as lunar meteorites, have been used to study the porosity of lunar rocks. For feldspatic material associated with the lunar highlands, Kiefer et al. (2012) found porosities between 2 and 20%. Impact breccias revealed the highest porosities of about 20%, while the feldspatic lunar meteorites hold the lowest porosities with values between 2 and 11.5%. Their results are consistent with those reported by Wieczorek et al. (2013) who studied 24 feldspatic Apollo samples and meteorites, finding porosities between 1 and 20%, with an average of 8.6 ± 5.3%. While considerations limited to Apollo samples collected at the surface might not capture the full range of all possible porosity characteristics, porosities of lunar meteorites may be biased to lower values due to the processes associated with ejection from the lunar surface and entry in Earth's atmosphere (Warren, 2001).

Since the first GRAIL investigations regarding crustal porosity, improved models of the Moon's gravity field have been derived with higher spatial resolutions and accuracies. The 420 degree and order model of Zuber et al. (2013) was employed by Wieczorek et al. (2013), whereas in the later work of Besserer et al. (2014) the 900 degree and order model of Lemoine et al. (2014) was used. In the present work, we made use of the most recent gravity model of Park et al. (2015), which is developed to spherical harmonic degree and order 1500. The higher

resolution of this model allows a detailed investigation of the porosity structure of individual impact basins on the Moon that was not possible in previous studies. Our approach to estimate the crustal density and porosity follows the method used by Wieczorek et al. (2013). By minimizing the correlation between the surface topography and the Bouguer gravity (using only the short wavelength signal that is unaffected by lithospheric flexure), bulk density variations of the highland crust were determined. In combination with independent knowledge of grain densities of the upper crust, the porosity of the upper crust was then calculated. With our derived maps we are able to study how the porosity variations are related to the structure of the basin, and also to quantify how the magnitude of the porosity signature varies with crater size and age.

In section 4.2, we describe how the new bulk density and porosity maps used in this study were constructed. In section 4.3.1, we present the global characteristics of the density and porosity model, and in section 4.3.2, we then systematically investigate the porosity signatures of large impact basins in the lunar highlands with diameters larger than 200 km. Finally, in section 4.4, we discuss several aspects related to the porosity signatures of the investigated impact basins, including how they are related to basin size and age.

4.2 Data and Methods

As a result of the GRAIL mission, the gravity field of the Moon is known with unprecedented accuracy and resolution. We made use of the most recent gravity field model GL1500E (Park et al., 2015; Konopliv et al., 2014) provided as spherical harmonic coefficients developed to degree and order 1500 (which corresponds to a spatial resolution of about 3.6 km). The effective resolution of the model, however, is highly dependent on the coverage of the low altitude data obtained at the end of the mission. To account for this variability in spatial resolution, we truncate the spherical harmonic coefficients at a maximum degree that is globally well resolved by the model. As shown in Figure 25, the power spectra of the gravity field and their related errors intersect at about degree 900, indicating that beyond this degree the global coefficients are poorly resolved.

A different indicator of the model's resolution comes from the spectrum of the Bouguer gravity. The Bouguer gravity represents the signal that remains after removing the expected signal of the surface topography from the free-air gravity (here using a crustal density of 2550 kg m^{-3}). The power of this signal decreases until about degree 700, at which point the power begins to increase. Beyond this degree, the power of the Bouguer gravity is very similar to the error spectrum of the gravity field, and we interpret the increase in power beyond degree 700 as noise in the global spherical harmonic coefficients. We note that Wieczorek et al. (2013)

truncated the gravity model at degree 310 whereas Besserer et al. (2014) truncated the field at degree 550. Thus, in comparison to Wieczorek et al. (2013), our derived density and porosity maps should have a resolution that is better by a factor of about two.

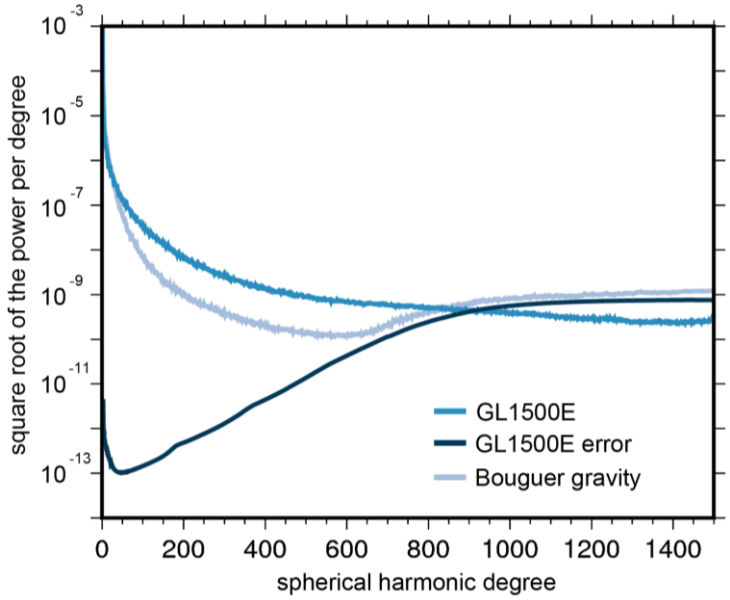

Figure 25: Power spectrum of the GRAIL gravity field model GL1500E (Park et al., 2015), the related error spectrum, and the power of the Bouguer gravity (computed using a crustal density of 2550 kg m^{-3}).

The topography model was derived from measurements made by the Lunar Orbiter Laser Altimeter (LOLA; Smith et al., 2017). We employed the model LOLA2600p of Wieczorek (2015) which is a spherical harmonic expansion of the gridded data products archived on the NASA Planetary Data System. To match the resolution of the gravity field, we truncated the spherical harmonic series of the topographic model to the same degree and order as the gravity model. We note that both the topography and gravity field are given in the same principal axis (PA) reference frame (NASA, 2008).

We estimated the bulk density of the upper crust using techniques developed by Wieczorek et al. (2013), which were later elaborated by Wahl and Oberst (2019). In the approach, the Bouguer gravity is first determined by removing the gravitational signal of the surface topography from the observed gravity (both downward continued to the mean planetary radius). If all gravity anomalies were the result of surface topography, the Bouguer gravity would be zero if the correct density was chosen. Introducing an incorrect density value, the Bouguer gravity would be non-zero and show a correlation with the topography. The density can thus be determined, by ensuring that the correlation between Bouguer gravity and topography is as small as possible. The correlation between the two fields was computed locally, using data collected on a grid

within a circle placed on the surface, and calculating the correlation coefficient we ensured that each point was weighted by its corresponding surface area. Before computing grids of the Bouguer gravity and topography, we first filtered out the longest wavelengths that could be influenced by lithospheric flexure. In particular, Wieczorek et al. (2013) showed that for degrees larger than 150, the gravitational signal resulting from the deflection of the crust-mantle interface is exceedingly small, regardless of what value is assumed for the lithospheric thickness. We accordingly set the spherical harmonic coefficients of these fields to zero for all degrees less than 150.

As described further in Wahl and Oberst (2019) we quantify the local variability of the bulk density based on the variance of the density estimates about a given analysis point. For this, we simply calculated the standard deviation of each point in relation to the neighboring values. Areas covered with mare were not considered in our study given that the density structure of the crust in these regions is complex, with dense basalts overlying less dense highland materials (Gong et al., 2016). In order to prevent dense mare basalts from biasing the results, we rejected estimated bulk densities where more than 2.5% of mare were present in the analysis region. All spherical harmonic analyses were performed using the freely available python-based pyshtools software package (Wieczorek and Meschede, 2018), and we make use of perceptually uniform colormaps generated by Crameri (2018).

After obtaining the bulk density, the porosity can be estimated if the grain density is known independently. Huang and Wieczorek (2012) showed that the grain density of common lunar rocks has a linear dependence on both FeO and TiO_2 abundances. In fact, the uncertainty in this dependence (±64 kg m^{-3}; Huang and Wieczorek, 2012) is comparable to the uncertainty of our bulk density estimates (±21 kg m^{-3}). Using the grain density map of Huang and Wieczorek (2012), for each analysis region we determine the average grain density and then calculate the porosity using the relation

$$\phi = 1 - \frac{\rho_{bulk}}{\rho_{grain}} \ . \tag{14}$$

Finally, we note that the bulk density and porosity obtained in this study are representative of the upper few kilometers of the crust. In particular, for each analysis region, the density is representative of the material located between the highest and lowest elevations, and for most regions this is approximately 4 km. For any location considered in our analysis, we expect the crust to be thinner than a few kilometers. Besserer et al. (2014) showed that the porosity is expected to decrease with depth, but that some porosity would still be present at the base of the crust.

4.3 Bulk density and porosity of the upper crust

4.3.1 Global consideration

Following the methods described above, we produced a global map of the bulk density of the upper crust of the Moon, which is shown in Figure 26. Mare areas (Nelson et al., 2014) are outlined with thin black lines and impact basins with diameters greater than 200 km (Neumann et al., 2015) are delineated by solid black circles. Analyses were performed on an equal area grid with a spacing of 0.75°, and bulk density analyses were carried out using the gravity and topography data within circles with a radius of 3° (about 90 km at the equator). The spatial resolution was chosen based on tradeoffs between the variance of the global maps, the uncertainties of the analyses, and expectations based on the maximum and minimum densities (and porosities). Our analyses thus have a spatial resolution that is two times better than in the initial study of Wieczorek et al. (2013), which is to be expected, given that the maximum spherical harmonic degree they employed (310) is about half of the value used here (700). Regardless, we note that none of our conclusions presented here are sensitive to changes in the radius of the analysis regions from 1.5° to 4.5° (corresponding to diameters of 90 km and 272 km, respectively).

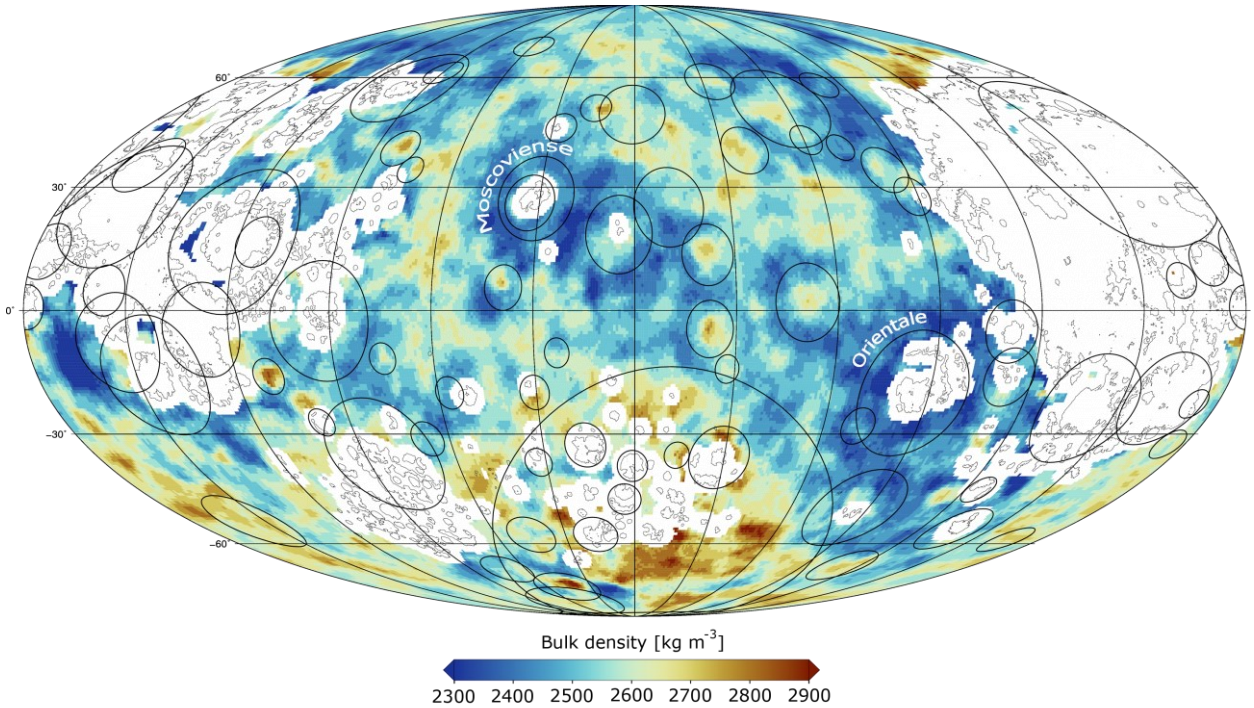

Figure 26: Bulk density of the upper crust. The map is shown using a Mollweide equal area projection, centered over the lunar farside at 180° E, 0° N. Impact basin main rims with diameters larger than 200 km are outlined by black circles and the mare, which were not considered in our study, are outlined in thin black lines. Regions, where analyses were not performed are shown as white. Each bulk density plotted in this map represents an average within a circle with a radius of 3° latitude. The mare basalt map is taken from Nelson et al. (2014).

Averaging the local bulk densities in Figure 26, we compute a mean bulk density of the highland crust of 2536 ± 21 kg m^{-3}. This value is consistent within uncertainties to the value of 2550 ± 18 kg m^{-3} from Wieczorek et al. (2013). The density is seen to vary from values as low as 2300 kg m^{-3} to as high as 2900 kg m^{-3}. The bulk densities are also seen to be higher within the farside South Pole-Aitken basin (~2700 kg m^{-3}) than in the surrounding highlands (~2500 kg m^{-3}). The Orientale and Moscoviense basins are associated with prominent density lows exterior to their peak rings. Furthermore, several of the smaller farside basins, that do not possess interior mare, are seen to have slightly higher densities than their surroundings.

The porosity of the upper crustal materials was computed using the grain densities from Huang and Wieczorek (2012) and is plotted in Figure 27. The porosity in the lunar highland crust varies from about 3 to 24%, with an average of 13%, similar to the values obtained in Wieczorek et al. (2013). This map has several features in common with that of Figure 26. As examples, the density lows associated with the regions surrounding Orientale and Moscoviense basins are associated with enhanced porosities. Furthermore, the interiors of small basins with no mare fill correspond to porosity lows.

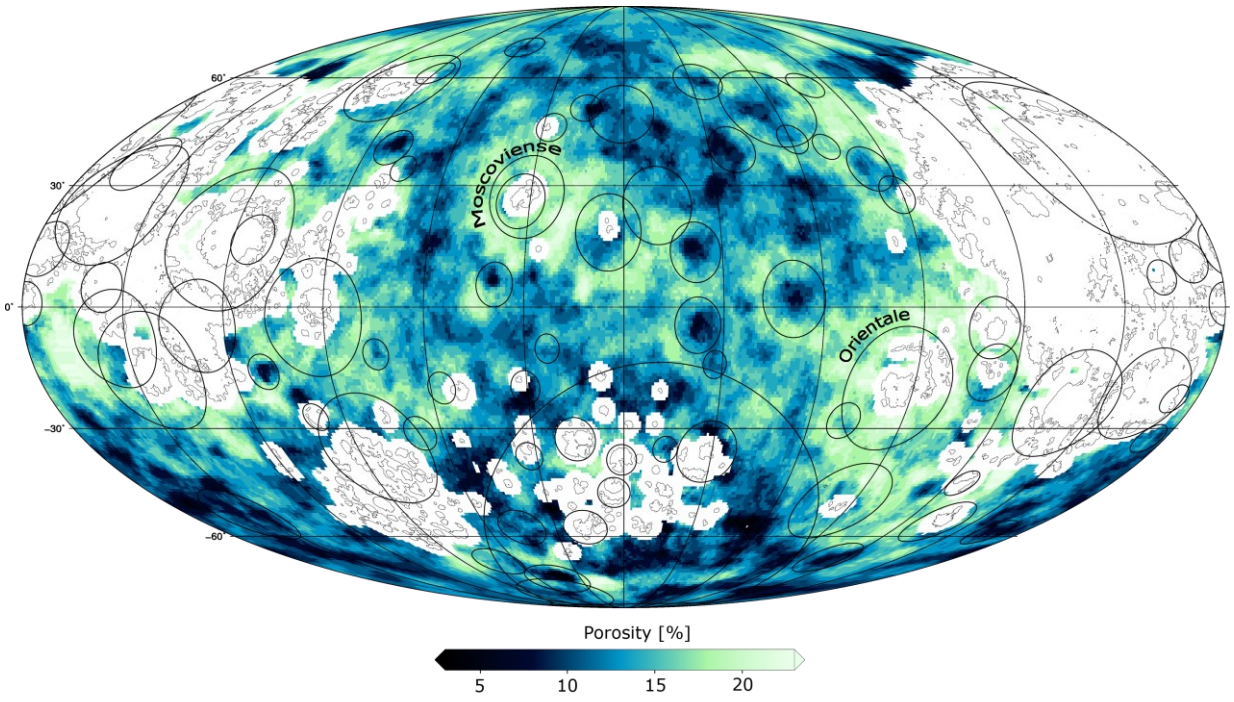

Figure 27: Lateral variations in porosity of the upper crust. Image format is the same as in Figure 26.

4.3.2 Porosity signatures of impact basins

We next analyzed the porosity signatures of individual impact basins, making use of the basin catalogue of Neumann et al. (2015). Several impact structures that are completely or largely covered by mare basalts were excluded from our investigation, given that their density structure is poorly constrained. These included many prominent basins on the nearside (such as Imbrium, Serentitatis, Crisium, Nectaris, and Humorum) as well as most of the basins located in the South Pole-Aitken (SPA) basin (such as Apollo). Some basins situated in the lunar highlands also show bulk density and porosity gaps due to the presence of mare basalts, but these gaps are mostly limited to the inner most portion of the basin and make up a very small portion of the data used in generating an azimuthally averaged radial porosity profile. In the end, we investigated 40 basins located in the lunar highlands with diameters greater than 200 km. For each basin, we created azimuthally averaged plots of porosity as a function of distance from the basin center, extending to 3 crater radii. For each point, we also computed the standard deviation, which is the measure of the natural variability of any given point with respect to the mean value. To aide in comparing the porosity profiles of the various basins, we normalized the radial distances by the main rim diameter of each basin.

While some basins show no clear pattern in their radial porosity profiles, others exhibit a distinct signature. In Figure 28 we investigate two representative basins, the large 571 km diameter Hertzsprung basin (left) and the highly degraded basin TOPO-22 (right). The upper image shows a shaded relief map of the basin, the middle panel shows our derived porosities in map form, and the lower image plots the azimuthally averaged porosity as a function of distance from the basin center. The main rim is marked as a solid, thick line at the distance of 1 crater radius, and the peak ring and inner depression (when present) are shown as dashed and dotted lines, respectively. Porosity profiles are normalized in distance by the main crater rim and the absolute distances from the basin center are shown on the upper axis.

For the Hertzsprung basin, the porosity signature is approximately concentric about the basin center. Regionally low porosities of 6% are found in the center of the basin, while just exterior to the main rim the porosity reaches its maximum value of about 15%. For this basin, the density contrast between the minimum and maximum values is 9% and we note that the lowest porosities are found interior to the peak ring, which has a diameter of about half of the main rim. Furthermore, this basin also possesses an inner depression that lies interior the peak ring, and the lowest porosities are closely correlated with the inner depression. In contrast, the slightly smaller, but highly degraded basin named TOPO-22 (Figure 28) shows a less distinctive and muted signature. The local minimum of 9% is found within the peak ring, and exterior to the main rim

the porosity is quite variable and affected by multiple younger impact structures. The maximum porosity corresponds to the regional value far from the basin rim of about 14%. Consequently, TOPO-22 only possesses a modest porosity contrast of at most 5%. The porosity contrast between the basin center and the main rim is substantially lower at about 3%.

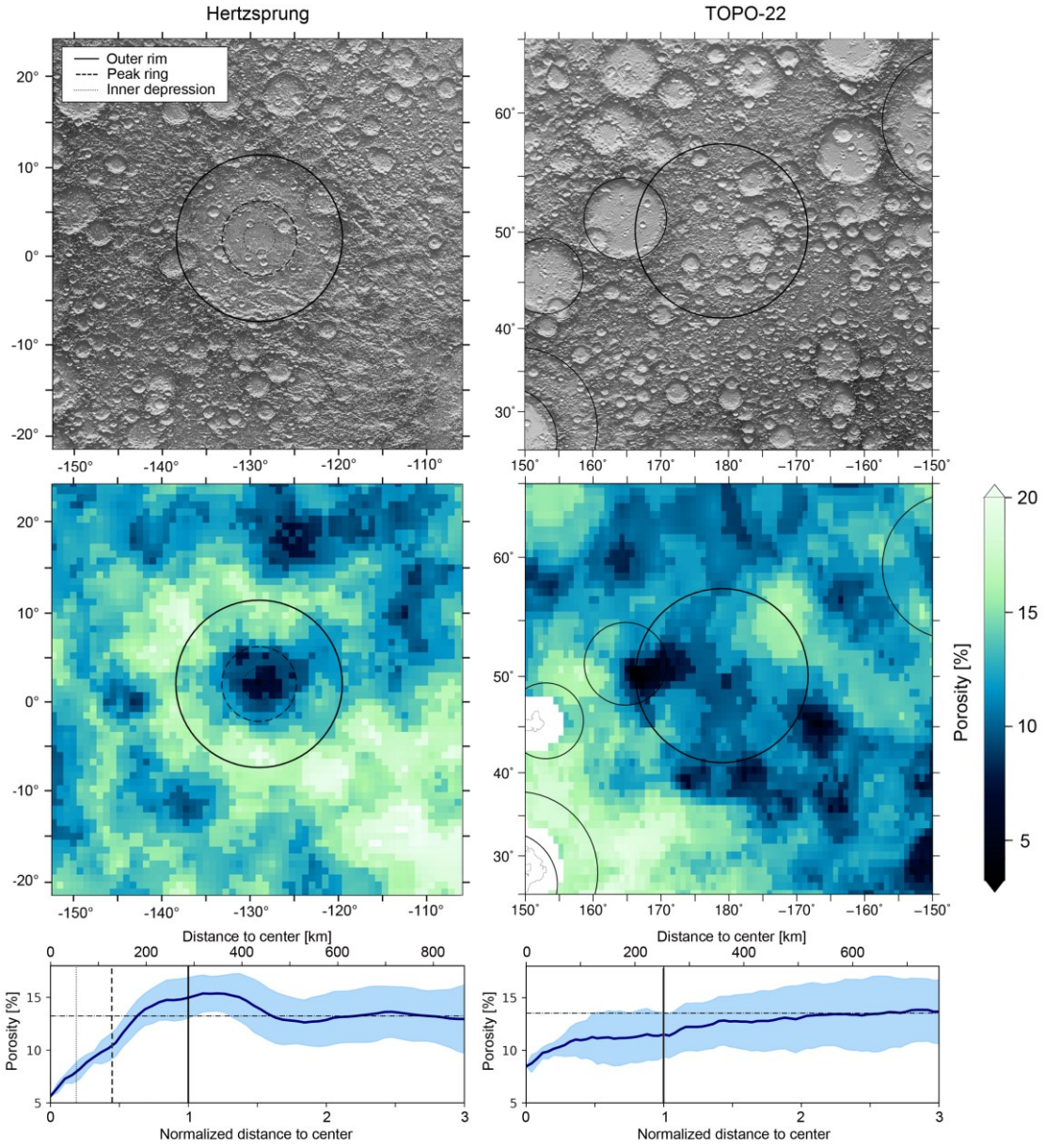

Figure 28: Porosity signatures of the Hertzsprung (left) and degraded TOPO-22 (right) impact basins. Plotted are (top) shaded relief maps, (middle) porosity maps, and (bottom) azimuthally averaged porosity profiles with associated standard deviations. In each image, basin ring diameters from Neumann et al. (2015) are plotted: main rim (solid), peak ring (dashed), and inner depression (dotted). Mare basalts (when present) are outlined in thin lines, and analysis regions that were excluded as a result of the mare basalts are plotted in white. Maps are show in a Mercator projection. The distances given on the lower axis of the porosity profile cross-sections are normalized to the main basin rim radius, and the upper axis provides absolute distances. The horizontal dash-dotted line denotes the ambient porosity, which is the average porosity between 2 and 3 radii distance from the basin center.

Azimuthally averaged porosity profiles of basins that have distinct porosity signatures are shown in Figure 29. A striking feature that can be observed for all basins presented in this figure is that the local minimum is always situated in the basin center inside the peak ring (if one exists). For many peak-ring and multiring basins, the porosity abruptly increases interior of the peak ring (such as Birkhoff), whereas for others, the porosity continually increases interior of the main rim (such as Dirichlet-Jackson). The majority of these basins also show higher porosities than the regional average, extending from the peak ring (at ~0.5 crater radii) to beyond the main crater rim at about 1.5 - 2 crater radii. In Figure 33 we show basins without any distinct porosity signature and in Figure 34 basins where porosity measurements in their interiors are lacking due to the presence of mare basalt.

The most striking basins in a global context (Figure 27) are Moscoviense and Orientale, which are two of the largest and also youngest basins located in the lunar highlands. Moscoviense is a 640 km diameter basin that is Nectarian in age, whereas Orientale is 937 km in diameter and one of the youngest basins with an Imbrian age. Both exhibit very high porosities in their surroundings as shown in Figure 30. Though the porosity could not be determined in the basin interior, as a result of the presence of mare basalts, extremely high porosities are found to extend out to almost 2 crater radii from the basin center. The porosity peaks for Moscoviense and Orientale at 20 and 22%, respectively, which are 8% greater than the ambient porosity.

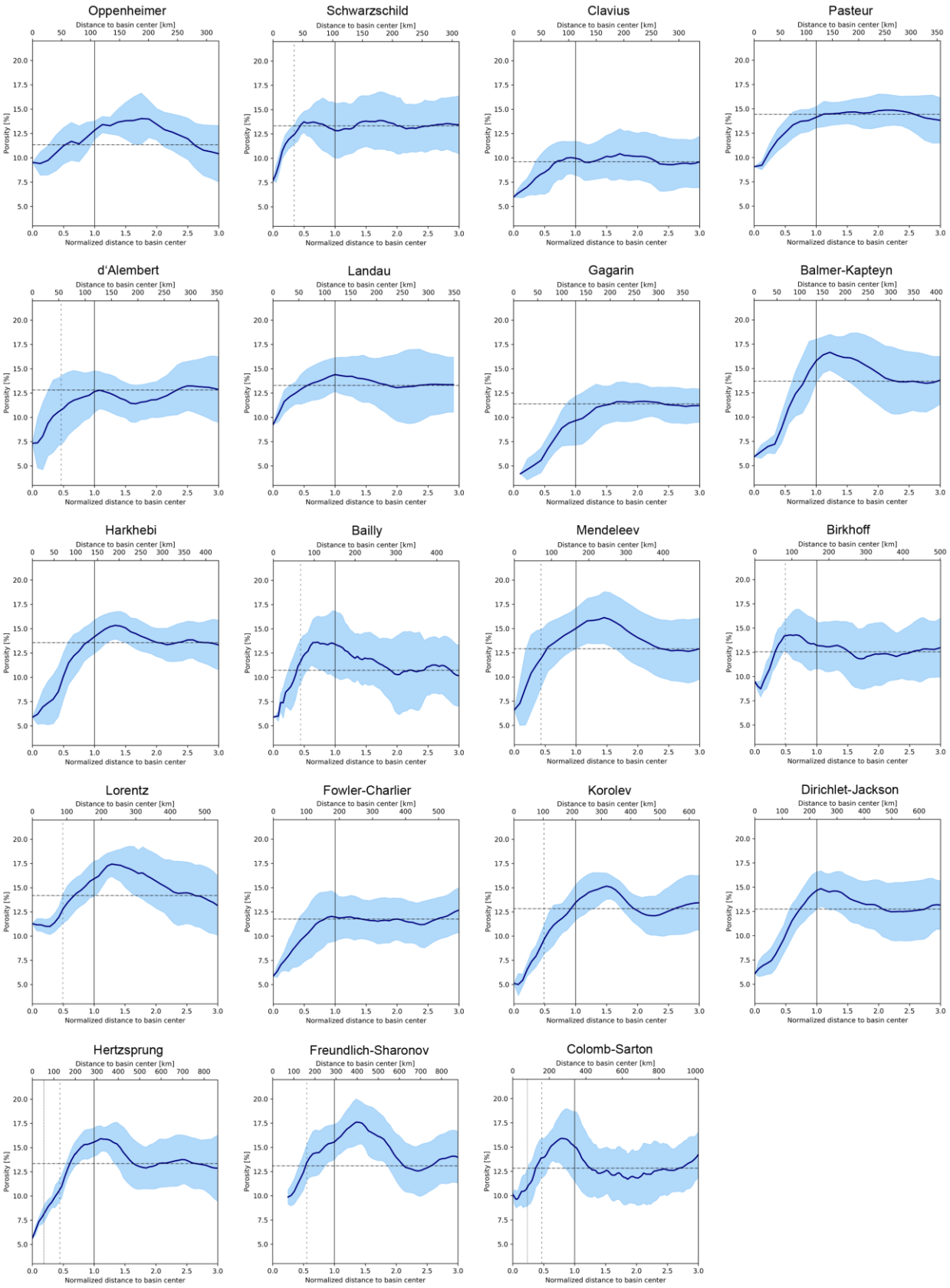

Figure 29: Azimuthally averaged porosity profiles of impact basins located in the lunar highlands that show a distinct porosity signature. Figure format is the same as in Figure 28.

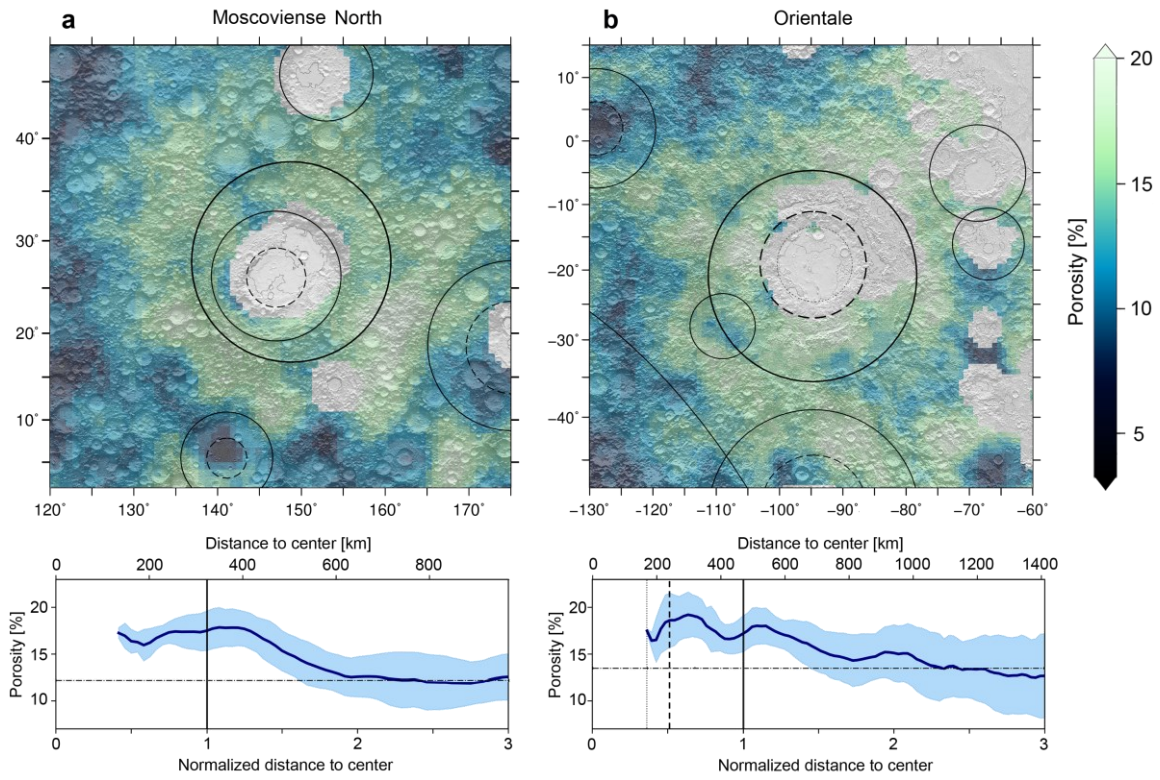

Figure 30: Porosity maps of (a) Moscoviense and (b) Orientale basin with shaded-relief LOLA topography in the background and azimuthally averaged profiles of porosity with their corresponding standard deviations (below). Maps are plotted in a Mercator projection. The image format is the same as in Figure 28.

In Table 2 we list the porosity characteristics of all basins that have been investigated in this study. For each basin we estimated the azimuthally averaged minimum porosity ϕ_{min}, the azimuthally averaged maximum porosity ϕ_{max}, and the porosity contrast ϕ_{diff}, which is defined as the difference between the maximum and minimum porosity. The ambient value of the crustal porosity is also provided, which represents an average between 2 and 3 main rim radii. Basins for which the minimum porosity could not be determined because of the presence of mare in their centers are enclosed by parentheses. The South Pole-Aitken (SPA) basin is not included in the list, since meaningful values cannot be determined, as a result of the huge dimension of the basin and the presence of numerous superposed younger basins. Instead, in the Appendix we provide a detailed map of the South Pole-Aitken basin porosity together with an azimuthally averaged porosity profile (Figure 35). As shown in the table, the minimum porosities vary from 4 to 16%, the maximum porosity ranges from 10 to 19%, and the ambient porosities vary between 10 and 16%. The porosity contrasts vary from 1 to 11%.

Table 2: Porosity characteristics of investigated lunar basins.

Basin name	Diameter [a] [km]	Min. porosity within basin [%]	Standard deviation [%]	Max. porosity [%]	Standard deviation [%]	Porosity contrast [%]	Standard deviation [%]	Ambient porosity [%]
Wegener-Winlock	205	15.5	0.4	16.7	0.0	1.3	0.4	14.2
Humboldt	206	(11.6)	1.4	13.9	2.7	(2.4)	4.1	13.3
Oppenheimer	206	(9.4)	1.2	14.0	2.6	(4.6)	3.8	11.3
Schwarzschild	207	7.7	0.0	13.9	3.0	6.2	3.0	13.3
Galois	210	9.6	0.0	14.0	1.1	4.4	1.6	13.1
Keeler West	218	11.1	0.0	12.5	1.6	1.4	1.6	11.2
Clavius	220	6.0	0.0	10.4	2.6	4.5	2.6	9.6
Deslandres	220	10.5	1.1	11.8	0.9	1.3	2.1	10.2
TOPO-13	220	(9.3)	0.0	13.3	1.6	(3.9)	1.7	10.6
Poczobutt	225	15.0	0.6	17.8	1.6	2.7	2.3	14.1
Pasteur	231	9.1	0.0	14.9	1.6	5.8	1.7	14.8
d'Alembert	232	7.3	0.0	13.2	2.5	5.9	2.5	12.8
Landau	236	9.2	0.0	14.4	1.7	5.2	1.7	13.3
Campbell	237	(14.0)	0.3	15.4	1.4	(1.4)	1.7	14.1
Fermi	241	(14.2)	0.6	15.6	1.3	(1.4)	1.8	13.4
Gagarin	256	(4.2)	0.0	11.7	1.7	(7.4)	1.7	11.4
Milne	264	14.2	1.4	14.8	0.5	0.6	1.9	12.5
Balmer-Kapteyn	265	5.9	0.0	16.7	1.8	10.7	1.8	13.8
Orientale-Southwest	276	14.5	0.6	17.5	1.0	3.0	1.5	16.4
Harkhebi	280	5.9	0.0	15.3	1.4	9.4	1.9	13.1
Bailly	299	5.9	0.0	13.6	2.7	7.7	2.7	10.8
Planck	321	9.7	1.5	12.0	2.7	2.3	4.2	11.7
Mendeleev	331	6.6	0.0	16.1	2.7	9.6	3.0	12.7
Birkhoff	334	8.7	0.8	14.3	2.7	5.6	3.5	12.6
Ingenii	342	10.9	2.2	14.1	2.6	3.2	4.9	10.4
Lorentz	351	(11.0)	0.8	17.4	1.3	(6.4)	2.8	14.3
Schiller-Zucchius	361	(13.5)	2.4	15.0	2.1	(1.5)	4.5	10.9
Fowler-Charlier	374	5.9	0.0	12.7	2.3	6.8	2.3	11.7
Korolev	417	5.0	1.1	15.2	1.4	10.2	1.9	12.8
Moscovience	421	(15.6)	2.1	17.7	1.8	(2.1)	3.9	14.5
Mutus-Vlacq	450	8.0	1.0	13.4	3.2	5.4	4.1	12.4
Dirichlet-Jackson	452	6.1	0.0	14.9	1.8	8.8	1.8	12.7
TOPO-22	500	8.5	0.0	13.8	3.0	5.4	3.0	13.5
Hertzsprung	571	5.6	0.0	15.9	1.3	10.3	1.7	13.2
Freundlich-Sharonov	582	(9.9)	0.7	17.6	2.4	(7.7)	3.3	12.9
Fitzgerald-Jackson	600	12.0	0.0	14.2	2.5	2.2	2.5	13.4
Moscoviense North	640	(16.0)	1.7	17.9	2.1	(1.9)	3.8	12.2
Mendel-Rydberg	650	(13.8)	2.2	16.5	2.5	(2.8)	4.7	13.4
Coulomb-Sarton	672	9.6	0.9	15.9	2.8	6.3	3.6	12.9
Orientale	937	(16.4)	0.9	19.2	2.4	(2.8)	3.3	13.5

Numbers in parentheses lack data in the basin centers as a result of the presence of mare basalts. Basin names are approved by the International Astronomical Union (IAU) or suggested by Neumann et al. (2015). The ambient porosity is the average porosity between 2 and 3 main rim radii from the basin center.

[a] Data from Neumann et al. (2015).

4.4 Discussion

4.4.1 Porosity characteristics of impact basins

Many lunar impact basins show marked crustal porosity anomalies that stand out against the global background (Figure 27). These basins all possess a similar signature where the porosity is reduced within the peak ring and the porosity is highest close to and just exterior to the main rim. Other basins have less well characterized profiles, and the most likely explanation for this is that the initial porosity signature was modified by subsequent impact events. We thus suggest that basins form with an initially well defined and characteristic porosity profile, and that as the crater degrades, the profile becomes more muted and less distinct.

In Figure 28 we show the porosity map and profile of Hertzsprung basin (left), which is representative of an unmodified basin that possesses a clear and distinct porosity pattern. In its center a pronounced porosity low can be found. The porosity is reduced to 5% within a radius of 0.6 crater radii compared to the regional value of 13%. This porosity low is confined largely within the peak ring. From about 0.6 to 1.6 crater radii the porosity is higher than the background value and achieves a maximum value of 16% just beyond the main basin rim at 1.2 crater radii. The maximum porosity of 16% is larger than the background value by 3%. Most basins with clear signatures have similar patterns, though the exact crater radii at the various transitions can vary by about half a crater radius.

The reduced porosity within the basin center is probably the result of several factors. One important contribution is likely the production of impact melt. Impact melt sheets, if sufficiently thick, should form with porosities near zero. As suggested by numerical simulations, the volume of melt is mainly related to the dimension of the projectile (Grieve and Cintala, 1992; Pierazzo et al., 1997), but is also dependent on other factors such as the composition and initial temperature of the target material (Pierazzo et al., 1997), and the impact angle (Pierazzo and Melosh, 2000). Cintala and Grieve (1998) proposed a scaling law for estimating the volume of impact melt V_M under terrestrial and lunar conditions as a function of transient crater diameter D_{tc} in the general form

$$V_M = c\, D_{tc}^{d} \tag{15}$$

where the constants c and d depend on the impactor velocity and composition. Applying values for a chondritic projectile with an impact velocity of 15 km s^{-1} and assuming a linear relationship between the diameter of the transient and the final crater, a basin with the dimension of Hertzsprung (D = 571 km) would have about 60 times more impact melt than a basin with a

diameter of only 200 km. Another crucial parameter controlling the amount of generated melt is the initial porosity of the target material before impact. Numerical simulations by Wünnemann et al. (2008) showed that materials with high initial porosity significantly reduce the critical pressure that is required for melting. Consequently, more melt is generated in target materials of high porosity. Vaughan et al. (2013) modeled impact melt production using the example of Orientale basin. The thickest melt sheet (about 14 km) was found to be located in the basin center, with an extent of approximately 0.7 crater radii. This is about the same size as the peak ring and fits well with the extent of the observed porosity minimum of the basins that do not possess younger mare basalts.

As suggested by numerical models, another factor being responsible for the reduced porosity in a basin's interior could be the compaction of the target material, which is the closing of preexisting pore space (e.g., Wünnemann et al., 2006; Collins et al., 2011). In highly porous targets the effect of compaction plays a fundamental role on the postimpact porosity (Housen and Holsapple, 2003). In particular, numerical simulations by Milbury et al. (2015) showed that preimpact porosities of greater than 7% result in positive Bouguer anomalies (indicating reduced porosities).

The increased porosities that are found near to the crater rim are likely the result of several factors, as well. First, during crater formation, target material gets displaced and deformed. Materials that are ballistically excavated reimpact the surface outside of the transient cavity and form an ejecta blanket, which can be of several tens kilometer thick. The ejecta deposits are generally continuous about 1 crater radii away from the rim, beyond which the deposits become discontinuous and thin. The ejecta deposits are expected to have extremely high porosities as a result of the excavation and reimpact processes. Second, as a result of the passing shock wave and the subsequent sheardominated cratering flow, fracturing and brecciation raise the porosity of the target material (Pilkington and Grieve, 1992; Collins et al., 2004). Dilatancy, which is the increase in volume of a rock while subject to shear deformation, would also contribute to raise the porosity (Collins, 2014). Numerical simulations by Wiggins et al. (2019) showed that the impact of projectiles with sizes of 1 to 10 km (which create craters with diameters of about 10 to 100 km) would create significant fracturing to depths of at least 20 km. Since the porosities estimated in our study represent an average of the upper several kilometers of the lunar crust, we emphasize that it is not possible to distinguish between deep porosity caused by fracturing of the in situ crust by shock waves or by the overlying ejecta blanket that represents ballistically excavated materials.

4.4.2 Porosity structure in relation to basin dimension and age

The majority of the investigated basins in our study have younger impact basins in their vicinity. These later superposed craters and basins likely interfered with the previously existing porosity structure, leading to substantial lateral variability in the porosity of the superposed impact basin. Of the 40 basins that were investigated, only 27 were likely not disturbed by later large scale impact events (see Figure 29 and Figure 33). The characteristics of these relatively pristine basins are investigated further in Figure 31, where we plot both the minimum and maximum porosity as a function of basin diameter. Those basins that lack density estimates in their interiors as a result of mare basalts are plotted in red.

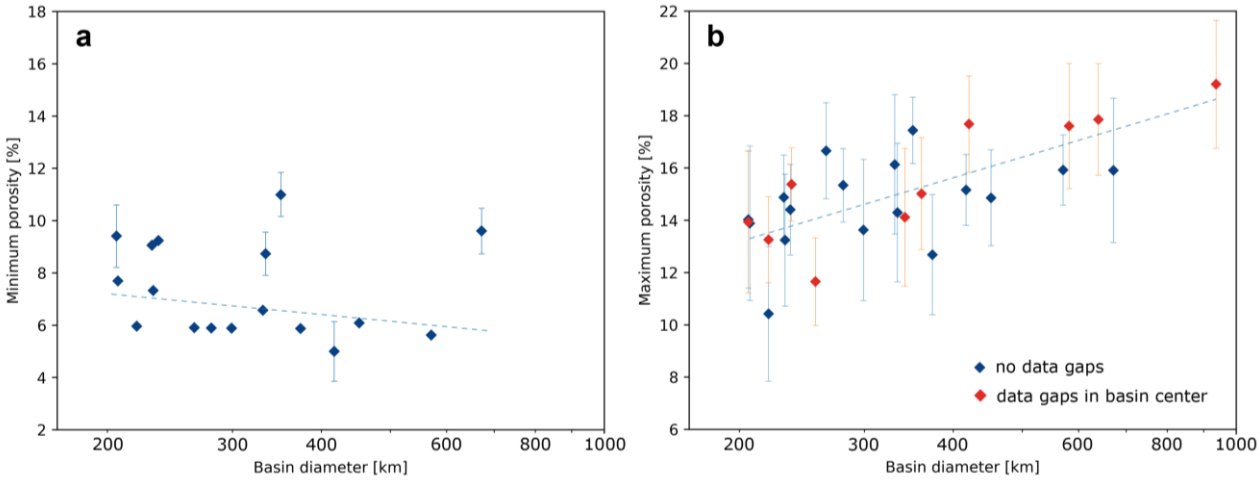

Figure 31: (a) Minimum porosity ϕ_{min} and (b) maximum porosity ϕ_{max} as a function of the main rim diameter (Neumann et al., 2015) for selected pristine basins. Basins, which lack data in their center due to of presence of mare basalt are marked in red and were excluded when estimating the trendline for the minimum porosity.

We first find that the maximum porosity increases with increasing basin diameter, from values close to 13% at 200 km diameter to 18% at 900 km diameter. We explain the increased porosities for larger basins by more material being excavated as the basin increases in size, leading to thicker ejecta blankets of highly porous and fractured material outside the transient crater. Since for larger basins a larger extent of the isobaric core (Pierazzo et al., 1997) is expected (within this region, the peak shock pressure reaches it maximum value), the fracture zone for larger basins should be shifted further outwards. In the left panel of Figure 31 we plot the minimum porosity as a function of crater diameter. For this measure, the basins with data gaps in their center should be considered unreliable, given that the lowest porosities are found generally in the basin center. When excluding those basins, we find that the minimum porosity only slightly decreases with increasing basin size, from about 7% at 200 km diameter to 6% at 600 km

diameter. This small effect could be related to the larger quantities and depths of impact melt that are generated by larger basins.

We next investigated how the porosity structure of individual basins varies with respect to their ages (Figure 32). Though some of the basins in our study have well known relative and/or absolute ages, the formation time of many basins are unknown. For the relative ages, we made use of the sequences published in Spudis et al. (2011) and Orgel et al. (2018). For the most part, these are consistent with previous work by Wilhelms (1987). If a relative basin age could not be found, we removed it from the consideration in our analysis.

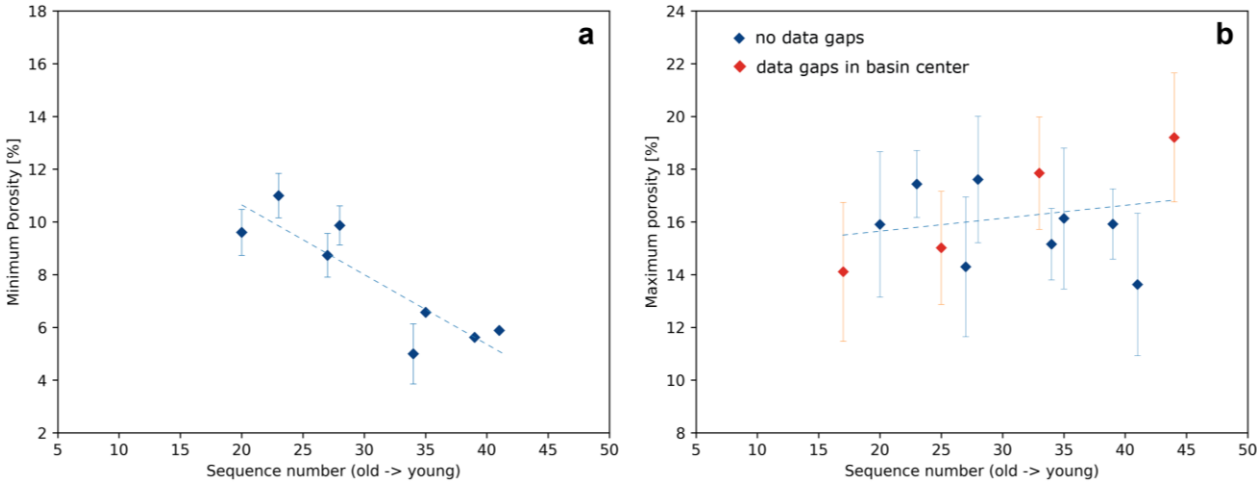

Figure 32: (a) Minimum porosity ϕ_{min} and (b) maximum porosity ϕ_{max} as a function of basin formation sequence (Spudis et al., 2011; Orgel et al., 2018). Basins that lack data in their center due to of presence of mare basalt are marked in red and were excluded when estimating the trendline for the minimum porosity. Basins with unknown relative or absolute ages were omitted from the analysis.

In Figure 32, we plot both the minimum and maximum porosities of the pristine basins as a function of relative age, where the ages decrease with increasing sequence number. We first find that the minimum porosity in the basin center is smallest for the youngest basins (about 5%), having a model age of about 3.81 Ga, and largest for the oldest basins (about 11%) with an approximate model age of 4.28 Ga (Orgel et al., 2018). We attribute this behavior to older basins being subjected to numerous smaller impact events (m to km scale), which progressively fractures the impact melt sheet with increasing time. For the oldest basins, the minimum porosity is not too different from the background value far from the basin center. For the maximum porosity shown in the right panel, a slight increase in maximum porosity with decreasing age is observed, from about 15% for the oldest basins to about 16% for the youngest.

4.5 Summary

High resolution gravity data from recent gravity models of the Moon have allowed us to estimate the bulk density and porosity of the upper lunar crust. The spatial resolution of our bulk density estimates are about a factor of two better than previous studies that used lower resolution gravity data, and this allowed us to investigate the porosity structure of lunar impact basins. We find that the upper crust exhibits a wide range of porosities, with values between 3 and 24%. Our global high-resolution porosity map provides clear evidence that large impact basins both increase and reduce porosity. Many basins show a distinct porosity signature, with low porosities in their center within the peak ring (if one exists), and increased porosities close to and just exterior to the main rim. Other basins show a less distinctive and muted porosity pattern, which are attributed to postimpact modification by superposed large basins and craters. We suggest that after formation all basins show pronounced porosity signature, and that basins that have been exposed to subsequent large scale impact events show a modified and more muted porosity pattern. The larger the impact basin, the more pronounced are the minimum and maximum porosities. Furthermore, we demonstrate a correlation between the porosity structure of impact basins and their relative ages. While older candidates show a less pronounced porosity signature with a lower porosity contrast, younger basins show the highest porosities near their rims and the lowest values interior to the peak ring. We relate the lower contrast for older candidates to modifications through later impacts. The results of the present work will help constrain models of impact crater formation that consider both fracturing and compaction of the crust.

Acknowledgements

Daniel Wahl was supported by the Deutsche Forschungsgemeinschaft (DFG) grant SFB TRR 170, subproject A04-83. Mark A. Wieczorek was partially supported by a grant from the French space agency (CNES). We gratefully acknowledge Jason Soderblom and an anonymous reviewer for their helpful comments improving the manuscript. The GRAIL gravity model GL1500E as well as topography data LOLA2600p can be accessed online via the NASA Planetary Data System (https://pds.nasa.gov/). All data to reproduce the results and figures in this work can be accessed online (http://dx.doi.org /10.17632/jmd84c6f64.1).

References

Besserer, J., Nimmo, F., Wieczorek, M.A., Weber, R.C., Kiefer, W.S., McGovern, P.J., Andrews-Hanna, J.C., Smith, D.E. and Zuber, M.T. (2014). GRAIL gravity constraints on the vertical and lateral density structure of the lunar crust. Geophysical Research Letters, 41 (16), 5771-5777, doi: 10.1002/2014GL060240.

Cintala, M.J. and Grieve, R.A.F. (1998). Scaling impact melting and crater dimensions: Implications for the lunar cratering record. Meteoritics and Planetary Science, 33 (4), 889-912, doi: 10.1111/j.1945-5100.1998.tb01695.x.

Collins, G.S. (2014). Numerical simulations of impact crater formation with dilatancy. Journal of Geophysical Research: Planets, 119 (12), 2600-2619, doi: 10.1002/2014JE004708.

Collins, G.S., Melosh, H.J. and Ivanov, B.A. (2004). Modeling damage and deformation in impact simulations. Meteoritics and Planetary Science, 39 (2), 217-231, doi: 10.1111/j.1945-5100.2004.tb00337.x.

Collins, G.S., Melosh, H.J. and Wünnemann, K. (2011). Improvements to the e-a Porous compaction model for simulating impacts into high-porosity solar system objects. International Journal of Impact Engineering, 38 (6), 434-439, doi: 0.1016/j.ijimpeng.2010.10.013.

Crameri, F. (2018) Scientific colour-maps. Zendo, doi: 10.5281/zendo.1243862.

Förstner, U. (1967). Petrographische Untersuchungen des Suevit aus den Bohrungen Deiningen und Wörnitzostheim im Ries von Nördlingen. Contributions to Mineralogy and Petrology, 15 (4), 281-308, doi: 10.1007/BF00404198.

Gong, S., Wieczorek, M.A., Nimmo, F., Kiefer, W.S., Head, J.W., Huang, C., Smith, D.E. and Zuber, M.T. (2016). Thicknesses of mare basalts on the Moon from gravity and topography. Journal of Geophysical Research: Planets, 121 (5), 854-870, doi: 10.1002/2016JE005008.

Grieve, R.A.F. and Cintala, M.J. (1992). An analysis of differential impact melt crater scaling and implications for the terrestrial impact record. Meteoritics, 27 (5), 526-538, doi: 10.1111/j.1945-5100.1992.tb01074.x.

Housen, K.R. and Holsapple, K.A. (2003). Impact cratering on porous asteroids. Icarus, 163 (1), 102-119, doi: 10.1016/S0019-1035(03)00024-1.

Huang, Q. and Wieczorek, M.A. (2012). Density and porosity of the lunar crust from gravity and topography. Journal of Geophysical Research: Planets, 117 (5), 1-9, doi: 10.1029/2012JE004062.

Kiefer, W.S., MacKe, R.J., Britt, D.T., Irving, A.J. and Consolmagno, G.J. (2012). The density and porosity of lunar rocks. Geophysical Research Letters, 39 (7), 1-5, doi: 10.1029/2012GL051319.

Konopliv, A.S., Park, R.S., Yuan, D.-N., Asmar, S.W., Watkins, M.M., Williams, J.G., Fahnestock, E., Kruizinga, G., Paik, M., Strekalov, D., Harvey, N., Smith, D.E. and Zuber, M.T. (2014). High-resolution lunar gravity fields from the GRAIL Primary and Extended Missions. Geophysical Research Letters, 41 (5), 1452-1458, doi: 10.1002/2013GL059066.

Lemoine, F.G., Goossens, S., Sabaka, T.J., Nicholas, J.B., Mazarico, E., Rowlands, D.D., Loomis, B.D., Chinn, D.S., Neumann, G.A., Smith, D.E. and Zuber, M.T. (2014). GRGM900C: A degree 900 lunar gravity model from GRAIL primary and extended mission data. Geophysical Research Letters, 41 (10), 3382-3389, doi: 10.1002/2014GL060027.

Love, S.G., Horz, F. and Brownlee, D.E. (1993). Target porosity effects in impact cratering. Icarus, 105, 216-224, doi: 10.1006/icar.1993.1119.

Melosh, H.J., Freed, A.M., Johnson, B.C., Blair, D.M., Solomon, S.C., Wieczorek, M.A. and Zuber, M.T. (2013). The origin of lunar mascon basins. Science, 340, 1552-1556, doi: 10.1126/science.1235768.

Milbury, C., Johnson, B.C., Melosh, H.J., Collins, G.S., Blair, D.M., Soderblom, J.M., Nimmo, F., Bierson, C.J., Phillips, R.J. and Zuber, M.T. (2015). Preimpact porosity controls the gravity signature of lunar craters. Geophysical Research Letters, 42 (22), 9711-9716, doi: 10.1002/2015GL066198.

NASA. (2008). A Standardized Lunar Coordinate System for the Lunar Reconnaissance Orbiter and Lunar Datasets. LRO Project LGCWG White Paper, 5, pp. 13.

Nelson, D.M., Koeber, S.D., Daud, K., Robinson, M.S., Watters, T., Banks, M., Williams, N.R. (2014). Mapping Lunar Maria Extents and Lobate Scarps Using LROC Image Products. LPSC Abtract #2861.

Neumann, G.A., Zuber, M.T., Wieczorek, M.A., Head, J.W., Baker, D.M.H., Solomon, S.C., Smith, D.E., Lemoine, F.G., Mazarico, E., Sabaka, T.J., Goossens, S.J., Melosh, H.J., Phillips, R.J., Asmar, S.W., Konopliv, A.S., Williams, J.G., Sori, M.M., Soderblom, J.M., Miljković, K., Andrews-Hanna, J.C., Nimmo, F. and Kiefer, W.S. (2015). Lunar impact basins revealed by Gravity Recovery and Interior Laboratory measurements. Science Advances, 1(9), e1500852-e1500852, doi: 10.1126/sciadv.1500852.

Orgel, C., Michael, G., Fassett, C.I., van der Bogert, C.H., Riedel, C., Kneissl, T., Hiesinger, H. (2018). Ancient Bombardment of the Inner Solar System: Reinvestigation of the “Fingerprints" of Different Impactor Populations on the Lunar Surface. Journal of Geophysical Research: Planets, 123 (3), 748-762, doi: 10.1002/2017JE005451.

Park, R.S., Konopliv, A.S., Yuan, D.-N., Asmar, S., Watkins, M.M., Williams, J., Smith, D.E. and Zuber, M.T. (2015). A high-resolution spherical harmonic degree 1500 lunar gravity field from the GRAIL mission. AGU Fall-Meeting, Abstract #G41B-01.

Pierazzo, E. and Melosh, H.J. (2000). Melt Production in Oblique Impacts. Icarus, 145 (1), 252-261, doi: 10.1006/icar.1999.6332.

Pierazzo, E., Vickery, A.M. and Melosh, H.J. (1997). A Reevaluation of Impact Melt Production. Icarus, 127, 408-423, doi: 10.1006/icar.1997.5713.

Pilkington, M. and Grieve, R.A.F. (1992). The Geophysical Siganture of Terrestrial Impact Craters (1992).pdf. Reviews of Geophysic, 30, 161-181, doi: 10.1029/92RG00192.

Pohl, J., Stöffer, D., Gall, H. and Ernstson, K. (1977). The Ries impact crater. In D.J. Roddy, R.O. Pepin, and R.B. Merrill (Eds.), Impact and explosion cratering. New York: Pergamon Press, pp. 343-404.

Rae, A.S.P., Collins, G.S., Morgan, J.V., Salge, T., Christeson, G.L., Leung, J., Gulick, S.P.S., Poelchau, M., Riller, U., Gebhardt, C., Grieve, R.A.F., Osinski, G.R. (2019). Impact-Induced Porosity and Microfracturing at the Chicxulub Impact Structure. Journal of Geophysical Research: Planets, 124, 1960-1978, doi: 10.1029/2019je005929.

Smith, D.E., Zuber, M.T., Neumann, G.A., Mazarico, E., Lemoine, F.G., Head, J.W., Lucey, P.G., Aharonson, O., Robinson, M.S., Sun, X., Torrence, M., Barker, M.K., Oberst, J., Duxbury, T.C., Mao, D., Barnouin, O.S., Jha, K., Rowlands, D.D., Goossens, S., Baker, D., Bauer, S., Gläser, P., Lemelin, M., Rosenburg, M., Sori, M.M., Whitten, J. and Mcclanahan, T. (2017). Summary of the results from the lunar orbiter laser altimeter after seven years in lunar orbit. Icarus, 283, 70-91, doi: 10.1016/j.icarus.2016.06.006.

Soderblom, J.M., Evans, A.J., Johnson, B.C., Melosh, H.J., Miljkovi, K., Phillips, R.J., Andrews-Hanna, J.C., Bierson, C.J., Iii, J. W.H., Milbury, C., Neumann, G.A., Nimmo, F., Smith, D.E., Solomon, S.C. and Sori, M.M. (2015). The fractured Moon: Production and saturation of porosity in the lunar highlands from impact cratering. Journal of Geophysical Research: Planets, 42 (17), 6939-6944, doi: 10.1002/2015GL065022.

Spudis, P.D., Wilhelms, D.E. and Robinson, M.S. (2011). The Sculptured Hills of the Taurus Highlands: Impli-cations for the relative age of Serenitatis, basin chronologies and the cratering history of the Moon, Journal of Geophysical Research: Planets, 116 (12), 1-9. doi: 10.1029/2011JE003903.

Vaughan, W.M., Head, J.W., Wilson, L. and Hess, P.C. (2013). Geology and petrology of enormous volumes of impact melt on the Moon: A case study of the Orientale basin impact melt sea. Icarus, 223 (2), 749-765, doi: 10.1016/j.icarus.2013.01.017.

Wahl, D. and Oberst, J. (2019). Lateral variations in bulk density and porosity of the upper lunar crust from high-resolution gravity and topography data: comparision of different analysis tech-niques. ISPRS Annals of the Photo-grammetry, Remote Sensing and Spatial Information Sci., 4, 527-532, doi: 10.5194/isprs-annals-IV-2-W5-527-2019.

Warren, P.H. (2001). Porosities of lunar meteorites: Strength, porosity, and petrologic screening during the meteorite delivery process. Journal of Geophysical Research: Planets, 106 (E5), 10101-10111, doi: 10.1029/2000JE001283.

Wieczorek, M.A. (2015). Gravity and topography of the terrestrial planets. In G. Schubert and T. Spohn (Eds.), Treatise on geophysics 2nd edition, Vol. 10, Planets and Moons (Ed. T. Spohn), Elsevier. 153-193, doi: 10.1016/B978-0-444-53802-4.00169-X.

Wieczorek, M.A. and Meschede, M. (2018). SHTools: Tools for Working with Spherical Harmonics. Geochemistry, Geophysics, Geosystems, 19 (8), 2574-2592, doi: 10.1029/2018GC007529.

Wieczorek, M.A., Neumann, G.A., Nimmo, F., Kiefer, W.S., Taylor, J.G., Melosh, H.J., Phillips, R.J., Solomon, S.C., Andrews-Hanna, J.C., Asmar, S.W., Konopliv, A.S., Lemoine, F.G., Smith, D.E., Watkins, M.M., Williams, J.G. and Zuber, M.T. (2013). The Crust of the Moon as Seen by GRAIL. Science, 339, 671-675, doi: 10.1126/science.1231530.

Wieczorek, M.A. and Phillips, R.J. (1998). Potential anomalies on a sphere: Applications to the thickness of the lunar crust. Journal of Geophysical Research: Planets, 103 (97), 1715-1724, doi: 10.1029/97JE03136.

Wiggins, S.E., Johnson, B.C., Bowling, T.J., Melosh, H.J. and Silber, E.A. (2019). Impact Fragmentation and the Development of the Deep Lunar Megaregolith. Journal of Geophysical Research: Planets, 124 (4), 941-957, doi: 10.1029/2018JE005757.

Wilhelms, D. (1987). The geologic history of the moon. ISGS Numbered Series, No. 1348. doi: 10.3133/pp1348.

Wünnemann, K., Collins, G.S. and Melosh, H.J. (2006). A strain-based porosity model for use in hydrocode simulations of impacts and implications for transient crater growth in porous targets. Icarus, 180 (2), 514-527, doi: 10.1016/j.icarus.2005.10.013.

Wünnemann, K., Collins, G.S. and Osinski, G.R. (2008). Numerical modelling of impact melt production in porous rocks. Earth and Planetary Science Letters, 269, 530-539, doi: 10.1016/j.epsl.2008.03.007.

Zuber, M.T., Smith, D.E., Watkins, M.M., Asmar, S.W., Konopliv, A.S., Lemoine, F.G., Melosh, H.J., Neumann, G.A., Phillips, R.J., Solomon, S.C., Wieczorek, M.A., Williams, J.G., Goossens, S.J., Kruizinga, G., Mazarico, E., Park, R.S. Yuan, D.-N. (2013). Gravity Field of the Moon from the Gravity Recovery and Interior Laboratory (GRAIL) Mission. Science, 339, 2011-2014, doi: 10.1126/science.1231507.

Supplemental information

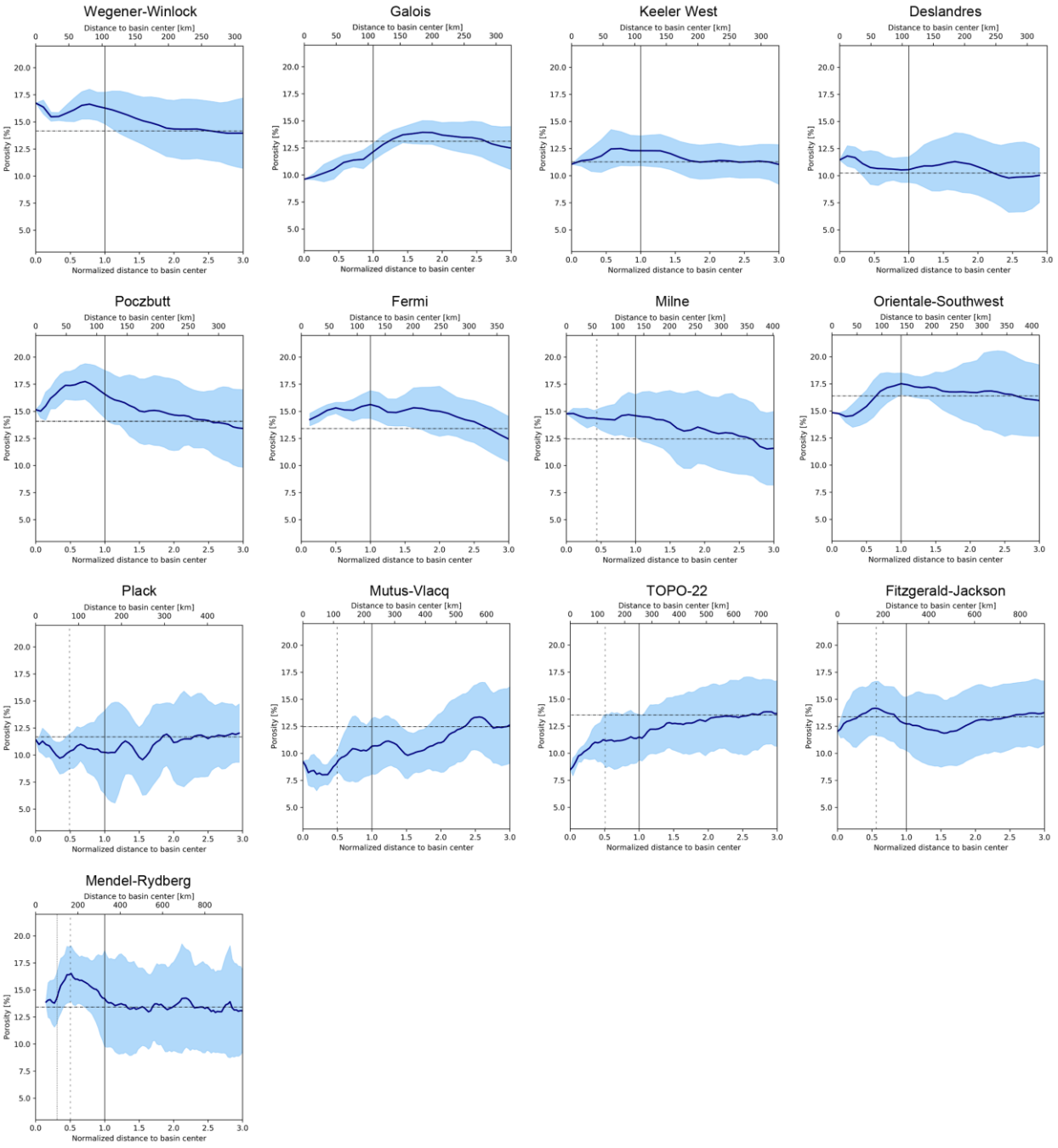

Figure 33: Azimuthally averaged radial porosity profiles with associated standard deviations for impact basins located in the lunar highlands that show an unpronounced porosity signature. The distances given on the lower axes are normalized to the main rim radius, and the upper axes provide absolute distances. Basin ring diameters from Neumann et al. (2015) are plotted: main rim (solid), peak ring (dashed), and inner depression (dotted). The horizontal dash-dotted line denotes the ambient porosity, which is the average porosity between 2 and 3 main rim radii from the basin center.

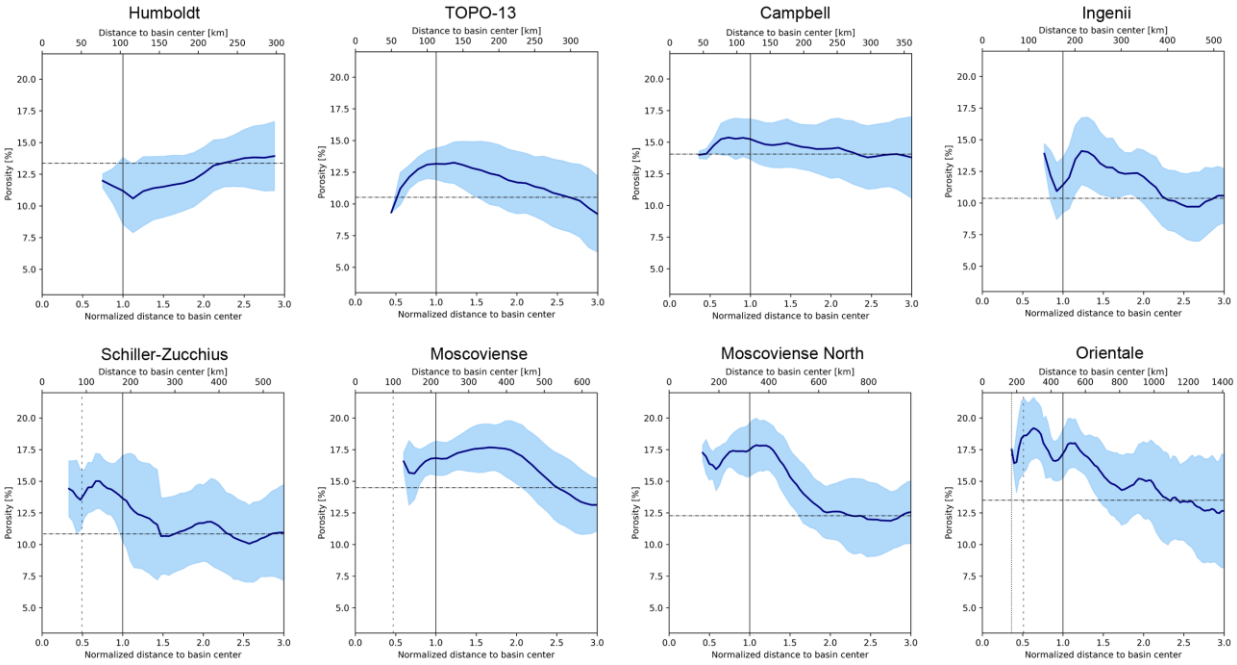

Figure 34: Azimuthally averaged radial profiles of porosity with their related standard deviations for impact basins located in the lunar highlands, having data gaps in their centers because of mare occurrences. Labels as in Figure 33.

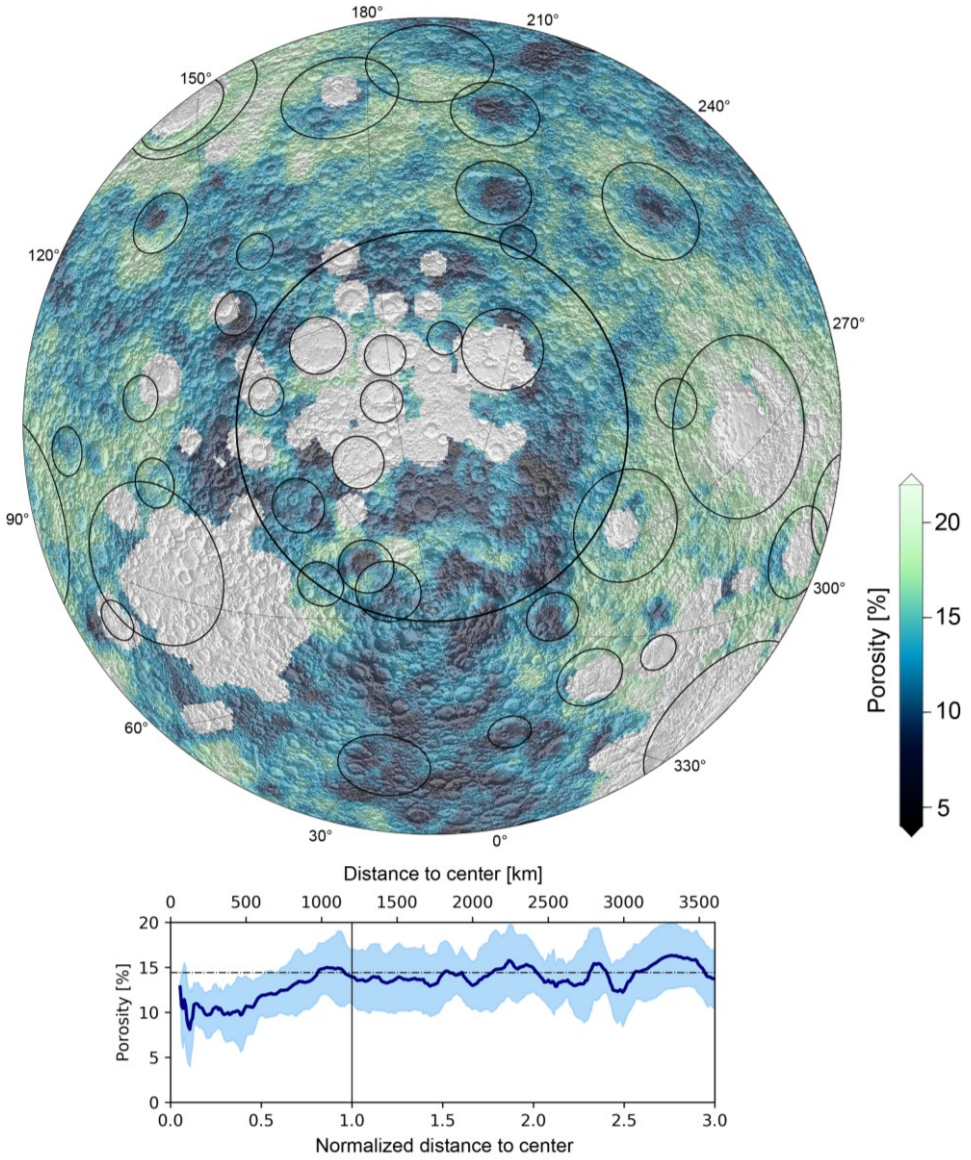

Figure 35: Porosity map of South Pole-Aitken (SPA) basin with superposed LOLA shaded relief map, presented in a Lambert azimuthal equal area projection. Below, the azimuthally averaged porosity profile for the basin is shown. Labels in the profile are similar to those in Figure 33 .

5. Discussion and Outlook

Compared to earlier models, the accuracy and spatial resolution of the latest GRAIL gravity field, represented as a spherical harmonic function model developed to degree and order 1500, significantly improved, allowing to revisit the geophysical properties of the upper crust of the Moon. Using gravity in combination with topography derived from LOLA data, lateral variations in bulk density of the highland crust are determined. From independently obtained data on soil minerals and their grain densities, the porosity of the upper portion of the lunar crust may be mapped.

The main part of this thesis consists of two scientific publications thematically closely related. The first publication focuses on the methods for determining lateral variations in bulk density. An approach presented by Wieczorek et al. (2013) is compared to a modified method. Benefitting from the higher spatial resolution of the new data, an investigation of the crustal structure associated with individual impact basins becomes possible, which is subject of the second publication of this thesis. Here, values of the porosity of the upper lunar crust are derived. By filtering the spherical harmonic coefficients below degree and order 150, the long wavelength gravity contribution, possibly originating from lithospheric flexure in deeper regions, is removed. This allows us to examine large impact structures with diameters exceeding 200 km, which usually show a bending of the crust-mantle interface due to a mantle uplift, and which therefore had to be omitted in previous studies (Millbury et al., 2015).

We would like to emphasize that both methods for determining the lateral variations in bulk density of the upper crust presented in this work, assume a constant density in the vertical, not necessarily an adequate model. Several observations indicate that density increases with depth: (1) the moment of inertia of the Moon (Section 2.2.4), seismic velocities from the Apollo seismic experiment (e.g., Cooper et al., 1974, Nakamura, 1983; Khan et al., 2000), the analysis of single spectral bands of GRAIL gravity field data (Besserer et al., 2015) as well as first model tests on mapping lateral variations for certain depth of the lunar crust, presented in the outlook (Section 5.3). Therefore, the results of lateral variations in bulk density and porosity in this work must be considered as an average value of the upper few kilometers of the lunar crust.

5.1 Similarities between bulk density and porosity

Lateral variations in bulk density and porosity of the highland crust show a similar global distribution, as indicated comparing Figure 26 with Figure 27. The estimated correlation coefficient of -0.9590 confirms the high dependency. Since the porosity of a rock describes its bulk density in relation to its pore-free grain density, both datasets would show larger deviations, if grain densities of the highland crust would show more variability (Figure 36). Global grain densities of the upper crust are derived based on remotely acquired iron and titanium abundancies (Huang and Wieczorek, 2012). In the Procellarum KREEP terrain (PKT) region, in the South Pole-Aitken basin, and within specific impact basins, where mare basalts are exposed, high variations in concentrations of TiO_2 and FeO are found (Prettyman et al., 2006), indicating a wide range of grain densities of up to 3500 kg m^{-3}. While mare basalts show a variety of compositional styles, the highlands reveal depleted, quite similar concentrations of titanium and iron. Consequently, the diversity in bulk density of the highland crust may not be associated with varying compositions (and associated grain densities) of lunar rocks but is primarily related to lateral variations in crustal porosity.

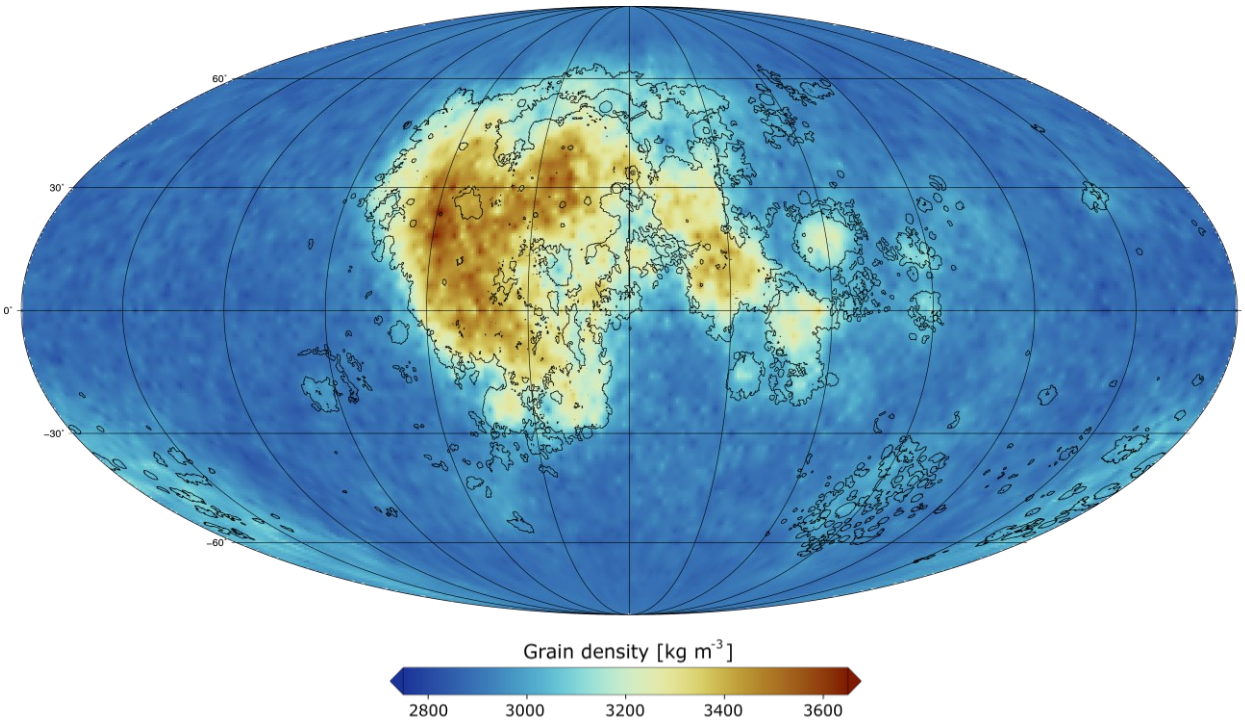

Figure 36: Global grain densities derived from titanium and iron abundancies (Huang and Wieczorek, 2012). The map is presented using a Mollweide equal-area projection, centered at the lunar nearside at 0° East, 0° North. Mare basaltic regions are outlined in black (Nelson et al., 2014).

5.2 Omission of lunar mare regions

All investigations concerning the bulk density and porosity of the crust in this work are limited to the lunar highlands. Mare basaltic regions are excluded from the investigations on account of scientific and technical reasons:

(1) The lunar crust was formed in the course of a cooling magma ocean, where minerals of different composition and density differentiated (see Section 2.2.1). Material of low density floated upwards, forming the anorthositic crust. However, the lunar maria, consisting of dark basaltic rock, was formed subsequently, in the course of volcanic activity. The large impact basins, mainly located at the lunar nearside, were flooded with basaltic magma, which was produced by melting of mantle material about 100 - 400 km below the surface (Shearer et al., 2006). The erupted magma solidified and formed the lunar maria, being much denser than the underlying anorthositic crust. Therefore, mare basaltic regions constitute a special case, not representing the initial crustal material. Consequently, those regions were omitted from the current study, not to mention that those areas have a complex structure. In particular, little is known about the depth of the basaltic deposits.
(2) As shown in the first publication of this dissertation (Section 3), two different methods for estimating the bulk density of the upper crust were tested. For the highland regions, where prominent topographic features are lacking, the results differ, indicating that in flat areas one or both methods fail to obtain reasonable values. As the lunar maria has an exceptionally flat appearance with less topographic features as well as a complex interior structure with mare basalts overlaying anorthositic rock, the presented methods could not be applied here.

5.3 Future work

Previous studies regarding the bulk density and porosity of the lunar crust considered either lateral variations (like in the present work) or focused on density depth profiles. But both approaches have limitations: While methods for estimating lateral variations in bulk density and porosity are only applicable for the upper part of the crust, investigations focusing on profiles attempt to find model solutions for analyzing single spectral bands (being sensitive for different depth) but extending over the entire sphere. A localized spectral analysis may be obtained by multiplying the data by a selective window (called taper), before the spectral expansion is performed (Wieczorek and Simons, 2005). An approach of a mixed analysis was presented by Besserer et al. (2015), who applied a localized, multi-taper admittance analysis using GRAIL

gravity data developed to degree and order 900. The derived maps of density gradients show that the farside is characterized by an increase in density with depth, while the mare areas exhibit high surface densities and a distinct decrease with depth. Since the long wavelength portion of the total gravity field signal was removed to avoid biases from contribution of lithospheric flexure, the results are restricted to the shallow density structure of the lunar crust.

In future studies, we recommend carrying out an investigation on subsurface density variations in the spatial domain. By analyzing spherical harmonic coefficients covering ranges of different degree and order separately, and by subjecting them to the methods for estimating the bulk density (see Section 3.3), the bulk density near the surface may be modelled for layers of different depth. In Figure 37 the results of a preliminary test are shown. Using the example of Hertzsprung basin, the spherical harmonic coefficients for the gravity and topography models are subdivided into three parts with spherical harmonic coefficient ranges of degree and order 450 - 700 (B), 300 - 450 (C), and 150 - 300 (D). The surface topography, presented as shaded relief, is shown on top (A). The approach is based on the idea that the short wavelength gravity signal (coefficients of large degree) represents the upper layers of an observed body, while the low degree coefficients include signals of deeper structures (e.g., Watts and Daly, 1981; Besserer et al., 2014).

Preliminary results reveal a trend of increasing bulk density with increasing depth. However, the method has some drawbacks, which need to be investigated in detail in future studies: (1) The spatial resolution reduces for deeper layers due to the reduced maximum spherical harmonic coefficient degree and order. (2) The modelling of the gravitational potential is nonunique. Therefore, it is not possible to link a certain spherical harmonic degree and order to an exact depth. (3) Filtering signals of longer wavelength for each layer may yield biased results, since long-wavelength signals may also be present in shallower regions.

Previous investigations on the formation sequence as well as the determination of absolute model ages of impact basins are often limited to impact structures with diameters larger than 300 km. But several studies suggest that the mass concentration in the basin center dominates the gravity signal for impact craters larger than about 200 km in diameter (e.g., Milbury et al., 2015; Soderblom et al., 2015). Therefore, it is reasonable to define the transition from (lunar) complex crater to impact basin at a diameter of 200 km,

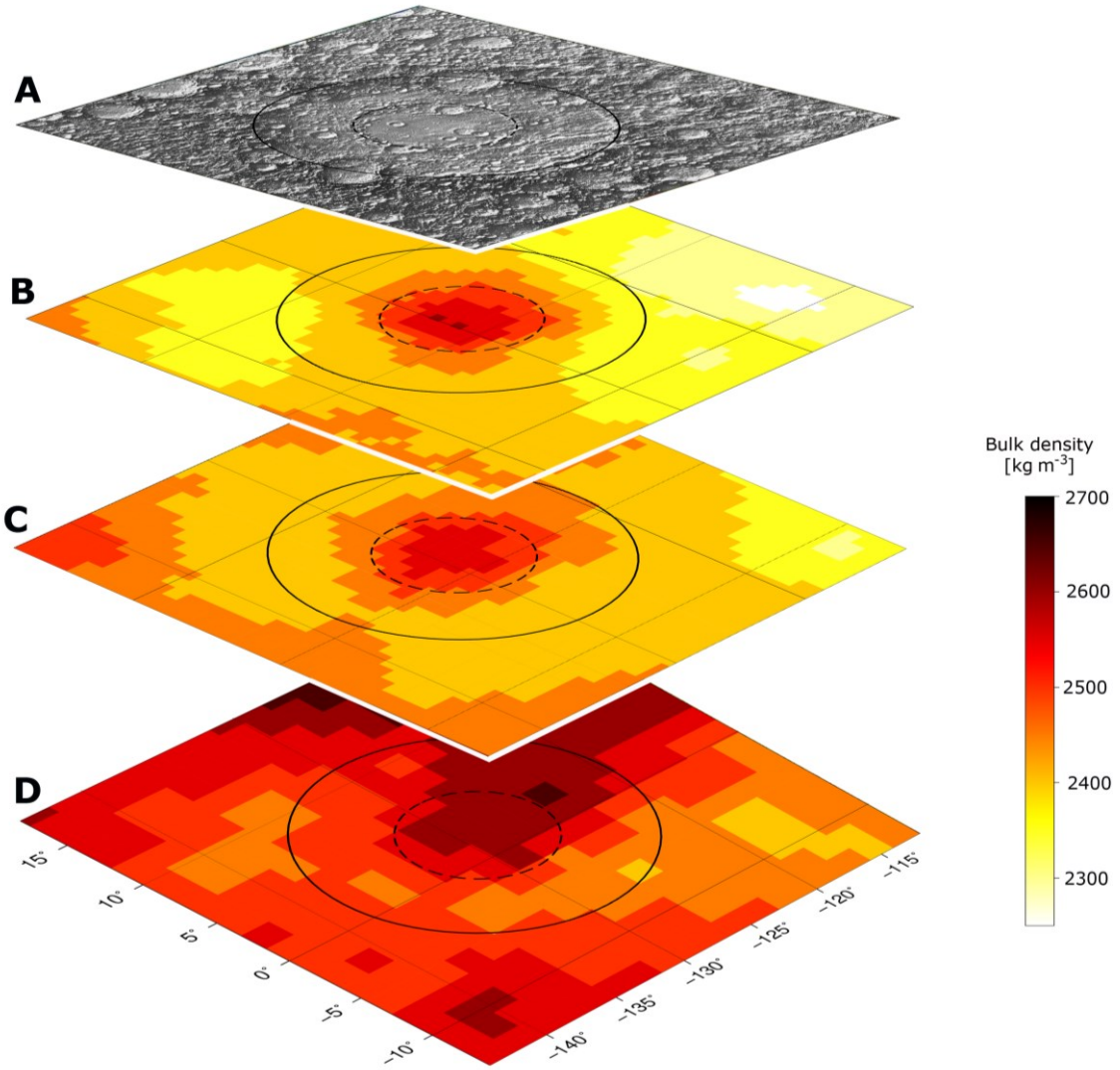

Figure 37: Hertzsprung basin with (A) shaded topography derived from LOLA data. Below, bulk density estimates for a layered model of the upper crust are shown, using coefficients between (B) 550-700, (C) 300-550, and (D) 150-300. The basin main rim is marked with a solid black line, the peak ring is marked with a dashed line (Neumann et al., 2015).

where the physical characteristics change. A larger number of dated impact basins would greatly improve the presented statistics in this work concerning the correlation between basin age and porosity signature (see Section 4.4.2).

In earlier studies, where Bouguer gravity is used for investigating subsurface structures, the Bouguer correction is usually calculated applying a global average bulk density of 2550 kg m^{-3} (e.g., Neumann et al., 2015; Zuber et al., 2016; Baker et al., 2017). Apart from the fact that this value only applies for the highland crust, the usage of local Bouguer gravity solutions would greatly improve understanding subsurface structures, allowing also a reexamination of the method for determining relative ages of impact basins based on their gravity signature, as presented in this work (Section 2.3.3).

References

Baker, D.M.H., Head, J.W. Phillips, R.J., Neumann, G.A., Bierson, C.J., Smith, D.E., Zuber, M.T (2017) GRAIL gravity observations of the transition from complex crater to peak-ring basin on the Moon: Implications for crustal structure and impact basin formation. Icarus, 292, 54-73.

Besserer, J., Nimmo, F., Wieczorek, M.A., Weber, R.C., Kiefer, W.S., McGovern, P.J., Andrews-Hanna, J.C., Smith, D.E. and Zuber, M.T. (2014) GRAIL gravity constraints on the vertical and lateral density structure of the lunar crust. Geophysical Research Letters, 41, 5771-5777.

Cooper, M.R., Kovach, R.L. and Watkins, J.S. (1974) Lunar Near-Surface Structure. Reviews of Geophysics and Space Physics, 12, 291–308.

Huang, Q. and Wieczorek, M.A. (2012) Density and porosity of the lunar crust from gravity and topography. Journal of Geophysical Research: Planets, 117, 1–9.

Khan, A., Mosegaard, K. and Rasmussen, K.L. (2000) A new seismic velocity model for the moon from a Monte Carlo inversion of the Apollo lunar seismic data. Geophysical Research Letters, 27, 1591–1594.

Konopliv, A.S., Binder, A.B., Hood, L.L., Kucinskas, A.B., Sjogren, W.L., Williams, J.G. (1998) Improved gravity field of the moon from lunar prospector. Science, 281, 1476-1480.

Milbury, C., Johnson, B.C., Melosh, H.J., Collins, G.S., Blair, D.M., Soderblom, J.M., Nimmo, F., Bierson, C.J., Phillips, R.J., Zuber, M.T. (2015). Preimpact porosity controls the gravity signature of lunar craters. Geophysical Research Letters, 42(22), 9711–9716.

Nakamura, Y. (1983) Seismic Velocity Structure of the Lunar Mantle. Journal of Geophysical Research, 88, 677–686.

Nelson, D.M., Koeber, S.D., Daud, K., Robinson, M.S., Watters, T., Banks, M. and Williams, N.R., 2014. Mapping Lunar Maria Extents and Lobate Scarps Using LROC Image Products. Lunar and Planetary Science Conference. Abstract #2861.

Neumann, G.A., Zuber, M.T., Wieczorek, M.A., Head, J.W., Baker, D.M.H., Solomon, S.C., Smith, D.E., Lemoine, F.G., Mazarico, E., Sabaka, T.J., Goossens, S.J., Melosh, H.J., Phillips, R.J., Asmar, S.W., Konopliv, A.S., Williams, J.G., Sori, M.M., Soderblom, J.M., Miljković, K., Andrews-Hanna, J.C., Nimmo, F. and Kiefer, W.S. (2015) Lunar impact basins revealed by Gravity Recovery and Interior Laboratory measurements. Science Advances, 1(9), e1500852–e1500852.

Prettyman, T.H., Hagerty, J.J., Elphic, R.C., Feldman, W.C., Lawrence, D.J., McKinney, G.W. and Vaniman, D.T. (2006) Elemental composition of the lunar surface: Analysis of gamma ray spectroscopy data from Lunar Prospector. Journal of Geophysical Research: Planets, 111, 1-41.

Shearer, C.K., Hess, P.C., Wieczorek, M.A., Pritchard, M.E., Parmentier, E.M., Borg, L.E., Longhi, J., Elkins-Tanton, L.T., Neal, C.R., Antonenko, I., Canup, R.M., Halliday, A.N., Grove, T.L., Hager, B.H., Lee, D.C. and Wiechert, U. (2006) Thermal and magmatic evolution of the Moon. Reviews in Mineralogy and Geochemistry, 60, 365-518.

Soderblom, J.M., Evans, A.J., Johnson, B.C., Melosh, H.J., Miljkovi, K., Phillips, R.J., Andrews-Hanna, J.C., Bierson, C.J., Head, J.W., Milbury, C., Neumann, G.A., Nimmo, F., Smith, D.E., Solomon, S.C. and Sori, M.M. (2015) The fractured Moon: Production and saturation of porosity in the lunar highlands from impact cratering, 6939-6944.

Watts, A. and Daly, S.F. (1981) Long wavelength gravity and topography anomalies. Annual review of Earth and Planetary Sciences, 9, 415-448.

Wieczorek, M.A., Jolliff, B.L., Khan, A., Pritchard, M.E., Weiss, B.P., Williams, J.G., Hood, L.L., Righter, K., Neal, C.R., Shearer, C.K., McCallum, I.S., Tompkins, S., Hawke, B.R., Peterson, C., Gillis, J.J., Bussey, B. (2006) The constitution and structure of the Lunar interior. Reviews in Mineralogy and Geochemistry, 60, 221-364.

Wieczorek, M.A., Neumann, G.A., Nimmo, F., Kiefer, W.S., Taylor, J.G., Melosh, H.J., Phillips, R.J., Solomon, S.C., Andrews-Hanna, J.C., Asmar, S.W., Konopliv, A.S., Lemoine, F.G., Smith, D.E., Watkins, M.M., Williams, J.G. and Zuber, M.T. (2013) The Crust of the Moon as Seen by GRAIL. Science, 339, 671–675.

Wieczorek, M.A. and Simons, F.J. (2005) Localized spectral analysis on the sphere. Geophys. J. Int., 162, 655–675.

Zuber, M.T., Smith, D.E., Neumann, G.A., Goossens, S., Andrews-Hanna, J.C., Head, J.W., Kiefer, W.S., Asmar, S.W., Konopliv, A.S., Lemoine, F.G., Matsuyama, I., Melosh, H.J., McGovern, P.J., Nimmo, F., Phillips, R.J., Solomon, S.C., Taylor, G.J., Watkins, M.M., Wieczorek, M.A., Williams, J.G., Jansen, J.C., Johnson, B.C., Keane, J.T., Mazarico, E., Miljković, K., Park, R.S., Soderblom, J.M., Yuan, D.-N. (2016) Gravity field of the Orientale basin from the Gravity Recovery and Interior Laboratory Mission. Science, 354 (6311), 438-441.

6. Appendix

6.1 Geopotential calculations with spherical harmonic functions

As described e.g., by Heiskanen and Moritz (1967), Newton's Law of Gravity (Eq. 3) can be expressed as integrals, when extending the point-mass to a volume of continuous mass density, bounded by a surface. Alternatively to using integrals, the gravitational potential U for some object of given mass distribution may be expressed in the form of Poisson's equation

$$\nabla^2 \cdot U = -4\pi G\rho \tag{16}$$

where G is the universal gravitational constant, ρ the density, and where

$$\nabla^2 \cdot U = \frac{\partial^2 U}{\partial x^2} + \frac{\partial^2 U}{\partial y^2} + \frac{\partial^2 U}{\partial z^2}\,. \tag{17}$$

The potential as well as the first derivatives of the potential are continuous. However, the second derivatives show discontinuities at interfaces, where the density ρ changes. Outside the volume, where the density ρ is zero, Poisson's equation reduces to Laplace's equation

$$\nabla^2 \cdot U = 0\,. \tag{18}$$

There are solutions in different form for this differential equation depending on the shape of the boundary. For a sphere, solutions may be expressed in the form of spherical harmonic functions, orthogonal sets of solutions of the Laplace's equation, represented in spherical coordinates. The gravitational potential U of a volume at any point on or above the surface can be expressed by the sum over degree l and order m (similar to the wave numbers in the Fourier series) of a spherical harmonic expansion, as

$$U(\theta, \lambda, r) = \frac{GM}{R} \sum_{l=0}^{\infty} \sum_{m=0}^{l} \left(\frac{R}{r}\right)^{l+1} C_{lm}\, Y_{lm}\ (\theta, \lambda) \tag{19}$$

where C_{lm} represent the spherical harmonic coefficients, split into cosine (c_{lm}) and sine (s_{lm}) components of the gravitational potential at a reference radius R which may differ from the radius r, where the potential U is to be evaluated. The spherical harmonic coefficients C_{lm} are the series expansion of the gravity potential in terms of spherical harmonic functions Y_{lm}, derived from gravity field measurements. The spherical harmonics functions Y_{lm} at geographical

colatitude θ and geographical longitude λ are defined as

$$Y_{lm} = P_{lm}\ (\cos\theta) \begin{cases} \cos\ m\lambda \\ \sin\ m\lambda \end{cases} \tag{20}$$

so that the gravitational potential U may be written as

$$U(\theta, \lambda, r) = \frac{GM}{R} \sum_{l=0}^{\infty} \sum_{m=0}^{l} \left(\frac{R}{r}\right)^{l+1} \bar{P}_{lm}(\cos\theta)\ (\bar{c}_{lm} \cos m\lambda + \bar{s}_{lm} \sin m\lambda). \tag{21}$$

When related to a unit sphere, numerical problems may occur. Therefore, the potential is scaled by the factor GM/R, where M is the mass of the planetary body. The unnormalized associated Legendre functions are defined as

$$P_{lm}(\theta) = (-1)^m\ (1-\theta^2)^{\frac{m}{2}}\ \frac{d^m}{d\theta^m}\ P_l(\theta) \tag{22}$$

with the Legendre polynomial

$$P_l(\theta) = \frac{1}{2^l\ l!}\ \frac{d^l}{d\theta^l}\ (\theta^2 - 1)^l \tag{23}$$

The spherical harmonic coefficients used in this work are 4π-normalized (as documented in the associated metadata file accessible on the Planetary Data System), wherefore the coefficients $\bar{c}_{lm}$ and $\bar{s}_{lm}$ (Eq. 21) are marked with a dash, same as the fully normalized associated Legendre functions

$$\bar{P}_{lm} = N_{lm} \cdot P_{lm} \tag{24}$$

with the normalization factor

$$N_{lm} = \sqrt{(2 - \delta_{m0})(2l+1)\frac{(l-m)!}{(l+m)!}} \tag{25}$$

where

$$\delta_{m0} = \begin{cases} 1, & m = 0\,, \\ 0, & m \neq 0\,. \end{cases} \tag{26}$$

For locations close to the poles, spherical harmonic expansions of very high degree and order make the associated Legendre functions become very large, causing classical techniques, as described e.g., by Heiskanen and Moritz (1967) for computing associated Legendre functions and their derivatives, to fail. In Figure 38 the logarithmic values of the Legendre polynomials are

shown as a function of their latitudinal position. Holmes and Featherstone (2002) presented recursive algorithms for solving the fully normalized associated Legendre functions of high degree and order, i.e., 2700. The *standard forward column* method calculates non-sectoral ($l > m$) fully normalized associated Legendre functions from previously computed terms as

$$\bar{P}_{lm}(\theta) = a_{lm} \cos\theta \, \bar{P}_{l-1,m}(\theta) - b_{lm} \, \bar{P}_{l-2,m}(\theta) \tag{27}$$

with

$$a_{lm} = \sqrt{\frac{(2l-1)(2l+1)}{(l-m)(l+m)}} \tag{28}$$

$$b_{lm} = \sqrt{\frac{(2l+1)(l+m-1)(l-m-1)}{(l-m)(l+m)(2l-3)}} \; . \tag{29}$$

The sectoral terms (l = m) are also calculated recursively,

$$\bar{P}_{mm}(\theta) = \sin(\theta) \sqrt{\frac{2m+1}{2m}} \; \bar{P}_{m-1,m-1}(\theta) \tag{30}$$

using the initial values

$$P_{0,0}(\theta) = 1 \quad \text{and} \quad \bar{P}_{1,1}(\theta) = \sqrt{3 \cdot \sin\theta} \; . \tag{31}$$

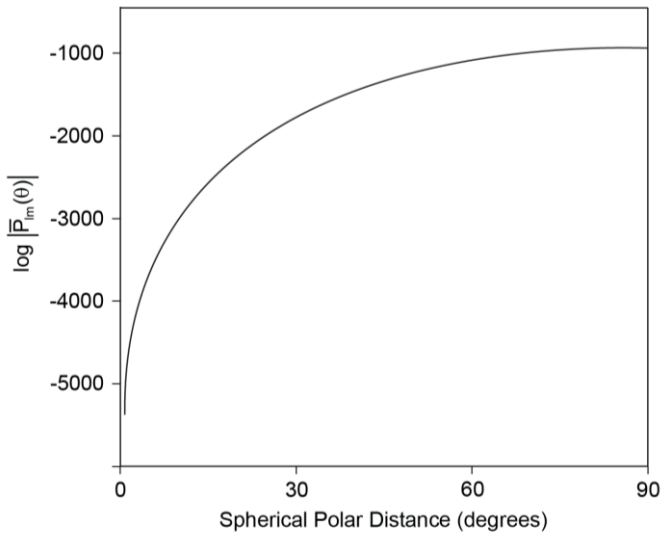

Figure 38: Logarithmic values of the absolute Legendre Polynomials as a function of their latitudinal position on a sphere, for Legendre functions developed up to degree and order 2700 (Holmes and Featherstone, 2002).

6.1.1 Free-air correction

When gravity is measured at a small height above the point of interest (predefined reference level), a correction Δg_{FA} can be applied to extrapolate the measurement downward:

$$\Delta g_{FA} = \frac{2h' g_0}{r_0} \tag{32}$$

with h' being the distance between the point of measurement and the reference level with radius r_0, and with g_0 being the measured gravity at the position of, for example, a satellite (Figure 39). Any topographic masses placed in between are neglected, which is why the resulting gravity field is often referred to as free-air gravity. The free-air gravity is given as

$$g_{FA} = g_T + \Delta g_{FA} - g_{Norm}. \tag{33}$$

where the normal gravity g_{Norm} (approximation of the true gravity by means of a sphere for the Moon, or an ellipsoid for Earth) is subtracted from the total gravity signal g_T, so that the result describes the deviations from the normal gravity field (free-air gravity anomalies). If the gravity is measured below the predefined reference level, the sign of h' is negative and the free-air correction may be subtracted from the total gravity signal g_T.

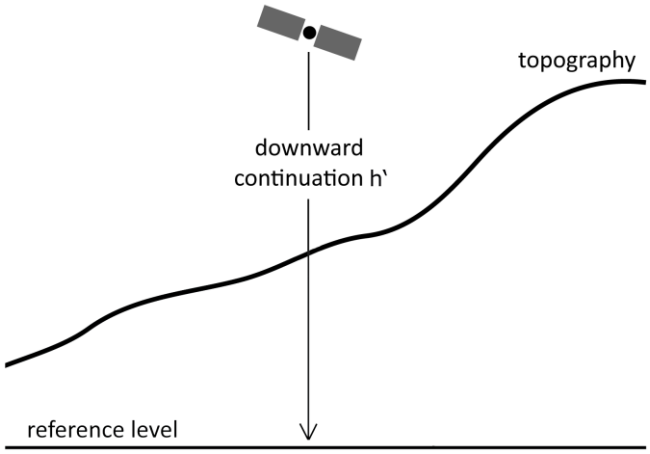

Figure 39: Concept of the free-air correction, downward continuing the measured gravity to a pre-defined reference level, neglecting any masses in between.

6.1.2 Bouguer gravity

The short-wavelength portion of the GRAIL gravity field is highly correlated with the local topography (Zuber et al., 2013b), aggravating efforts of gaining insights into subsurface mass distributions. As a first-order correction, the gravitational attraction of the terrain may be subtracted from the total gravity signal using the Bouguer plate correction, where gravity is compensated for an infinite slab of constant thickness h and constant density ρ as

$$\Delta g_{Bou} = 2\pi G\rho h\,. \tag{34}$$

Consequently, the Bouguer anomalies g_{Bou} are the difference between the gravity signal, corrected for the elevation of the satellites with respect to a reference level, and subtracted normal gravity (Section 6.1.1), and the Bouguer plate correction Δg_{Bou}, given as

$$g_{Bou} = g_{FA} - \Delta g_{Bou}\,. \tag{35}$$

A sketch illustrating the Bouguer plate correction is shown in Figure 40. In case of a rough topography surrounding the point where the measurements are made, the Bouguer plate correction must be considered as a rough estimation. Masses, which are located above the Bouguer plate (area A) are not accounted for and, on the other hand, the topographic masses below the top edge of the Bouguer plate (area B) are overcompensated. If steep topography is present near the point where the measurements are made, these errors become significant. Given the rough lunar topography, deviations of up to 80 mGal may occur (Wieczorek, 2009). To account for steep gradients, an additional terrain correction may be applied.

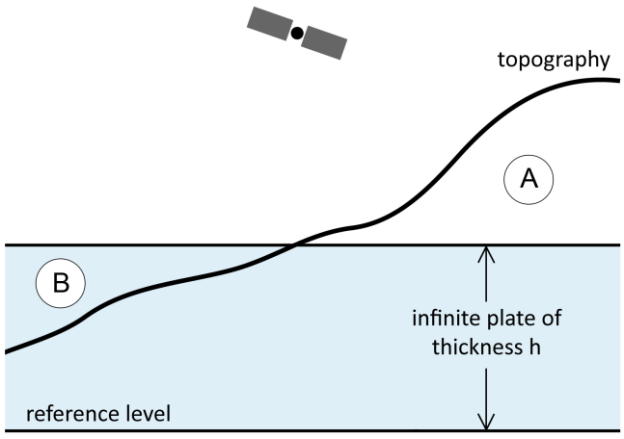

Figure 40: Concepts of the Bouguer plate correction, compensating for an infinite plate of constant thickness h and density ρ.

An alternative, more precise approach for estimating the Bouguer correction is the finite-amplitude scheme of Wieczorek and Phillips (1998), where the attraction of the topographic relief is calculated in the spectral domain. Powers of topography are expanded into spherical harmonics, using a Taylor's series. The potential coefficients C_{lm} with regards to a reference radius D, may be expressed as

$$C_{lm} = \frac{4\pi D^3}{M(2l+1)} \sum_{n=1}^{l+3} \frac{(\rho h^n)_{lm}}{D^n n!} \frac{\prod_{j=1}^{n}(l+4-j)}{(l+3)}. \tag{36}$$

The spherical harmonic coefficients of the density ρ multiplied by the relief h of the nth power can be obtained by calculating the integral

$$(\rho h^n)_{lm} = \frac{1}{4\pi} \int_{\theta,\lambda} [\rho(\theta,\lambda)\ h^n(\theta,\lambda)]\ Y_{lm}(\theta,\lambda)\ d(\Omega) \tag{37}$$

where

$$d(\Omega) = \sin\theta\ d\theta\ d\lambda\ . \tag{38}$$

Since the relation between topography and the potential of the topography is nonlinear (Wieczorek et al., 2007), the potential of the topography may be expanded into series of powers n of the topographic heights. With increasing power n each term of the sum becomes smaller than the previous. The sum can be truncated beyond a maximum value of n, depending on the roughness of the topography. Using only the first order term of Eq. 36 the formula reduces to

$$C_{lm} = \frac{4\pi D^2 (\rho h)_{lm}}{M(2l+1)} \tag{39}$$

and with increasing degree l the results are equivalent to the Bouguer plate approximation (Wieczorek et al., 2007).

6.2 Computation procedure of bulk density and porosity

The bulk density and porosity were calculated using gravity field data in combination with topography, both given in spherical harmonic coefficients. Minimizing the correlation between Bouguer anomalies (applying only the short wavelength portion of the gravity field) and the surface relief, the bulk density was estimated in small analysis regions of 3° radius. Applying grain densities derived from independently obtained data on soil minerals and relating them to the calculated bulk densities, the porosity of the upper lunar crust was determined.

All computations were carried out on a Linux Red Hat Enterprise operating system, release 6.10, using the programming language Python, version 3.0. Maps and figures were created using the software Generic Mapping Tools (GMT; Wessels et al., 2013) version 5.1.1. Spherical harmonic analyses were carried out using the freely available shtools library for Python (Wieczorek and Meschede, 2018). Due to the implementation of fast Fourier transforms when integrating over latitude bands, the synthesis from the continuous spectral to the discrete spatial domain turned out to be faster than classical routines.

However, due to the high resolution of the derived bulk density and porosity maps (240 x 480 points) and the required execution of individually performed spherical harmonic transformations for each grid point (for each grid point an individual reference level had to be taken, based on the average topographic elevation within the analysis region) calculations still turned out to be time intensive (about 300 seconds for each grid point) on a Quadcore Intel Xeon® CPU @ 3.50 GHz.

A schematic sketch of the procedure for calculating global bulk densities and related porosities is given in Figure 41. The GRAIL gravity field model GL1500E together with global topography derived from LOLA data, both expressed in spherical harmonic functions, serve as input data.

For estimating the bulk density of a pre-defined raster of 0.75° spacing, a circular analysis region of 3° radius is moved along the global grid, implemented by looping over 240 points in latitude and 480 points in longitude direction.

First it is selected which points of the global gravity and topography data (having a higher spatial resolution than the resulting grids) are within in the analysis region. This step turned out to be time intensive, as the datasets (having a resolution of ~0.06°) comprise about 18,000,000 points in total. The grids were therefore split in several tiles, to reduce the number of points in the search algorithm and improve the performance of the program.

In a next step, the Bouguer correction (see Section 6.1.2) is calculated. Both, the Bouguer correction as well as the total gravity field were truncated to degree and order of 150 to 700 by setting the remaining coefficients to zero. Since the GRAIL gravity field refers to a radius of

1738 km and the Bouguer gravity to the mean elevation of the topography of 1737.151 km, in the later course (within the program loop) both fields are downward continued (see Section 6.1.1) to the mean topographic radius within the analysis region and scaled to densities, which should be tested (between 2000 and 3100 kg m^{-3}).

It should be noted that since only the short wavelength portion of the total gravity field signal is used, the resulting Bouguer anomalies are not comparable with the classical Bouguer anomalies, where the complete spectrum of the gravity field is used.

In the following, the Pearson correlation between the Bouguer anomalies and the corresponding topography is computed. Since each introduced grid point within the analysis circle has a different area (due to the narrowing grid for points closer to the poles), they were weighted based on their latitudinal position. In parallel, the roughness of the Bouguer anomalies is determined by calculating the standard deviation. In a loop, this procedure is applied to the complete range of bulk densities which should be tested, with a step size of 25 kg m^{-3}. After finishing this routine, the correlation coefficient closest to zero is searched for, referring to the correct bulk density for the processed grid point (correlation approach, see Section 3.3.1). The search for the smallest standard deviation of the Bouguer anomaly surface leads to an alternative bulk density (Bouguer anomaly roughness approach, see Section 3.3.2).

Applying grain densities estimated from the surface composition and putting them into relation to the determined bulk densities (see Section 3.4.3), two sets of crustal porosities are calculated, one based on bulk density determined by the correlation analysis, the other on bulk density from Bouguer anomaly roughness.

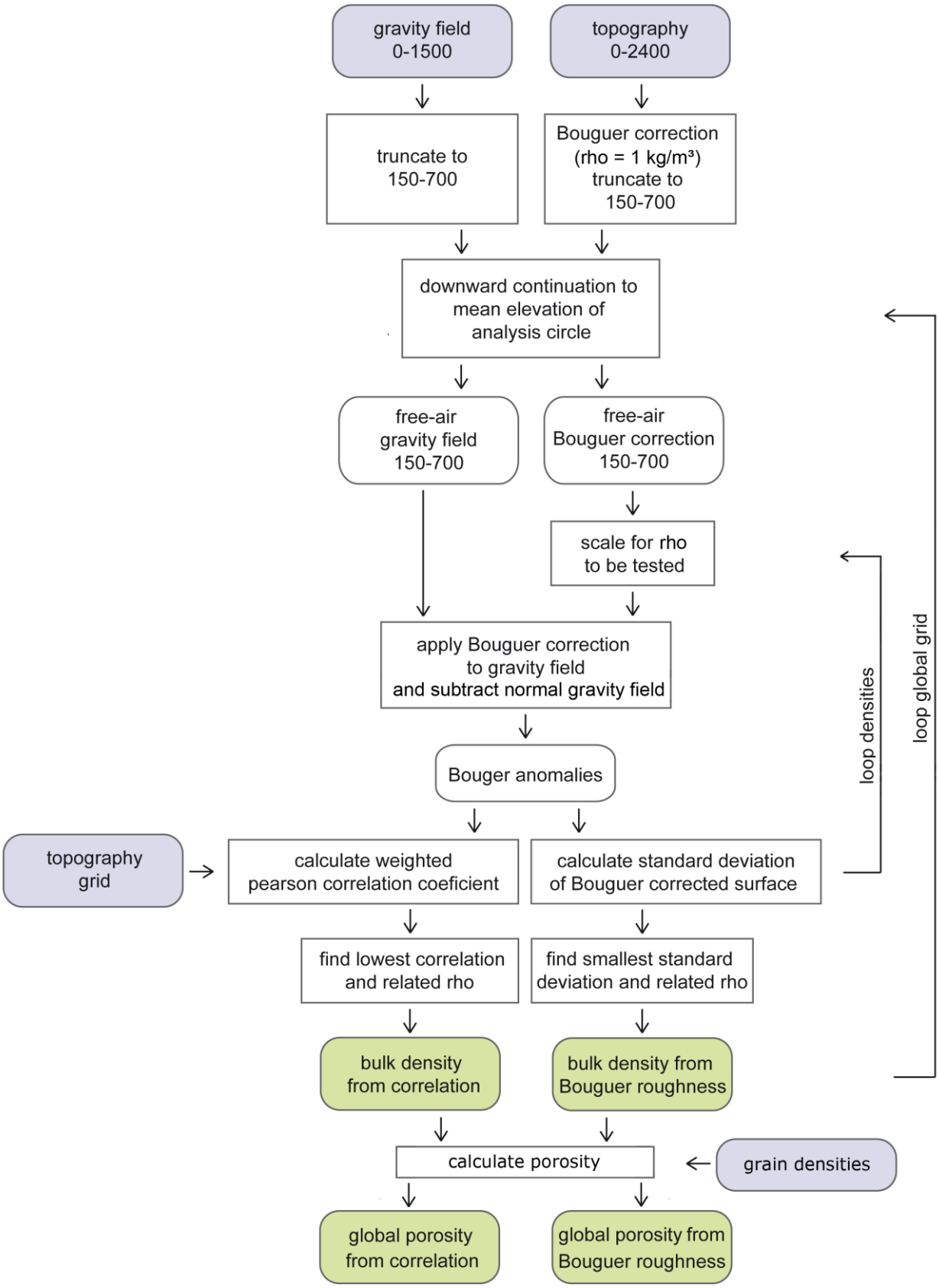

Figure 41: Scheme of the program sequence for calculating bulk density and porosity of the upper crust. Input data are marked in blue, green fields symbolize the results.

6.3 Finding the appropriate spatial resolutions of maps

Each grid point (with a spacing of 0.75°) of the bulk density map shown in Figure 26 was calculated using a circular analysis region of 3° radius, which corresponds to a diameter of about 180 km. The resolution was chosen based on several factors. First, we considered the estimated uncertainties of bulk densities when testing for different analysis region sizes. As it can be seen in Table 3, the uncertainties increase with a decrease in size of the analysis region, while the global mean density for different circle dimensions is almost constant. Since the uncertainties are influenced by the geological properties at individual locations (see Section 3.3), they do not represent a meaningful parameter for finding the appropriate resolution.

Table 3: Mean bulk densities and related uncertainties of the highland crust using different analysis circle dimensions.

Analysis region radius [deg]	correlation approach		Bouguer anomaly roughness	
	mean density [kg m^{-3}]	standard deviation [kg m^{-3}]	mean density [kg m^{-3}]	standard deviation [kg m^{-3}]
1.5°	2532.4	48.8	2496.1	44.7
2.25°	2529.6	34.3	2506.4	32.3
3.0°	2536.1	21.4	2503.0	23.6
4.5°	2536.8	6.8	2505.2	7.1
6.0°	2537.0	5.0	2506.0	5.3

In a next step, we computed global bulk density using analysis regions of various sizes and compared the resulting maps. Wieczorek et al. (2013) (using a gravity spherical harmonic model, truncated at degree and order 310) applied an analysis region of 6° radius (corresponding to a diameter of about 360 km). Since we use a gravity field model at about twice the resolution, we initially used analysis regions half this size. An important indicator for finding the proper resolution for the applied datasets were (independently derived) grain densities of the highland crust provided by Huang and Wieczorek (2012). Based on remote sensing data of surface composition, they found grain densities of up to 2860 kg m^{-3} in the lunar highlands and about 3000 kg m^{-3} in the South Pole-Aitken (SPA) basin (Figure 36). Since the bulk density of a rock cannot be higher than the pore free density, the grain densities serve as an upper limit, which should not be exceeded when testing for the right resolution.

In Figure 42 maps of lateral variations in bulk density are shown, together with the related histograms for different tested sizes of analysis regions, calculated with the correlation approach. For smaller analysis regions, bulk densities show a broader distribution, and the maps appear to show a higher variability. For the circle radii of 1.5° and 2.25° some data approach or become larger than values of 3000 kg m^{-3}, which are physically not possible, suggesting that the analysis region was chosen too small. On the other hand, maps where analysis regions of 4.5° and 6° radius were used show a narrower range in bulk densities around the global mean, but are heavily smeared, suggesting that analysis regions are chosen too conservative. Using an analysis region of 3° radius for our calculations seems to be the appropriate compromise in resolution. For the sake of completeness, in Figure 43 the results for different analysis circle dimensions, using the Bouguer anomaly roughness approach are given. The maps are very similar to those obtained with the correlation approach, as exemplified in Section 3.5.

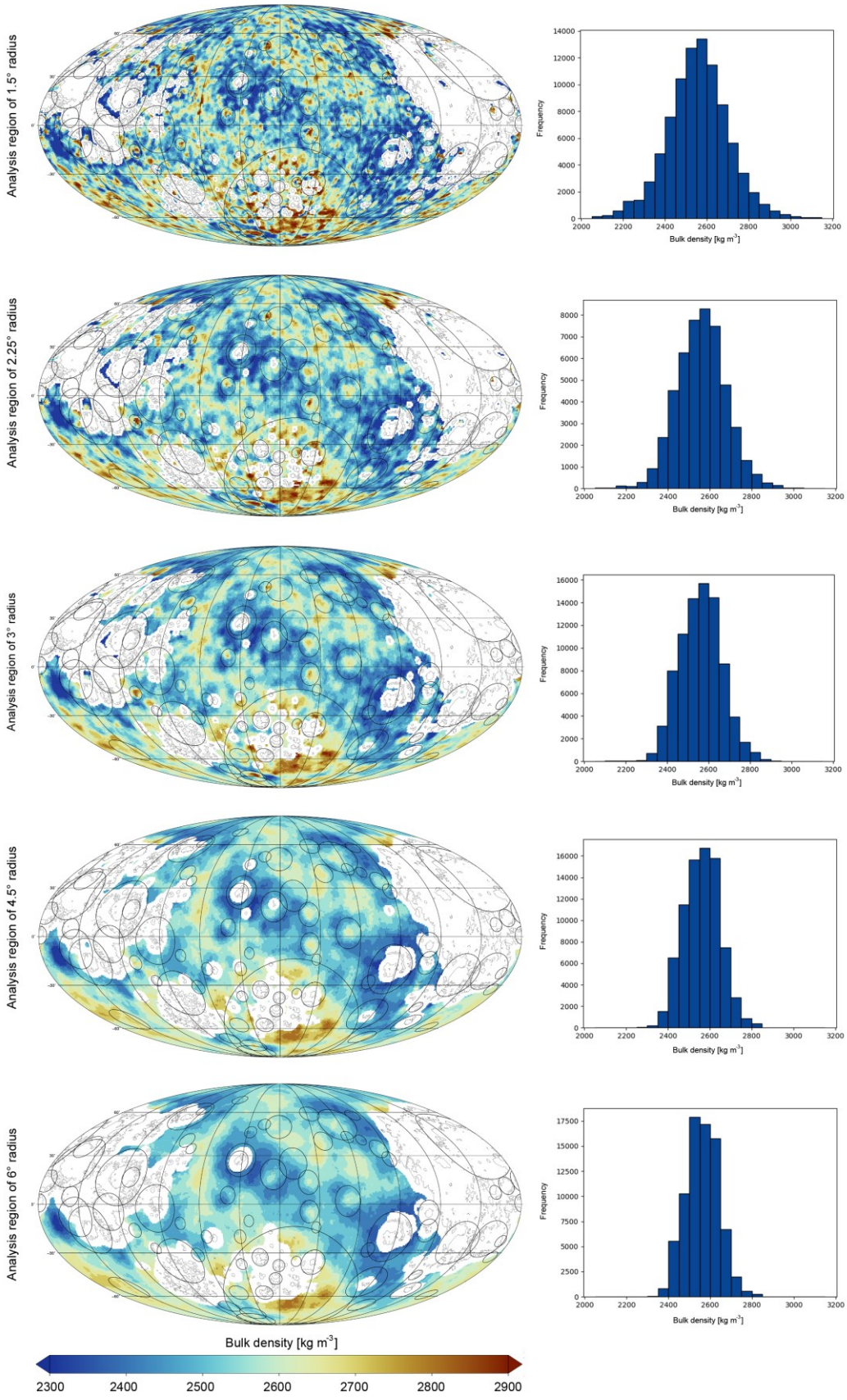

Figure 42: Bulk density estimates (correlation approach) using analysis regions of 1.5°, 2.25°, 3°, 4,5°, and 6° radius (from top to bottom). Projection and labels of the maps are identical to those in Figure 26. The cumulative frequencies of individual bulk densities are given on the right.

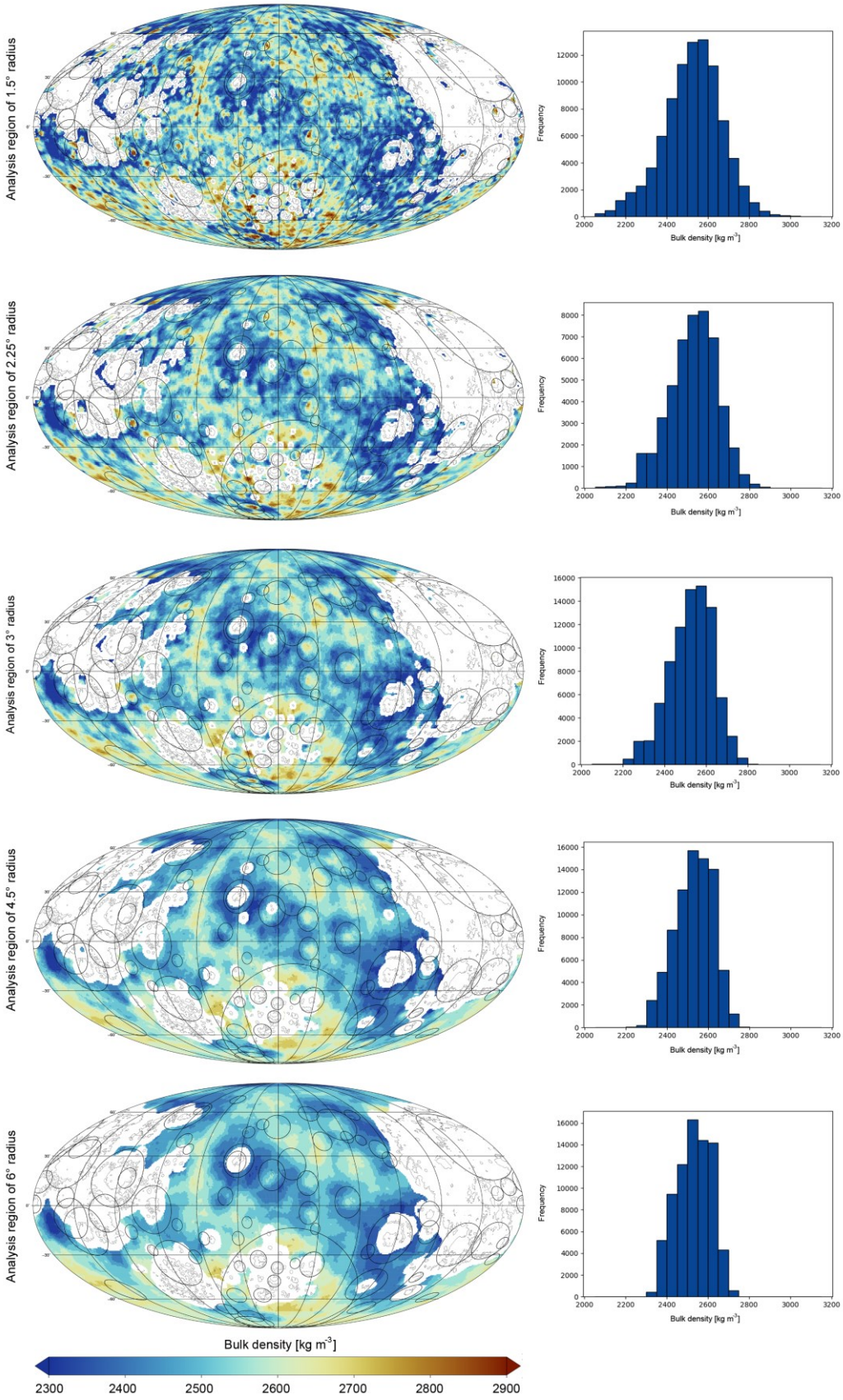

Figure 43: Bulk density estimates (from Bouguer gravity roughness) using analysis regions of 1.5°, 2.25°, 3°, 4,5°, and 6° radius (from top to bottom). Format is the same as in Figure 42.

References

Driscoll, J.R. and Healy, D.M., 1994. Computing fourier transforms and convolutions on the 2-sphere, 202-250.

Heiskanen, W. and Moritz, H. (1967) Physical Geodesy, Freeman, San Francisco, pp. 364.

Holmes, S. and Featherstone, W. (2002) A unified approach to the Clenshaw summation and the recursive computation of very high degree and order normalised associated Legendre functions. Journal of Geodesy, 76 (5), 279-299.

Huang, Q. and Wieczorek, M.A. (2012) Density and porosity of the lunar crust from gravity and topography. Journal of Geophysical Research: Planets, 117, 1-9.

Ramilien, G. (2002) Gravity / magnetic potential of uneven shell topography, Journal of Geodesy, 76, 139-149.

Wessel, P., Smith, W.H.F., Scharroo, R., Luis, J. and Wobbe, F. (2013). Generic mapping tools: Improved version released. EOS, Transactions American Geophysical Union,94(45), 409–410.

Wieczorek, M.A., 2009. Gravity and topography of the terrestrial planets. In: G. Schubert and T. Spohn (eds), Treatise on Geophysics, Vol. 10, Elsevier, Amsterdam, 165–206.

Wieczorek, M.A. and Meschede, M., 2018. SHTools: Tools for Working with Spherical Harmonics. Geochemistry, Geophysics, Geosystems 19(8), 2574-2592.

Wieczorek, M.A., Neumann, G.A., Nimmo, F., Kiefer, W.S., Taylor, J.G., Melosh, H.J., Phillips, R.J., Solomon, S.C., Andrews-Hanna, J.C., Asmar, S.W., Konopliv, A.S., Lemoine, F.G., Smith, D.E., Watkins, M.M., Williams, J.G. and Zuber, M.T., 2013. The Crust of the Moon as Seen by GRAIL. Science 339, 671–675.

Wieczorek, M.A. and Phillips, R.J., 1998. Potential anomalies on a sphere: Applications to the thickness of the lunar crust. Journal of Geophysical Research 103(97), 1715–1724.

Zuber, M.T., Smith, D.E., Watkins, M.M., Asmar, S.W., Konopliv, A.S., Lemoine, F.G., et al. (2013) Gravity Field of the Moon from the Gravity Recovery and Interior Laboratory (GRAIL) Mission. Science, 339, 2011–2014.